

Chapter 1. Evaporation and monolayer overview

1.1 Introduction

Effective evaporation reduction by monolayers requires careful dispensing and monitoring conditions so that maximum coverage can be obtained. It will be seen in this chapter that environmental conditions such as wind and microbes can quickly compromise coverage, and render the surface open to evaporation. So an automatic system of informed dispensers using detectors reporting on coverage would best respond to these changes and top up any depletion of coverage.

The aim of this work is to examine as wide a range of detection methods possible and choose the most promising method which lends itself to incorporation into a complete automatic detection and dispensing system, in order to provide more reliance on maximum coverage and lower labour costs. Other groups are focussing on various aspects of monolayer deployment. Various dispensing systems are being investigated by Gavin Brink; brink@usq.edu.au, at USQ, and novel monolayer/polymer materials are being developed by David Solomon and Emma Prime eprime@unimelb.edu.au at the University of Melbourne.

Other methods of evaporation control are reported in this introductory chapter, and also methods for theoretically and experimentally measuring evaporation.

1.2 Water demand and Water storage

Population growth combined with an increase in the standard of living, and associated economic activities have intensified the demand for fresh water all over the world, with the demand in many countries outstripping supply (FAO 2007). One of the most commonly used indicators for relating the water needs to water availability is the Falkenmark Water Stress Indicator (EEMRU 2009). It measures the water resources, in Megalitres (ML) of natural renewable water per capita for a year. A rating of 1.7 is the threshold, above which water shortage occurs only irregularly or locally. Around a value of 1.0 there are limitations to economic development and human health. Below 0.5 the lack of water is a severe constraint to life. Countries with a high renewable water reserves per capita such as Papua New Guinea (166.6), New Zealand (102.8) and Guyana (279.9) are on the high end of the scale, while countries such as Kuwait (0.0), Saudi Arabia (0.1) and Israel (0.1) are on the lower end. On this scale Australia rates at 18.2 (Lawrence, Meigh, & Sullivan 2002). This estimation includes all water sources, such as monsoons in northern Australia where three-quarters of the annual rain falls from September to early January, making it difficult to store and use efficiently. Recent droughts in Australia (Botterill & Chapman 2002) are likely to reduce Australia's Falkenmark index significantly.

Australian Bureau of Statistics figures state that Australia's total use of water for 2004-2005 was 80 Teralitres (TL). Around three-quarters of this water was returned to the environment. The remainder was consumed across the economy. Using these figures, with a current population of close to 22.5

million people (Australian Bureau of Statistics 2010), this would put the Falkenmark index at approximately 4, which shows the difference between water available and water used.

The population in Australia is concentrated in the south, but the river basins with the greatest water-harvesting potential lie in the north. For example, 41% of the run-off rainwater harvested in the Murray-Darling Basin is diverted for human use while the more seasonal Gulf of Carpentaria, with 4 times the run-off has only 0.05% diverted for human use. Diverting just 10% of the flows into the gulf would harness more water than used in the Murray- Darling Basin (Wahlquist 2008). Because of the distinct wet and dry seasons that exist in tropical Australia (Recreation 2010) large scale water storages in the north may be part of the solution by storing water in the December-March wet season; ready for the May-October dry season, thereby providing year round water for cropping.

Over Australia's landmass, the total water storage is estimated to be approximately 94 TL, with 8 TL of this, being stored in over 2 million farm dams (ANCOLD 2008). According to the Australian Bureau of Statistics, the water consumption in 2004-05 was 18.8 TL. The sectors of the economy that used this water in 2007 were (NWC 2008):

- Agriculture: 65%
- Household: 11%
- Water supply industry: 11%
- Other industries (including electricity and gas): 7.4%
- Manufacturing: 3%
- Mining: 2%

Of the water used by the largest consumer, agriculture, most was used for irrigation of crops and pastures. Household water consumption equates to 104 kilolitres (kL) of water per person per year (NWC 2008), though the Australian department of the Environment, Water Heritage and the Arts puts this figure at 156 kL per person for a year (DEWHA 2006). The world health organization WHO defines the minimum daily water requirement as 150 litres per person, or 55 kL per year (Asheesh 2002). Most of the capital cities in Australia, have had water restrictions, with water storage levels generally around the 50% level in 2009 (WSAA 2009). These restrictions include limitations on watering gardens, washing the car and cleaning paving with water from a hose. The effectiveness of these restrictions in Greater Sydney, coupled with the promotion of house water tanks is evident in the fact that water usage per person per year in 2004-05 was 30% lower than 1990-91 (CityofSydney 2009).

Of the 60 TL of Australia's water which is returned to the environment (i.e. not consumed by the sectors above), a proportion of this is used to keep rivers running to provide water downstream of water storages. This leaves the often quoted figure of 40 TL, or half the water used in Australia which is unavoidably lost to the environment from water storages by either seepage or evaporation.

1.3 Seepage

Water is lost from earthen-banked dams via permeation through the underlying soil. This seepage depends on several factors, including permeability of the soil and the pressure exerted on the soil by stored water (Reddi 2003). Permeability can vary over a wide range, depending on soil structure

and composition. Wet areas observed downstream of a water storage, often thought to be natural springs, are generally seepage flows from the storage itself (Byron 2009).

Quantifying seepage losses is an important component of assessing the viability of water storages. The two most common types of seepage flow instruments are the V-notch and the Parshall flume (ASCE 2000). Both techniques involve drilling or digging into the soil near the storage, to directly measure soil water flow rate. An indirect method of measuring seepage is the “Evapcalc” system (Craig 2005; Hancock 2009), which uses water level data from a sensitive pressure transducer (PST), placed on or near the bottom to measure water depth. Obviously water depth is also influenced by evaporation (assuming inflows and outflows are also accurately documented). The Evapcalc system incorporates local evaporation rate estimates based on data obtained from a local weather station. Combining estimates of evaporation from humidity, temperature, and wind speed with the water level gradients taken over time from the PST data allows the seepage rates to be extracted from the water height data.

Methods of limiting seepage from water storages include lining the walls/floor with impermeable plastics such as polyethylene, PVC or polyethylene (HDPE) or butyl rubber. Alternatively sealing may be achieved using fine clays such as Bentonite (Yiasoumi 2004), which are generally incorporated into the topsoil layer of the storage. Compaction of the existing surface soil has also proven useful for some storages (Cripps 2006).

1.4 Evaporation

Evaporation is defined as the change of state of a liquid into a vapour at a temperature below the boiling point of the liquid. Evaporation occurs at the surface of a liquid where water molecules with the highest kinetic energies escape into the gas phase. The resulting decrease in the average kinetic energy of the remaining molecules of the liquid is expressed as a decrease in the temperature of the water (Oxford Reference Online 2009). Two important points given by this definition are that the molecules of highest energy leave the liquid, creating a heat sink at the surface, and that the processes of supplying the heat and removing the water vapour from the surface determine the evaporation rate. So the large amount of vaporization and condensation of water molecules continually occurring at the surface is quite distinct from evaporation which involves complete removal of water molecules away from the surface.

The process of evaporation from the water surface involves several mechanisms and these are summarized in Figure 1.1.

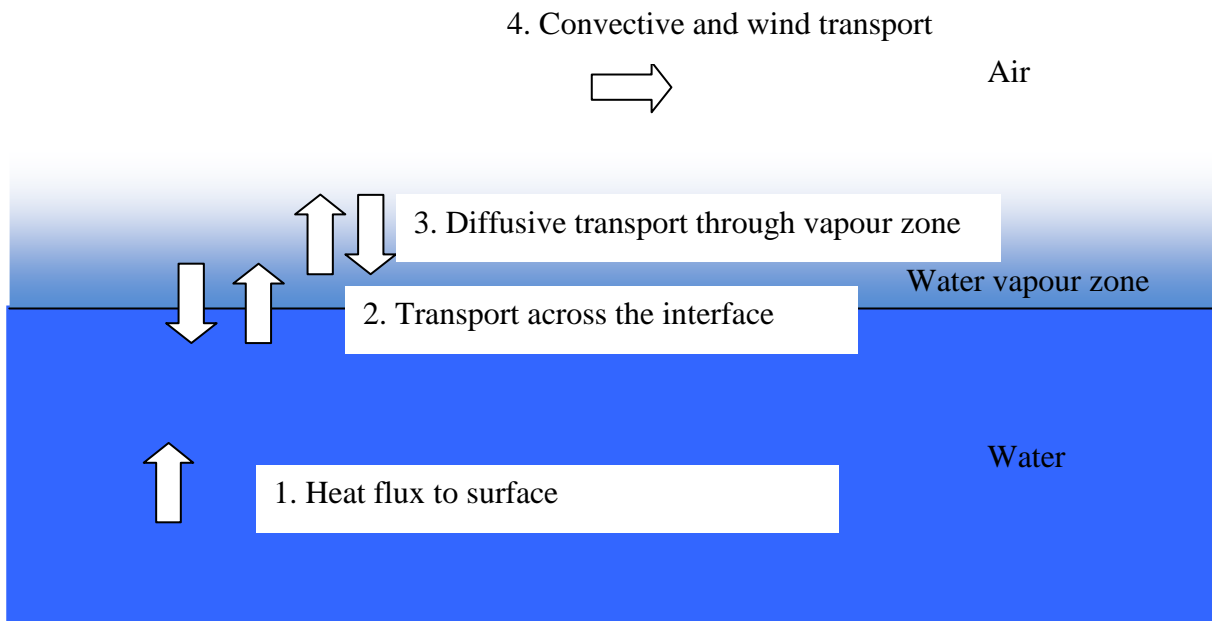


Figure 1.1 Transport across the water surface

The latent heat for evaporation is supplied via an upward-directed heat flux ('1' in Figure 1.1) in the water body, comprising both convective and conductive transport mechanisms. At the surface, this heat is absorbed by vaporization and transportation of the most energetic water molecules, enabling them to cross the interface ('2'). Most of the molecules which leave the surface are immediately returned into liquid phase by collisional condensation, however some undergo diffusive transport ('3'), into the vapour zone. Here the vapour moves by molecular or eddy diffusion, henceforth referred to as diffusion. On traversing the vapour diffusive zone, vapour is moved by convective or wind transport away from the surface ('4') (Wu 1971). The underlying physics of the evaporation process will be discussed in more detail later (Section 1.4.1).

The evaporative demand on a water body is dictated mainly by temperature, humidity of the air, and wind conditions. It is an unfortunate consequence that arid environments, where rainfall is low also typically have the highest evaporative demand, since the humidity of air is also low and daytime temperatures are frequently high. A map of estimated average annual evaporation rates (mm year^{-1}) for Australia is given in Figure 1.2 (BoM 2009). Annual average evaporation rates range from less than $1000 \text{ mm year}^{-1}$ in the more southern and damp coastal areas to more than $4000 \text{ mm year}^{-1}$ in the drier regions of central and Western Australia.

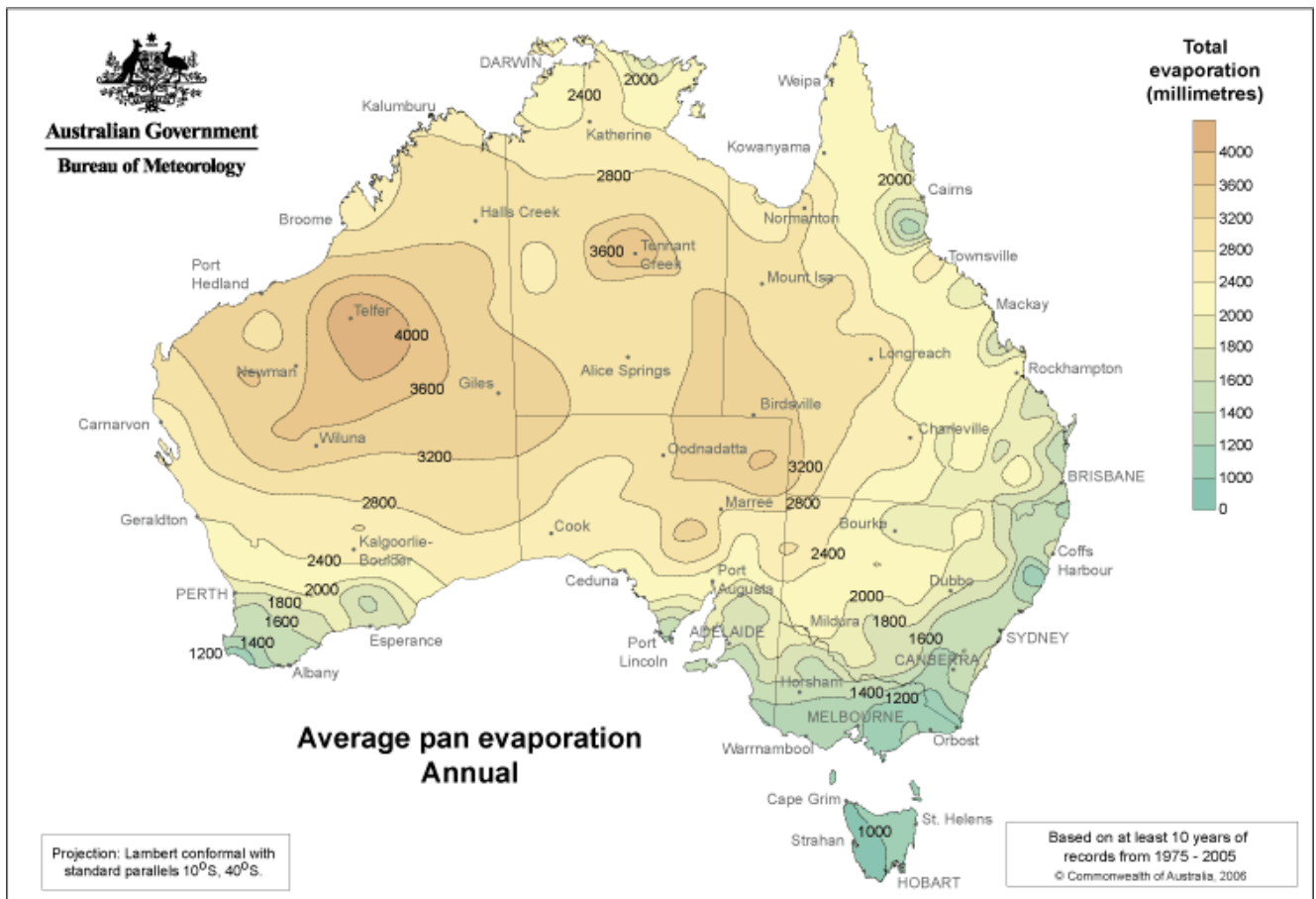


Figure 1.2 Average annual evaporation over Australia using a class A pan. Source; Australian Bureau of Meteorology (BoM 2009)

The annual rate of evaporation over most of Australia is, on average, in excess of 2 m year^{-1} whereas the mean annual rainfall is less than 500 mm year^{-1} (Craig 2008). Figures on capital cities (Table 1.1), which are all on the coastal higher rainfall areas, shows the evaporation is still in excess of the rainfall.

Table 1.1 Average annual rainfall and evaporation rates for Australian cities (BOM 2010)

City	Rainfall m year^{-1}	Evaporation m year^{-1}
Sydney	1.220	1.330
Melbourne	0.661	1.330
Brisbane	1.189	1.425
Perth	0.869	1.710
Adelaide	0.553	1.805
Hobart	0.624	1.045
Darwin	1.666	2.090

Using the estimation of 8 TL being stored in farm dams (ANCOLD 2008), and assuming Australian farm dams are, on average 4-5 m deep (Craig *et al.* 2005) and kept full. The average annual evaporation of 2 m means approximately 3.2 TL, or 40% could be lost to evaporation. In times of rainfall, the amount lost is simply replaced, however in drought, such losses may mean the difference between a farm being able to sustain core breeding livestock or maintain an irrigated crop through to harvest. Clearly reducing the main loss mechanisms, that is seepage and evaporation are very important to the sustainability of a farming enterprise. As discussed previously, the amount of water loss due to evaporation is determined by many factors, including wind stress, temperature and surface area. Reduction of surface area of the water storage is an obvious aim in storage design. In Australia, the cost of increasing the height of an open water storage through earthworks is of the order of \$200-1000 per ML of storage gain (NCEA 2010), although actual costs are highly variable.

Thus, controlling evaporation from open storages, at a cost comparable with earth-works would be an excellent alternative for reducing water loss. In the following sections, the concept of evaporation is discussed in detail along with methods of measuring evaporation rates.

1.4.1 Theoretical basis and estimation of evaporation rates

One of the most commonly used methods for estimating evaporative loss in open water; that is when the water surface is sufficiently large so that edge effects can be ignored, is the Penman Equation (Equation 1.15), originally developed in 1948 at the Rothamsted Experimental Station, UK. It accounts for the energy required to sustain evaporation, and also the mechanism of removing the water vapour from the surface. A derivation of the Penman equation based on Linacre's work (1997) will be described here.

Mass transfer Dalton equation

The relationship between the mass transfer from a water body and the humidity deficit above that body is described by the Dalton Equation (Dalton 1802; Segal & Burstein 2010:131). It estimates the *specific evaporation rate*, m_e , on the basis of wind speed, saturation vapour pressure and air vapour pressure according to:

$$m_e = f(U)(e_{swT} - e) \quad \text{kg s}^{-1} \text{ m}^{-2} \quad (1.1)$$

where $f(U)$ is a function of wind speed U (m s^{-1}), measured at a standard height above the surface. For open water bodies, this height is generally 10 m (U_{10}), which is assumed to be close to the true wind speed (U_∞) as explained in Chapter 5. e_{swT} is the vapour saturation pressure at the water temperature (Pa) and e is the measured air vapour pressure value (Pa). The function $f(U)$ is found empirically from available data for a specific location. Initially Dalton simply used the function kU , where k is a constant (Singh & Xu 1997), however subsequent researchers have found that the correlation with wind is more complicated. To allow for low wind speeds and still air conditions the function is often written in the form $a(1 + bU)$, where a and b are experimentally determined coefficients for a given location (Wu 1971).

The unit of the evaporation rate can be simplified from kg m^{-2} to simply depth evaporated in mm, and since measurements on large storages are made over periods of days, a more practical unit to use is mm day^{-1} . The evaporation E , in mm of height day^{-1} is then:

$$E = a(1 + bU_{1.0})(e_{swT} - e) \quad \text{mm day}^{-1} \quad (1.2)$$

Smith (1909) cites Fitzgerald's results in 1886 on Chestnut Hill reservoir, near Boston, finding the coefficients to be; $a = 1.4 \times 10^{-3}$ and $b = 1.12$ when the pressure is in Pa and the average wind speed is in m s^{-1} measured at a height of 1 m. Penman (1948) similarly determined the constants from data taken over several years, with wind speed measured at a height of 2 m. These were $a = 0.35$ and $b = 1.98 \times 10^{-3}$, in mm day^{-1} . An excellent summary of the forms of this function and subsequent coefficients over history is provided by Singh & Xu (1997).

Measuring humidity

Humidity is often estimated using a "wet and dry" thermometer. These consist of two individual thermometers, one of which has the bulb exposed to air (the 'dry' bulb), and a second 'wet' bulb kept moist, generally by enclosing it in a moist cloth. The relationship between humidity and temperature is given by the relationship:

$$\gamma = -\frac{e - e_{sa}}{T_{dry} - T_{wet}} \quad (1.3)$$

where γ is the **psychrometric constant**, T_{wet} is the temperature of a wet thermometer bulb, T_{dry} is the temperature of a dry thermometer bulb in air, e is the vapour pressure of the air and e_{sa} is the saturated vapour pressure. The psychrometric constant itself can be calculated using:

$$\gamma = \frac{c_a P}{L MW_{ratio}} = \frac{c_a P}{2.45 \times 10^6 \times 0.625} \quad \text{Pa } ^\circ\text{C}^{-1} \quad (1.4)$$

where P is the atmospheric pressure (Pa), L is the latent heat of water vaporization ($2.45 \times 10^6 \text{ J kg}^{-1}$), c_a is the specific heat of air at constant pressure ($\text{J kg}^{-1} \text{ } ^\circ\text{C}^{-1}$) and MW_{ratio} is the ratio of the molecular weights of water vapour (18.0 g) and dry air (28.8 g). The psychrometric constant γ is approximately constant, at the same elevation and similar humidities. As P depends upon altitude, so does γ . Although the specific heat of dry air is constant, the specific heat of real air will increase, the greater the water vapour content.

There are two definitions of relative humidity; (i) the mass of water vapour contained in a sample compared to saturated conditions, and (ii) the partial pressure of water vapour contained compared to the saturated value. In literature it is often difficult to determine which form of relative humidity is being discussed. These would be identical if water vapour was an ideal gas. The difference in the saturated vapour curve for each form of measurement is only a few percent in the temperature region up to 40°C . For the purposes of this thesis the **relative humidity** will always be based on the **partial pressure of water vapour**.

A convenient empirical expression for the temperature-dependent, saturation humidity vapour pressure is based on a polynomial curve fitting of available data between 0 and 40 °C is (Nave 2009):

$$V = 747.51 + 1.0755T + 4.0257T^2 \quad (1.5)$$

where V is the saturated vapour pressure in Pa and T the temperature in Celsius.

The *psychrometric slope*; D , of the saturated vapour pressure-temperature curve relates the saturated vapour pressure of air, at an air temperature T_a to the saturated vapour pressure of the air in the vicinity of a water surface of temperature T_{ws} .

$$D = \frac{(e_{sa} - e_{SWT})}{(T_a - T_{WS})} \quad \text{Pa } ^\circ\text{C}^{-1} \quad (1.6)$$

where e_{wst} is the saturation water vapour pressure at the water surface temperature T_{ws} . The saturated vapour pressure curve for temperatures up to 40 °C is shown in Figure 1.3. The psychrometric slope for a water temperature of 10 °C and an air temperature of 20 °C is drawn in red.

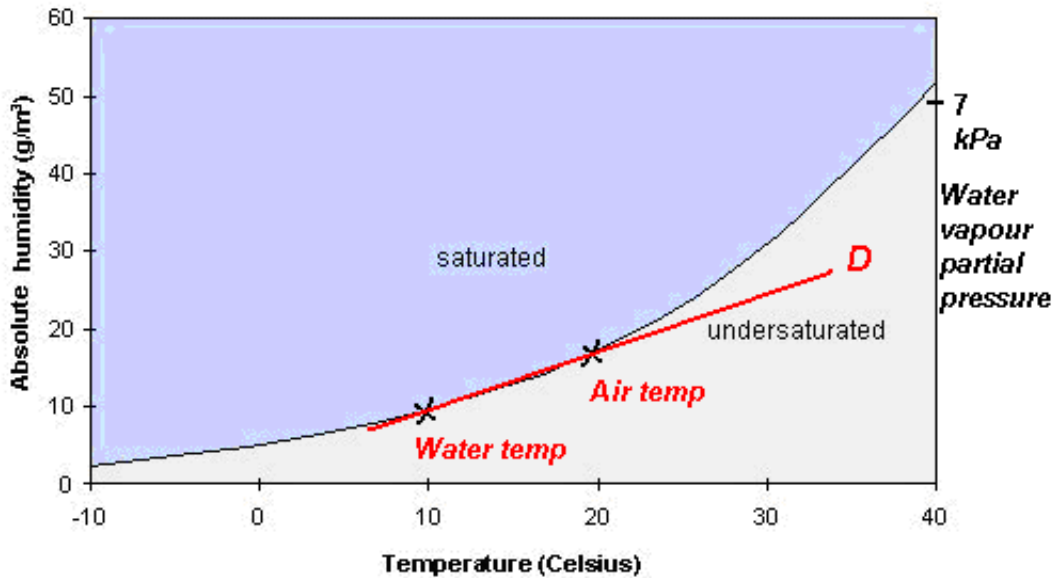


Figure 1.3 Saturated vapour pressure curve, showing the determination of the psychrometric constant D . Adapted from; The Engineering Toolbox (2005).

The evaporation resistance of still air and vapour existing just above the surface of water, a region known as the *vapour diffusion layer*, is the major component in determining the evaporation rate from that water surface (Langmuir & Langmuir 1927; Rideal 1924). The major evaporation process in this layer is diffusion, and the resistance to the vaporization of water molecules is measured by the ‘diffusion resistance’. A relationship between the definition of *diffusion resistance* between water and air is given by (Linacre 1997):

$$r_a = \frac{\rho_a c}{\gamma L f(U)} \quad \text{s m}^{-1} \quad (1.7)$$

where ρ_a is the density of the air (kg m^{-3}), c is its specific heat ($\text{J kg}^{-1} \text{C}^{-1}$), L is the latent heat of evaporation (J kg^{-1}) and γ_s is the psychrometric constant, $f(U)$ is the function of wind speed described earlier in the Dalton equation (Equation 1.1).

The **convective heat flux** H from water to air, can be found using the temperature difference between the water surface T_{WS} and temperature of air T_a combined with the diffusive resistance r_a

$$H = \frac{\rho_a c (T_{WS} - T_a)}{r_a} \quad \text{W m}^{-2} \quad (1.8)$$

This is the usual heat conduction relation with a diffusion resistance factor. The **energy balance** for an insulated water surface (water heat flux $G = 0$) can be found by equating radiant heat with sensible heat flux balance H and latent heat Lm_e :

$$R = Lm_e + H \quad \text{W m}^{-2} \quad (1.9)$$

where R is the **net radiation inflow**.

Combining the Dalton's Equation (1.1) and the diffusion resistance (Equation 1.7) gives:

$$m_e = \frac{\rho_a c (e_{WST} - e)}{\gamma L r_a} \quad \text{kg s}^{-1} \text{m}^{-2} \quad (1.10)$$

The term $(e_{WST} - e)$, can be expanded and substituted into the earlier psychrometric slope definition (Equation 1.6) to give:

$$e_{WST} - e = (e_{WST} - e_{sa}) + (e_{sa} - e) = D(T_{ws} - T) + \delta e \quad \text{Pa} \quad (1.11)$$

where e_{sa} is the saturation vapour pressure of air, and the humidity deficit $\delta e = (e_{sa} - e)$

Substituting Equation 1.10 into Equation 1.9 leads to:

$$m_e = \frac{\rho_a c (D(T_{WS} - T_a) + \delta e)}{\gamma L r_a} \quad (1.12)$$

and rearranging gives:

$$\rho_a .c.D(T_{ws} - T_a) = \gamma.L.m_e.r_a - \rho_a.c\delta e \quad \text{J kg m}^{-4} \text{s}^{-2} \text{C}^{-1} \quad (1.13)$$

which, by equating the first term with the convective heat flux H from water to air (Equation 1.8) gives:

$$H = \frac{\gamma L m_e - \frac{\rho_a c (\delta e)}{r_a}}{D} \quad \text{W m}^{-2} \quad (1.14)$$

By using the energy balance relation (Equation 1.9) to determine the mass of water lost due to evaporation, Penman's equation (1948) is thus obtained:

$$m_e = \frac{DR + \frac{\rho_a c (\delta e)}{r_a}}{L(D + \gamma)} \quad \text{kg s}^{-1} \text{m}^{-2} \quad (1.15)$$

where the first term on the numerator corresponds to sensible heat, and the second to latent heat fluxes. This can be rearranged in terms of the evaporation E_0 .

$$E_0 = \frac{0.408D(R_n - G) + \gamma \left(\frac{900}{T + 273} \right) U_2 (e_{swT} - e)}{D + \gamma(1 + 0.34U_2)} \quad \text{mm day}^{-1} \quad (1.16)$$

where G is the heat flux originating from the water.

1.4.2 Measurement of evaporation

The dissipation of water vapour away from the surface as a measurement of evaporation is difficult to measure directly. It is possible to estimate evaporation rates based on the water vapour concentration at a certain height above the surface, but this requires a detailed consideration of the environmental effects including air temperature, air movement and water temperature. Alternatively, it is possible to infer evaporation rates by measuring the decrease in the water level of a container, or even the water storage itself. Building up an understanding of evaporation dynamics from evaporation rates in the context of large water storages is challenging, not the least because of issues of scale and the need to factor in highly complex environmental conditions.

Controlled, physical, albeit indirect measurements of evaporation conducted either in close proximity to the water storage of interest, or directly in/on the water storage are obviously likely to be more accurate, when it comes to reflecting the influence of external, environmental parameters, such as air temperature, humidity, air flow, insolation etc. A commonly used setup using a synthetic representation of the water storage is a *class A pan*. If the deposits and withdrawals from a water storage is known, then devices measuring water level are useful. Some of these are *stilling wells* using a float to determine depth and *pressure sensing transducer* (PST), determine depth from near the floor of the storage. Radiation measurements can also be used to estimate evaporation in a technique called Bowen ratio, as can accurate wind measurements in Eddy correlation techniques. These will now be discussed in more detail.

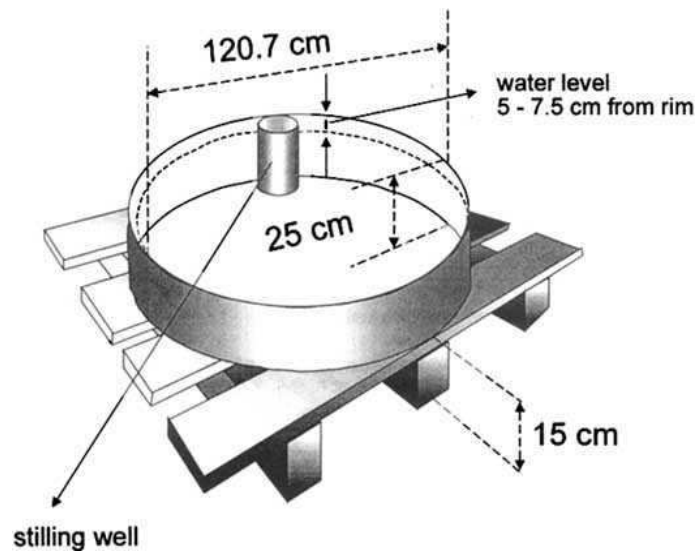


Figure 1.4 Class A pan (SILO 2010).

Class A pan

A small open tank, called a pan, emulating the targeted water storage on a small scale, is placed as close as conveniently possible beside the water storage and its loss of water due to evaporation is monitored. A standard “Class A” pan is commonly used around the world. Its dimensions, as defined by SILO (2010) website are shown in Figure 1.4. Class A pans must be placed on a slatted timber base and equipped with a bird guard and fenced off to prevent animals from drinking. Pans require constant maintenance to keep the contained water clean.

Daily evaporation measurements are performed when the pan is filled to exactly 5 cm from the top. At the end of a 24 hour period the pan is re-filled to exactly the same position and the amount of water required is measured. If there is rainfall in the 24 hour period, a nearby rainfall measurement is necessary in order to extract the evaporation rate from the pan measurements. One obvious problem of this approach is when the daily rainfall exceeds 5 cm as it will cause the pan to overflow. Another problem is encountered when the water surface freezes. Besides these sources of error, a major limitation of using pans to characterize the evaporation of a nearby water storage is the issue of scale and the inability to truly replicate the environmental conditions associated with the considerably larger water storage. For example, the Class A pan evaporation is consistently found to be greater than that from a nearby shallow lake (Eagleman 1967).

Differences occur for several reasons. For example, the pan and its relatively small volume of contained water has less ‘thermal inertia’, that is the temperature of the pan follows air temperature much more closely than the water in the surface layers of a storage (Eagleman 1967). The wind conditions over the contained water are also different to open storages as the pan has 5 cm walls and is often surrounded by protective fencing. There is a typical correction factor K , in:

$$m_e = Km_e^* \quad (1.17)$$

where m_e is the corrected evaporation rate measured from an open water surface and m_e^* is the value gained from the pan.

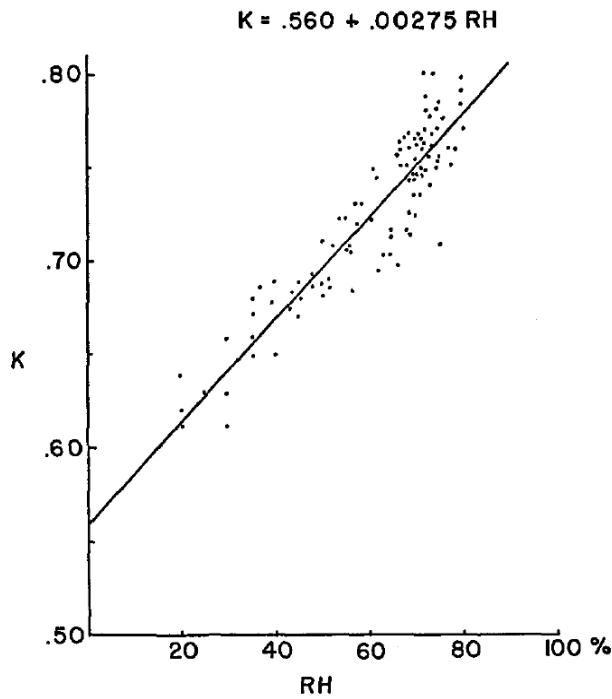


Figure 1.5 Effect of relative humidity on the pan coefficient for average relative humidity (Eagleman 1967).

The *K* correction value is often found to be around 0.7, as shown by averaging the values in Figure 1.5. Indeed the *K*-factor for a pan can be calibrated for the area it represents. The effect of humidity on the *K* value is also displayed in Figure 1.5, showing that the coefficient reduces in arid areas. Local placement of the pan is important as nearby plants increase the local humidity and therefore alter the effective pan coefficient. Interpolated daily pan evaporation estimates for Australia are available for all of Australia from the SILO database (SILO 2010), with the average pan rates over the last 10 years in Australia shown in Figure 1.2.

As filling this type of pan is labour-intensive, they will often have an automatic filling device which can automatically measure the filling volume released. A schematic diagram of an integrated reservoir-based system is shown in Figure 1.6. Data loggers are often attached to the reservoir so that water usage can be plotted as a function of time for ‘on-the-go’ measurements of evaporation rate.

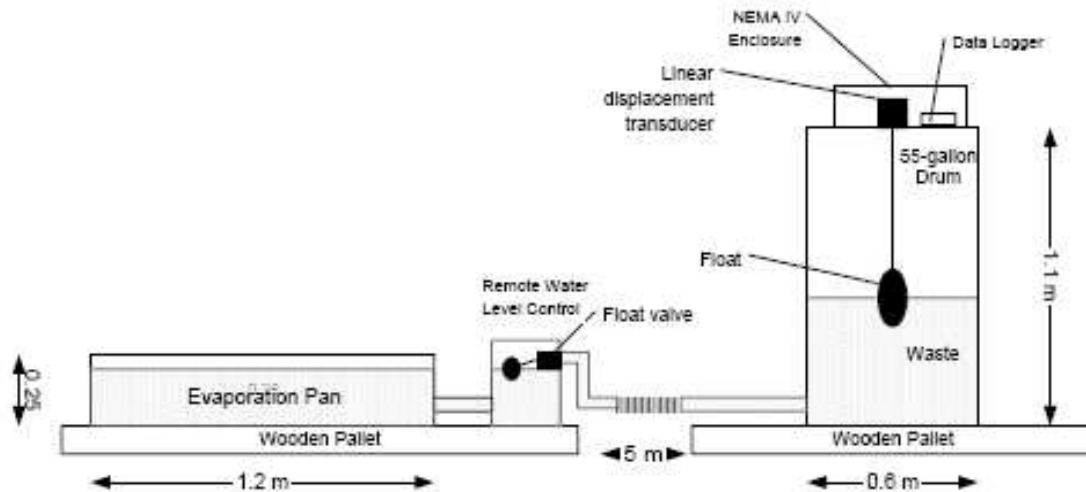


Figure 1.6 A schematic diagram of a Class A pan with and automated reservoir system (Ham (2001)). The height of the wall above the water surface and the nearby structures all may perturb air flow compared to that experienced by a nearby water storage and this needs to be accounted for.

Stilling well

A 'stilling well' is a contained void located either inside the water storage or located beside the storage, in both cases containing water at a level that mimics that within the storage. The vertical 'container' acts as a damping mechanism so that there is only calm water in the well. If located besides a storage a connecting pipe is inserted to allow flow of water in and out so that the water level matches that of the water storage. A hydrological sensor such as a shaft encoder is usually positioned inside the tube so that the water level can be monitored and recorded. Schematic diagrams of the two main forms of stilling well are depicted in Figure 1.7(a) and (b).

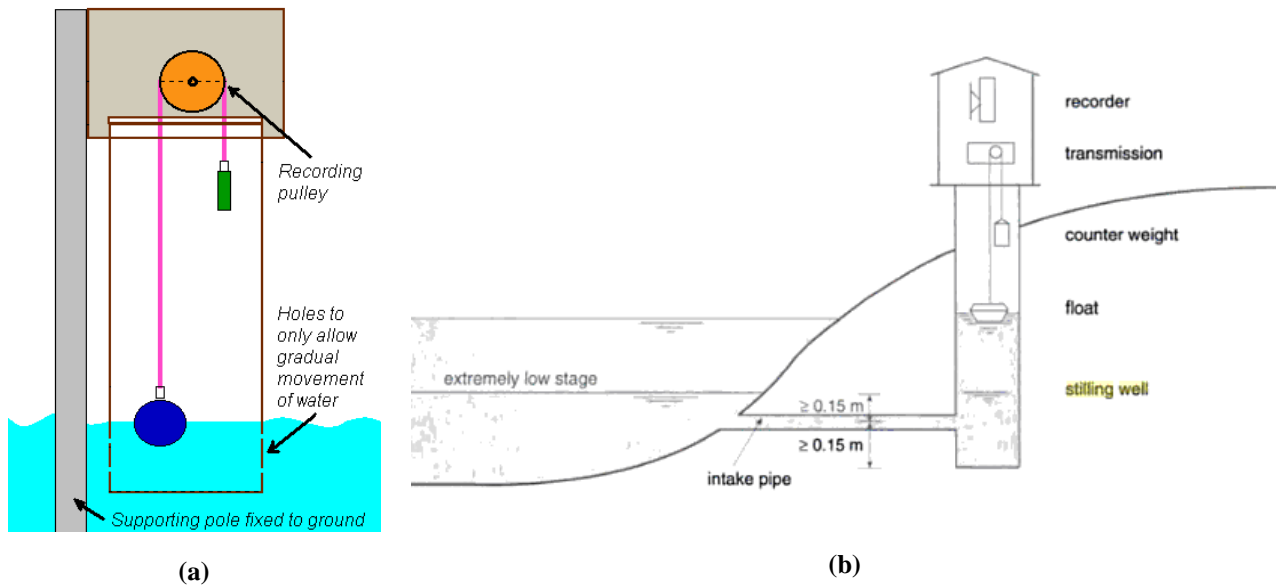


Figure 1.7 (a) Schematic diagram of a simple in-storage stilling well viewing arrangement inside vertical pipe. (b) In-ground type of stilling well (Boiten (2000)).

Pressure sensing transducer

The evaporation rate from a water body can also be evaluated by accurately monitoring the water pressure near the base of the storage. Based on measuring small fluctuations in water depth, the evaporation rate is the difference between the constant seepage of water into the storage walls/floor and oscillating day-night evaporation rates. One approach is to use submersed, temperature-compensated, pressure-sensitive transducers (PSTs) (Craig *et al.* 2005) such as those depicted in Figure 1.8. These devices measure the electrical resistivity of a micro-machined, single silicon crystal, mounted in a high integrity glass-to-metal seal that is isolated from the surrounding water using an alloy ‘HastelloyTM’ diaphragm. With the aid of an atmospheric pressure compensated breather box system, these devices are capable of recording water depth to an accuracy of 1 mm (0.04%) (Craig *et al.* 2005).

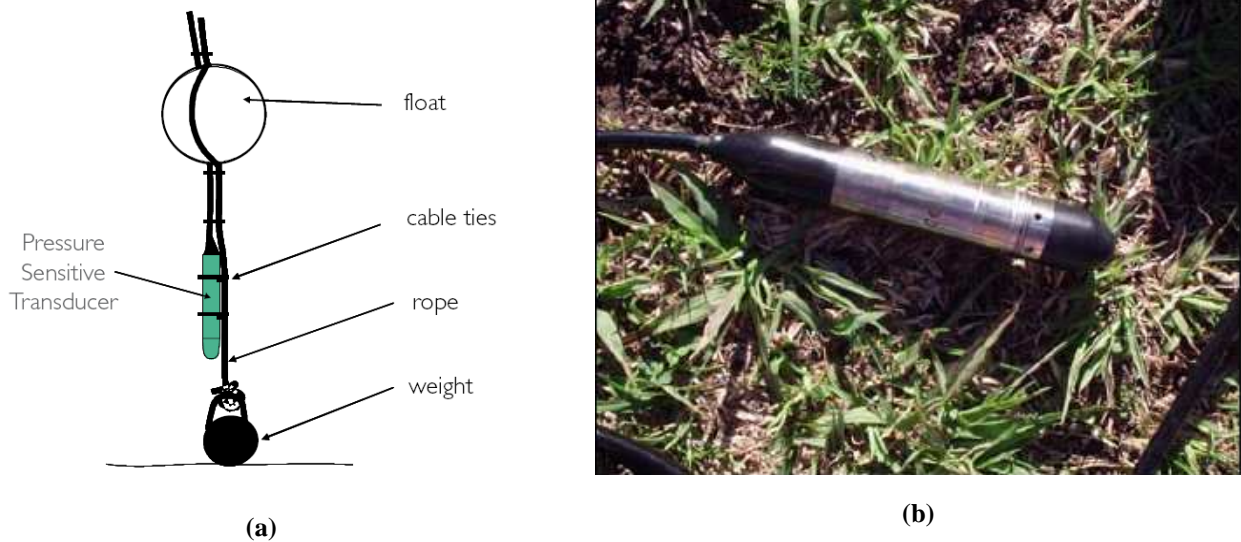


Figure 1.8 (a) Submersing mechanism for pressure sensing transducer (Craig *et al.* 2007) and (b) a close-up photo of a Druck PDCR 4030 Pressure sensing transducer (Craig *et al.* 2005).

Data produced using the PST (Craig *et al.* 2005) is shown in Figure 1.9, along with simultaneous evaporation calculations using variations of the Penman equation with local measurements of conditions. The PST shows some fluctuation, however there is quite good agreement between the two.

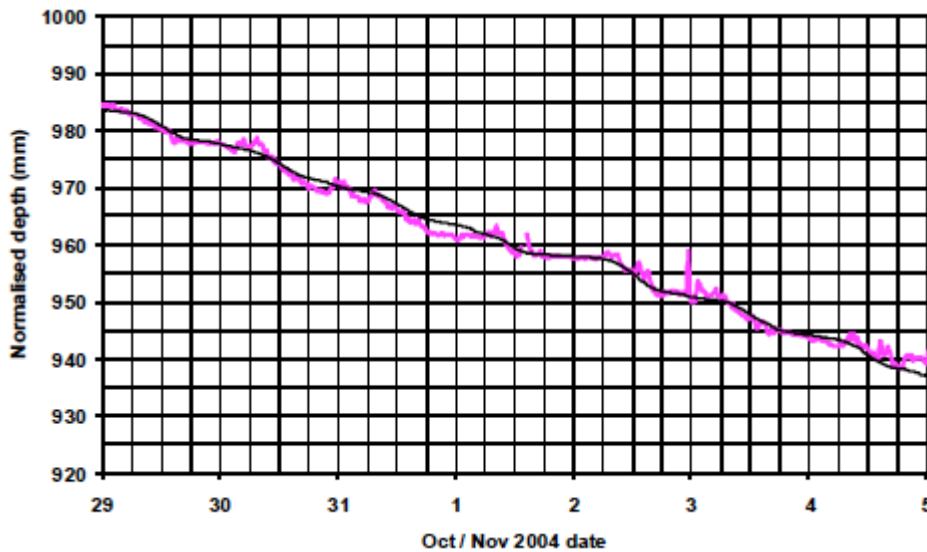


Figure 1.9 Comparison of calculated estimation of evaporation; black line, with PST data; purple line, measured over a week on a 120 ha clay-lined farm dam at Dirranbandi, Qld (Craig *et al.* 2005).

Bowen ratio of heat fluxes

Bowen (1926) recognized that the diffusion of water vapour from the surface is very similar to the diffusion of heat upwards from the surface and a ratio of the two is approximately constant. He derived ratios of these two diffusion rates for both still and windy conditions and incorporated both into a semi-empirical model for estimating evaporation. The basic energy flux balance for water storages is:

$$R = H + L_E + G \quad (1.18)$$

where R is the *net radiant energy*, H is the *sensible energy* concerned with a change in temperature of the water and G is the heat loss due to heat fluxes of conduction and convection from the bulk water and ground surrounding the water storage and L_E is the *latent energy* made up of L ; the latent heat of vaporization and m_e ; the evaporation rate. Bowen used a ratio very similar to that used for wet and dry thermometers to calculate humidity for open water, where no edge effects exist. It is based on a difference of temperature compared to a difference in vapour pressure between the surface and air, now called the **Bowen ratio**, B (Ohmura 1982):

$$B = \frac{L_E}{S} = \frac{c_p}{L} \frac{K_T}{K_e} \frac{\Delta T}{\Delta e} = \gamma \frac{K_T}{K_e} \frac{\Delta T}{\Delta e} \quad (1.19)$$

where c_p is the specific heat of the air, K_T is the thermal conductivity in air: $0.024 \text{ W m}^{-1} \text{ }^\circ\text{C}^{-1}$ (Kaye & Laby 1973), K_e is the diffusion constant for water vapour in air: at 20°C is $21.2 \times 10^{-6} \text{ m}^2 \text{ s}^{-1}$ (Holsoft's Physics Resources Pages 2001).

Measurements taken by Watts (1983) on grassy fields under a range of conditions indicate that B is uncertain by up to 30%. This led to an uncertainty in L_E of 5% (Fritschen 1965).

The equipment is complex to position and operate in the field. Over water, there would be many more factors to overcome to position and operate the sensors. This technique has been superseded by Eddy Correlation for water storages (Craig 2008)

Eddy correlation

The Eddy Correlation technique requires accurately measuring above a water surface the wind speed in 3 dimensions (with rapid response anemometers), humidity and temperature. An example of such a system is given in Figure 1.10.



Figure 1.10 Commercial CSAT3 Three dimensional sonic anemometer retailed by Campbell Scientific.

Vertical components of air velocity can originate from one of three sources (Van Dijk 2003). If there is a heat flux from water to air, the air will rise in convection currents. Evaporating water produces water vapour with a volume of approximately three orders of magnitude greater than the original liquid water volume. This expansion has the effect of displacing the atmosphere upwards. When a mole of water weighing 18g (0.018 litres) vaporizes it takes up a volume of 22.4 litres, so a thickness of 18 mm expands to a water vapour layer 22.4 metres thick. As this layer is forming the

air is pushed upwards. Wind speed needs to be taken into account as deceleration of moving air by friction at the surface induces a negative vertical velocity. This produced compression of the slowed air and, a volume sink is created near the surface.

The vertical latent heat flux can be found using (Craig 2008):

$$L_E = \rho L w q \quad (1.20)$$

where L_E is the instantaneous vertical heat flux (W m^{-2}), ρ is the density of air, L is the instantaneous latent heat of vaporization of water (J kg^{-1}), q is the instantaneous specific humidity (kg kg^{-1}) and w is the vertical wind speed.

Even with careful calibration of present day equipment, Eddy Correlation estimates of flux measurements may be off by more than 15% (Eugster, McFadden, & Chapin 1997). However it compares favourably with other methods and despite being expensive, this equipment is particularly suited to measurements close to open water surfaces (Craig 2008).

1.5 Evaporation mitigation techniques

Evaporation and seepage are the two major causes of loss from water storages. The cost of addressing either needs to be weighed up against the price of water saved. The cost of techniques to save water can be estimated; however the price of water is more unpredictable, depending on rainfall. Figures for the tendered price of water in the Murray-Darling basin for 2009 (DEWHA 2010) vary between \$200 and \$3000 per ML. This large variation is an indication of the difference between high-security water, that which the availability is certain and reliable, and low-security water, the availability of which largely depends on seasons. Economic considerations largely dominate the selection of approaches taken to reduce evaporation from water storages. There are a wide variety of evaporation mitigation techniques available. These can be grouped into 4 basic classes; biological surfaces (e.g. water-weeds, shelterbelts), physical shade structures, physical floating covers and chemical layers.

1.5.1 Biological methods

Aquatic plants and nearby vegetation can reduce evaporation by, reducing any or all of incident solar radiation, surface area or wind speed. Whenever plants are used for this purpose, the water drawn up and used for transpiration needs to be taken into account. Trees and plants on the banks, which may be drawing water for transpiration such as Eucalyptus and Pine trees could not have an reducing effects large enough to offset the water they transpire as a fully grown trees draw around 100-200 litres day^{-1} (Wullschleger, Meinzer, & Vertessy 1998).

Floating plants

Floating aquatic plants such as Water Lily (*Nymphaea odorata*), Small Duckweed (*Lemna minor*), Giant Duckweed (*Spirodela polyrhiza*) and Water meal (*Wolffia columbiana*) (Figure 1.11) offer a possibility of lowering the net evaporation of water storages by forming a physical barrier to the flux of vapour, preventing the interaction of air currents with the boundary layer and reducing incident solar energy (Ramey 2004).



(a) Close-up photo of Duckweed (*Lemna minor*)



(b) Duckweed (*Lemna minor*) complete with ducks



(c) Water meal (*Wolffia Columbian*) (IFAS 2009)



(d) Water Lily (*Nymphaea odorata*)



(e) Water Hyacinth (*Eichhornia spp*)



(f) Water lotus (*Nelumbo nucifera*)

Figure 1.11 Various biological (plant) covers.

However not all water plants effectively reduce evaporation rates. For example, Water Hyacinth (*Eichhornia spp*) and Water Lotus (*Nelumbo nucifera*) both produce leaves that are positioned above,

rather than on the surface. This actually increases the transpiration surface area and does little to reduce storage surface area, ultimately leading to an increase in evaporation rates (Ramey 2004). Ramey reports the evaporation-reducing effects of a number of plants, including Water lily (*Nymphaea odorata*) nil, Small duckweed (*Lemna minor*) 10%, Water meal (*Wolffia columbiana*) 11% and Giant duckweed (*Spirodela polyrhiza*) 15%, while Phaovattana(1995) has shown duckweed can reduce evaporation by up to 9%.

Introduction of an exotic plant to a water storage for the purposes of evaporation reduction may have additional undesirable effects, including affecting water quality, reducing the storage’s suitability for recreation and overwhelm natural flora dynamics (NPSI 2005/4 April).

Wind breaks

Wind breaks consisting of tree ‘shelterbelts’ reduce the wind speed by 80% for a distance of 5 times the height of the trees. The effects of trees on reducing wind speed can extend horizontally downwind of the trees by as much as 50 times the tree height (Helfer, Zhang, & Lemckert 2009). However it has been reported that the resulting increased turbulence and ambient temperature in the downwind zone of the wind breaks tends to increase, rather than reduce evaporation from large water surfaces (Cleugh *et al.* 2002).

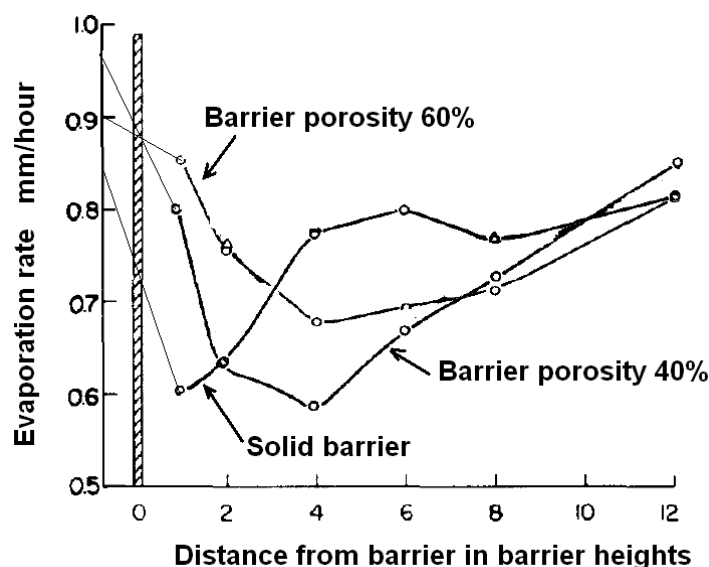


Figure 1.12 Effect of porosity of wooden slat fence on evaporation. Adapted from Skidmore & Hagen (1970).

These results of Cleugh *et al.* are in contrast to results gained by Skidmore & Hagen (1970), who modelled wind shelters on a smaller scale using a 2.44 m high slatted wooden fence and small evaporating troughs. This type of fence was used so that slats could be added or removed to vary the ‘porosity’. They found that a solid barrier actually reduces evaporation by less than a barrier with 40% porosity and this was attributed to the higher turbulence associated with the solid barrier. They also measured an increase in air temperature downwind from the barrier, again leading to increased evaporation (Figure 1.12). From a management perspective, water use by the trees also needs to be factored in to total evaporation savings (Frenkiel 1965), as does any potential damage by the roots to the storage itself. Whilst shelterbelts may produce some evaporation savings for

small water storages (e.g. small farm dams), only minor evaporation reductions could be achieved for large dams (Helfer, Zhang, & Lemckert 2009).

1.6 Physical Shade structures

Reducing the solar radiation using suspended material reduces water temperature and the wind speed.

1.6.1 Shade cloth

Shade cloth suspended above the surface of water storages (Figure 1.13) has the effect of reducing solar radiation reaching the surface, lowering wind speed and increasing the air humidity under the cover. Tests indicate evaporation reduction on small dams to be as large as 59-76% (Jennison 2003). From a logistical perspective, these structures need to be supported above the water, adding considerable difficulty and cost, especially for large storages (even moderate farm dams).



Figure 1.13 Two examples of suspended shade cloth structures over water storages (a) NetPro shadecloth (Netprocanopies 2010) and (b) Suspended shadecloth in East Gippsland Victoria (Jennison 2003).

1.6.2 Floating devices

Floating physical covers for reducing evaporation generally have two forms; continuous covers and modular covers. These devices are sun-blocking devices with the added advantage of reducing air flow across the surface of the water and reducing the evaporative surface area (Jennison 2003). Continuous sheeting options such as E-VapCap is similar in structure to ‘bubble wrap’ sheeting, only with white upper surface and dark lower surface (Figure 1.14(a)). The product is reputed to reduce evaporation by 100%, costing approximately \$6.60 m⁻² (in 2002), capable of reducing or preventing algal growth. High winds causing a rough surface, however can be a problem (Jennison 2003).

Modular devices floating on the surface need little structure to hold them in place, They generally show good evaporation reducing ability (Jennison 2003), however are quite expensive to purchase initially. For example, Nylex Aquacap covers are made up of interlinked, injection moulded, white polypropylene disks that float semi-submerged on the surface of the water are shown in Figure

1.14(b). They are about 1.1 m in diameter with a curved surface on top and fit together to cover up to 80% of the surface area. Aquacaps have the potential to reduce evaporation by an average of about 70% annually. Estimated costs of installation in 2002 were around \$16 m⁻² (NPSI 2005/4 April). They also lower solar radiation penetrating the water and reduce oxygenation of the water to some extent.



(a)



(b)

Figure 1.14 Examples of (a) Continuous floating structure (E-VapCap sheeting) and (b) the Aquacap floating modular system.



Figure 1.15 Aqua Armour floating modular system Source: (Aqua Armour 2010).

Aqua Armour, picture in Figure 1.15, is a floating modular system made by Aqua Guardian Group. The manufacturers claim an evaporation reduction of up to 88% (Aqua Armour 2010). This system is similar to Aquacap, only with hexagonal shape, so that the units lock together. The individual units measure 1.2 m in diameter. When installed they take on water for stability and weigh about 60 kg. The cost is \$30 m⁻², making them unsuitable for all but the smallest storages' (E. Schmidt 2010, pers. comm., June).

1.7 Chemical evaporation reducing layers: Monolayers and thin films

Chemical evaporation reducing layers encompass compounds created for the purpose of reducing evaporation rates from water surfaces. The layers generally fall into two classes, surface-active films and self-assembling monolayers.

These classes are defined on the basis of their thickness and assembled state when covering the water surface. The area of coverage is often called a *slick*.

Surface active films are composed of insoluble molecules which have an affinity for the surface interface. They tend to form an amorphous material of any thickness on the surface of water. An example is the use of dimethyl siloxane silicone oil in a commercially available product called “Aquatain”.

Self assembling monolayers on the other hand, are long-chain organic compounds that distribute themselves on top of a water surface at only one molecule, a few nm thick. The term ‘self assembling’ originates from the amphiphile hydrophilic/hydrophobic nature of the molecular chains; the hydrophilic ‘head’ and hydrophobic ‘tail’ ensures they position themselves vertically on the water surface packing into an ordered crystal, and tending not to form multiple layers. Two most favoured compounds used for evaporation control are the alcohols hexadecanol ($C_{16}H_{33}OH$) and octadecanol ($C_{18}H_{35}OH$) (Brown 1988), although more complex variants are currently in development. The following sections discuss each class of layer in turn.

1.7.1 Surface active layers

These range from silicone oils and polymers to aviation fuel and crude oil slicks, which have hydrophobic qualities making them insoluble in water. These layers have no set structure (e.g. molecular alignment) and act to reduce evaporation by the shear thickness of the film. They also generally reduce surface tension, increase surface viscosity which have effects on waves, wind structure and evaporation reduction. In fact, surface active layers can be identified by the fact that they significantly reduce the surface tension (Hühnerfuss, Walter, & Kruspe 1977). Goldacre (1949) tested the surface tension of many water bodies around England, finding that most are covered with a slick of either biological or anthropogenic origin.

In order to gain effective evaporation reduction, these films need to be of the order of micrometers thick, such as the recommended thickness of Aquatain, a silicone oil at around 1 μm . (Ultimate Products (Aust) Pty Ltd 2009).

Owing to their thickness, surface active layers are generally easier to observe, either through changes in wave height due to increased damping, or measurable alterations to the reflectivity of incident radiations. Fingas & Brown (2000) point out that the most widely used method for detection of oil spills is still human vision methods, despite results being variable. Visual methods of detection of oil slicks by observing the sheen of oils, called “sheen surveillance” were developed by Taft, Egging, & Kuhn (1995) as reported by (Wells, Butler, & Hughes 1995) in which the type of oil making up the spill could be determined by the appearance of the sheen which was best observed from aircraft. These layers also cause wave damping, which can be detected using Synthetic Aperture Radar (Section 2.5.1) and numerous other remote detection methods are actively being researched due to the importance of being able to detect and map oil spills (Karantzas & Argialas 2008N). Detection methods used for surface active films are not the aim of this thesis, as this work is not concerned with thin films *per se*. However comparisons will be made, and some of the techniques will be revisited later owing to their applicability to detecting self-assembling monolayers; the main thrust of this thesis.

1.8 Properties of Monolayers

Monolayers are layers one molecule thick of long-chained, organic compounds comprising a hydrophobic carbon tail connected to a hydrophilic, ionically bonded head. The polar charge in the head results in hydrogen bonding with adjacent water molecules. Polar functional groups include alcohol (-OH), carboxylic acid (-COOH), amine (-NH₃⁺), -phosphate (PO₄⁻) and aldehyde (CO) (Troy 2006:294). The hydrophobic carbon tail ensures the molecules stand ‘upright’; that is the head bonded to the surface of the water and the tail extended vertically above the water surface. The molecule as a whole is called an *amphiphile*, the original Greek meaning of which implies to love both water and oil.

From a simplistic viewpoint, the ‘effectiveness’ of a monolayer is based on a combination of the ability of the molecules to form a film by packing closely side by side with each other without stacking and the thickness of this film, ultimately determined by the molecular chain length.

Experience has shown that to be an effective, water insoluble monolayer, the hydrocarbon chain attached to the polar group should possess more than 12 ‘units’, that is (CH₂)_n, where n > 12 (La Mer & Healey 1965). If the chain is shorter, though still insoluble in water, the amphiphile on the water surface tends to form water-soluble *micelles*. On the other hand if the length of the chain is too long the amphiphile tends to crystallize on the water surface and consequently does not form a monolayer. It is difficult to determine, *a priori*, the optimal length for the hydrocarbon chain because its film forming ability also depends on the polar part of the amphiphile. Rosano and La Mer (1956) and Garrett (1971), testing evaporation through monolayers on small droplets, found that straight chain alcohols and acids with alkyl chains free of double and triple bonds formed the most densely-packed monolayers.

In order to discuss the performance characteristics of monolayer, some basic physical properties must be introduced.

1.8.1 Surface Tension

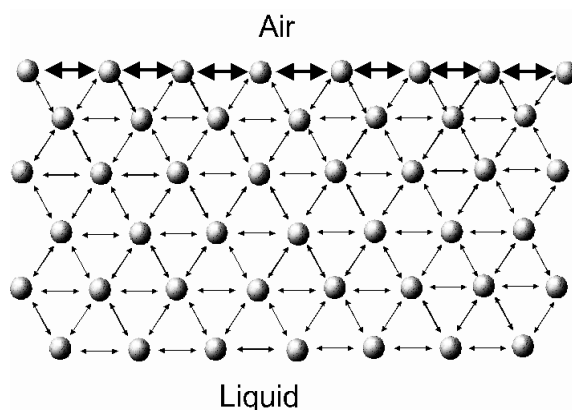


Figure 1.16 Adhesive forces within a fluid causing surface tension. Source: (KSV 2009).

The cohesive forces on a molecule in the centre of a liquid are relatively isotropic. That is, the molecules are pulled equally in all directions by neighbouring molecules (Figure 1.16). However at the edge of a liquid/air interface there is an unbalanced force pulling the molecule into the liquid

creating a force which acts to reduce surface area. This force per unit length of surface is called surface tension γ with units of N m^{-1} . Surface tension can also be described in terms of the energy required to increase the area of the surface where it is referred to as surface free energy (J m^{-2}).

Measuring surface tension

There are many methods of measuring surface tension. One widely used technique for measuring surface and interfacial tensions accurately is the Wilhelmy plate method (Erbil 2006). A small plate of known physical size is suspended into the surface of a liquid allowing the meniscus to adhere as shown in (Figure 1.17 (a)).

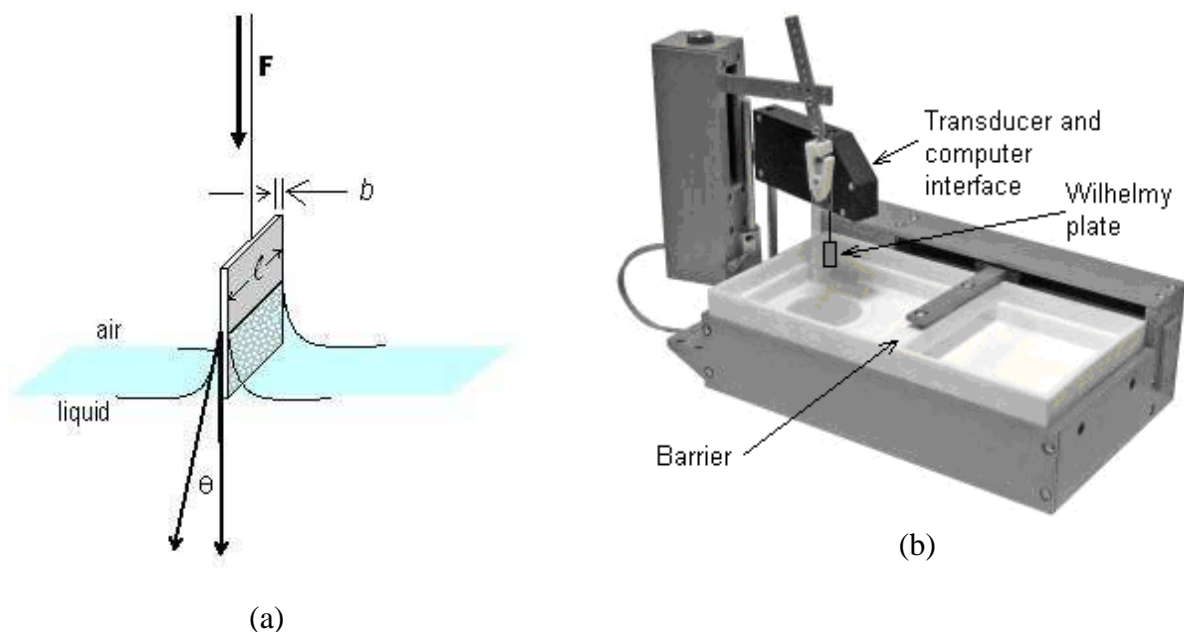


Figure 1.17 (a) Close up of meniscus behaviour on the Wilhelmy plate. (b) A Langmuir trough. Usually these trough are Teflon lined with a moveable barrier to alter surface area. The surface tension is usually measured using a Wilhelmy plate attached to a transducer.

The surface tension can be inferred from the observed additional weight of the entrained meniscus of the fluid pulling the plate downwards using:

$$F = \gamma 2(l+b) \cos \theta \quad (1.21)$$

where F is the increased weight, l and b are the wetted length and breadth of the plate, θ is the meniscus contact angle with the plate. If the plate is very thin this reduces to the Wilhelmy equation:

$$\gamma = \frac{F}{2l \cos \theta} \quad (1.22)$$

where the contact angle θ for water or monolayer approaches zero.

Water possesses an exceptionally high value of surface tension compared to other liquids and consequently it makes a very good subphase for any surface layer, such as monolayers, which reduces surface tension.

Surface tension measurements and characterising monolayers are often performed on Langmuir troughs, as shown in Figure 1.17(b). These are devices used to provide the controlled conditions necessary to measure surface tension, and to allow external parameters such as the interacting surface area to be changed. These troughs are quite small; a medium size trough retailed by Nima Technology (2009) has inner dimensions of 364 (L) \times 75 (W) \times 4 (H) mm and generally lined with the extremely hydrophobic product, Teflon. A moveable barrier driven by a stepping motor is used to alter surface area, while at the same time the surface tension can be monitored using the Wilhelmy plate transducer, which has a specified accuracy of 4 μNm^{-1} (Nima Technology 2009). Langmuir troughs, and their integral Wilhelmy plate sensors are key tools for examining the physical characteristics of monolayers described in the following section.

1.8.2 Surface Pressure π

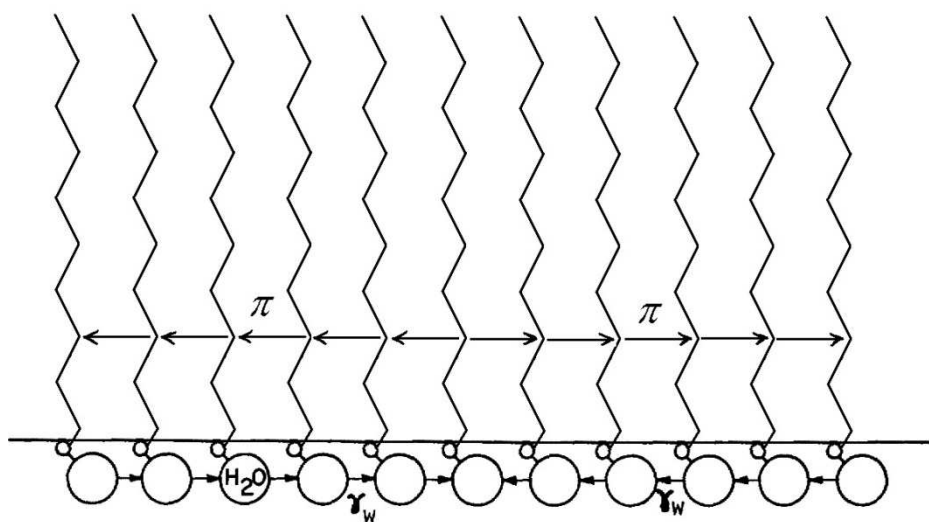


Figure 1.18 Surface pressure π of monolayer. Adapted from Gainer, Beard, & Thomas (1969).

When an insoluble solution comprising a monomolecular amphiphile in a water-insoluble solvent is placed on an infinitely large water surface, the solution spreads to cover the available area. Under these conditions the monolayer has little effect on the surface tension of water. If the available surface area of the monolayer is progressively reduced by a moving barrier system (for instance, using a Langmuir trough), the long chains of the molecules move closer to each other, exerting a repulsive force. This repulsive force acts to oppose the surface tension of the surface as depicted schematically in Figure 1.18. The surface tension of water, shown as γ_w is drawing the monolayer molecules together, while the repulsive “surface pressure”, indicated as π , forces the molecules apart.

The repulsion between the vertical parallel molecular chains reduces the effective surface tension of monolayer covered water. As an important property of surfactant films, the change in surface tension of pure water, when covered with a monolayer, is often discussed in terms of surface pressure π (Gladyshev 2002) which is defined by:

$$\pi = \gamma_w - \gamma. \quad (1.23)$$

Here γ_w is the surface tension of water in absence of a monolayer (72 mN m^{-1} at 25°C) and γ is the surface tension with the monolayer present. For example, a hexadecanol monolayer with excess crystals floating on the surface displays a maximum reduction in the surface tension of water to 32 mN m^{-1} , or a maximum (full) surface pressure π value of 40 mN m^{-1} . Similarly octadecanol has a full surface pressure of 35 mN m^{-1} (Table 1.2).

1.8.3 Surface Pressure- Area (π -A) Isotherms

When alterations to the surface area of a liquid such as pure water do not affect the surface tension, it is said to possess zero dilational elasticity (Behroozi *et al.* 2007). Evaporation-reducing monolayers have a non-zero dilational elasticity because work is done in changing the surface area as the surface tension is altered. Changes in surface tension plotted against area/molecule are called isotherms, often discussed in terms of measuring the surface pressure as a function of the area of water surface available to each molecule. This is often measured with a Langmuir trough/Wilhelmy plate apparatus described in the preceding section. The shape of the resulting isotherm is used to characterize monolayers. A typical isotherm for monolayers is shown in Figure 1.19, along with a simple terminology used to classify different monolayer phases proposed by Harkins (1952).

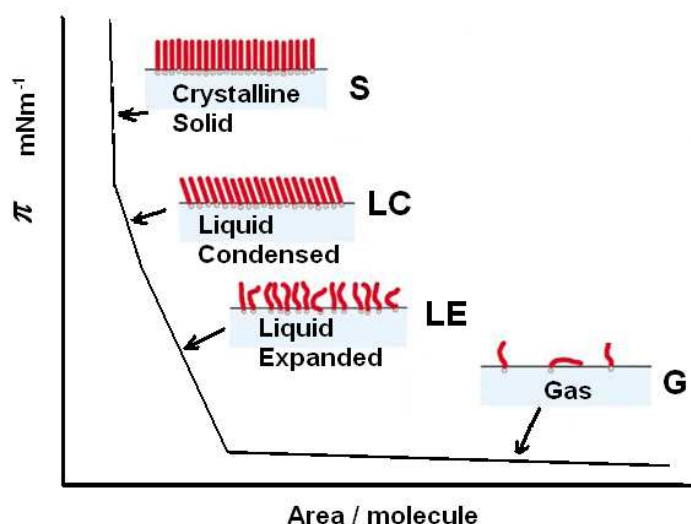


Figure 1.19 Phases of an isotherm for a typical monolayer. (Barnes & Gentle 2005).

At high area/molecule values, the monolayer molecules exert little force on each other and can be considered as existing in a two dimensional gas state labelled (G). Here they have almost no effect on surface tension. As pressure is applied to the surface by moveable barriers, the monolayer carbon chains begin to be forced upward, as the area/molecule decreases. This has the effect of increasing the surface pressure and forcing a phase transition to that of an ‘expanded liquid’ (LE). Further reduction of surface area leads to the attainment of a ‘condensed liquid’ phase (LC).

On further compression of the monolayer surface area, the chains line up vertically, and then start to repel each other, creating a near vertical line on this region of the isotherm as the surface pressure increases. This is called the ‘solid phase’ (S).|

Under still further compression the vertical alignment of the chains is destroyed; the monolayer collapses unpredictably as it may again crystallize or form areas of amorphous multiple layers (so-called ‘stacking’). Here the surface pressure area/molecule curve becomes a wavering horizontal

line; the monolayer cannot sustain any more surface pressure than its maximum (not shown in Figure 1.19 due to the unpredictability). This stacking phenomenon is a practical problem in deploying monolayers on water storages (as will be discussed later). Wind pushing the monolayer to the down-wind side of storages, compresses it and produces this very effect.

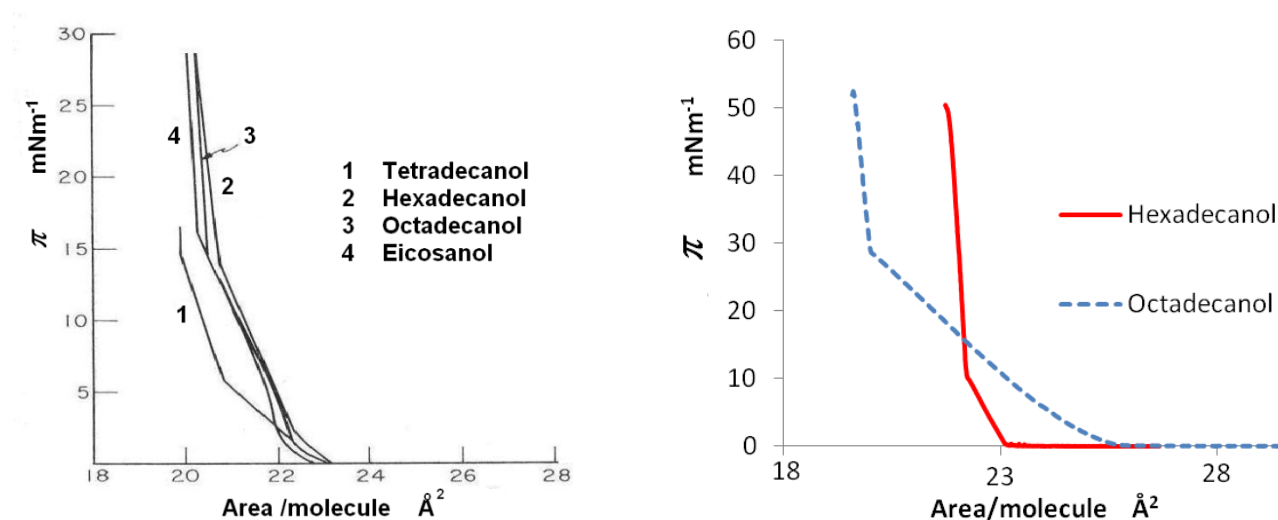


Figure 1.20 (a) Pressure-area π - A isotherms for long chain alcohols at 20 °C, measured by Nutting and Hawkins (1939). (b) π - A isotherms for hexadecanol and octadecanol measured by M. Herzig (Pers. Comm. 2009).

Examples of π - A isotherms for long chain alcohol monolayers are shown in Figure 1.20(a) measured by Nutting and Hawkins (1939). These show that there very little difference in phases between the monolayers of primary alcohols for chain lengths of 16, 18 and 20 carbon atoms. More recent data Figure 1.20(b), obtained by Herzig (2007) using a computer driven Langmuir trough shows the phase differences more clearly. A noticeable trend is that, the longer the length of the carbon chain, the more pressure needs to be exerted on the surface to effect a transition into the solid phase.

1.8.4 Spreading Pressure F_0

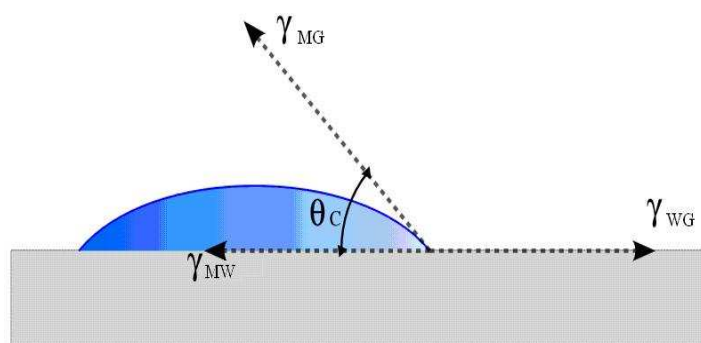


Figure 1.21 Contact angles at the edge of monolayers.

The ability of a monolayer to spread on the surface of water is largely dependent on the contact angle that is made with water at the edge of particles of amphiphile. This angle is formed as a result of an equilibrium formed between the surface tensions of water under the monolayer γ_{MW} , surface

tension of free water γ_{WG} and the surface tension of the monolayer γ_{MG} . The relationship between the forces are depicted in Figure 1.21.

If the forces are resolved in the horizontal direction, we have:

$$F_0 = \gamma_{WG} - \gamma_{MW} - \gamma_{MG} \cos \theta \quad (1.24)$$

where F_0 is the spreading pressure at the edge of a monolayer. The units of F_0 are mN m^{-1} , however this becomes a pressure when the added dimension of length around the monolayer is considered.

The materials used for monolayers generally have a low contact angle because of the hydrophilic group. When spread at only one molecule thick, the contact angle $\theta \sim 0$ and Equation 1.24 becomes (Garrett & Barger 1970):

$$F_0 = \gamma_{WG} - \gamma_{MG} - \gamma_{MW} \quad (1.25)$$

Clearly, F_0 needs to be > 0 for all monolayer preparations, so that the monolayer will spread completely. The size of this coefficient will determine the spreading rate. If the F_0 of a monolayer is not sufficiently high, it can be increased by mixing it with a volatile hydrophobic solvent, which later evaporates, leaving the monolayer in place.

Garrett & Barger (1970) have suggested the possibility of using monolayers, to lower the surface tension of water surrounding an oil slick in order to contain its spread. The main problem they encountered was finding a substance that would be insoluble in both water and the oil substance of the slick. They suggest using oleyl alcohol, though it has a surface pressure of 33.8 mNm^{-1} , which is very little above the spreading pressure of oil slicks at $25\text{-}33 \text{ mN m}^{-1}$. The surface pressure of oil slicks varies depending on the thickness (Kaiser 1972), however at the edge the spreading pressures have been determined by Garrett (1965), who found pressures of typical light oil slicks to be around 33 mN m^{-1} , while heavy, more viscous oil such as diesel had spreading pressures around 25 mN m^{-1} . The initial spreading rates of alcohols was measured by Deo (1961) (Figure 1.22), showed a decrease with increasing chain length. Additionally the evaporation resistance increases with chain length, so there is a trade off between the two, leading to either hexadecanol or octadecanol as being the most useful.

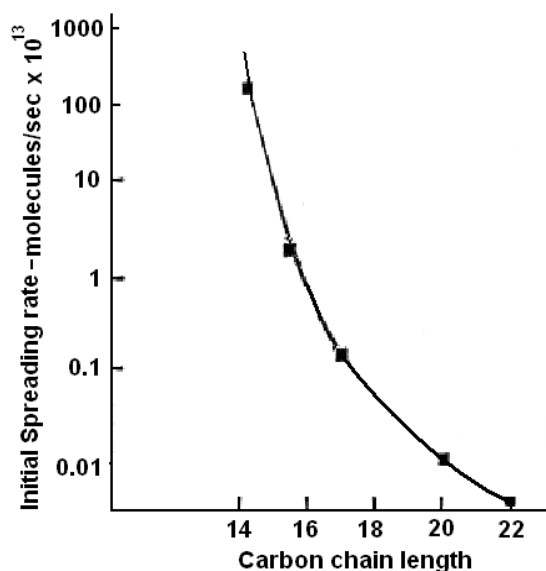


Figure 1.22 Initial spreading rate of the primary alcohols. Source; (Deo *et al.* 1961).

In practice, there are two processes which occur in forming monolayer coverage. The monolayer material needs to transfer from solid (or liquid) to an adhering monolayer on the surface, called the *spreading rate*. The surface pressure then acts to move the monolayer across the surface by surface tension forces as described above. This process is often measured in terms of *spreading speed*. This is the speed at which the leading monolayer edge moves away from the dispensing position. Initially it is high, and decreases with increasing distance.

Measurement of the spreading rate has been carried out by Deo *et al.* (1961) from the solid state for the primary alcohols. They prepared a rod of each sample of material of a standard size, which was placed into the water surface of a small container. The time taken to raise the surface pressure by 1 mN m^{-1} was noted so that the transfer rate could be calculated.

With increasing chain length, the alcohols are more viscous hence have lower spreading speed and are less volatile. While tetradecanol (C_{14}) alcohol covers areas very quickly, it has a much lower evaporative resistance. By comparison, docosanol (C_{22}) alcohol has a much higher evaporation resistance; however it takes much longer to spread and to self-repair 'damaged areas' in the film.

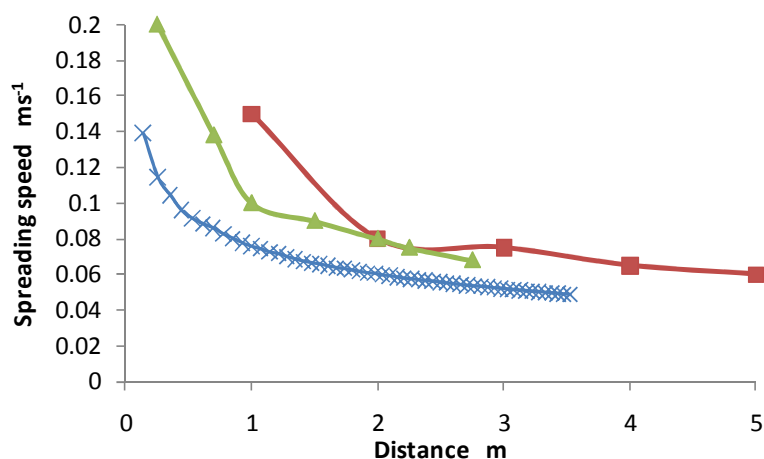


Figure 1.23 Spreading speed of bile (30 g l^{-1}) (■) Hale & Mitchell (1997), oleyl alcohol (▲) Garrett & Barger (1970) and octadecanol (×) G. Brink (Pers. Comm. 2009).

Spreading speeds gathered by researchers for monolayers, generally showed one of two shapes depending on the method used to make measurements. The first method uses a relatively small trough and the sample is placed at one end. This produces a noticeable change of velocity gradient at between 1-2 m from the edge for commonly used monolayers. This feature can be seen in Figure 1.23 for measurement of bile (30 g l^{-1}) (Hale & Mitchell 1997) and oleyl alcohol (Garrett & Barger 1970). It is presumably caused by adding the monolayer material in close proximity to the side of the trough. The spreading occurs in both directions (towards the adjacent edge, and towards the centre of the trough), pushing the initial material towards the centre of the trough. Since the leading edge of the monolayer is being monitored, it is falsely high, while the initial material is still moving. Once there is full pressure both sides of the initial material it ceases to move and the second gradient is followed. A diagram of this effect is shown in Figure 1.24.

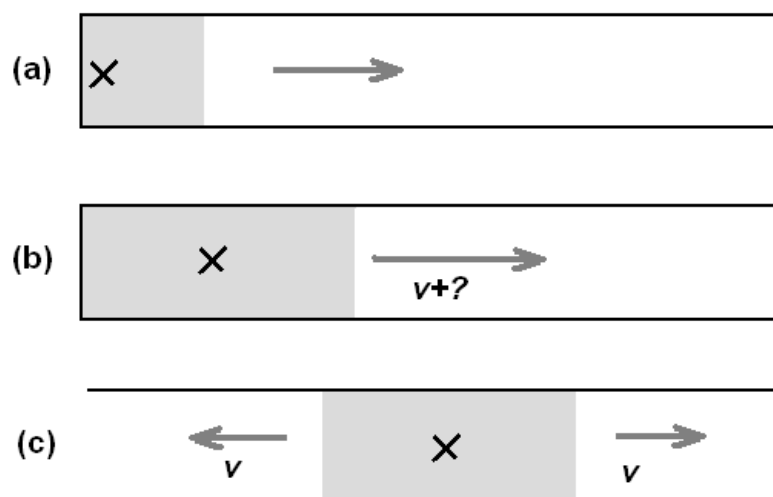


Figure 1.24 The initial high higher gradient in the spreading velocity originates from movement of the monolayer material, when the monolayer material is placed beside an edge of a trough. Troughs (a) and (b) are troughs bounded on the left side, while (c) is open on both sides. If the monolayer material is placed near the edge, as in (a), the material itself is forced away from the edge as it spreads (b). This is very noticeable with hexadecanol crystals. The spreading edge away from the edge is travelling at a higher speed until the material comes to a standstill. Placing the material away from an edge, as in (c), gives the true spreading speed and also gives a

smoother speed distance gradient.

Data produced by G. Brink (Pers. Comm. 2009) in a large tank with octadecanol deposited at the centre, instead of near an edge does not show this feature, but a gentle decrease of speed. His data shows that following the application of a 'point' of monolayer on the water surface, there is an initial speed of $\sim 0.15 \text{ m s}^{-1}$ followed by a smooth decay in speed to $\sim 0.04 \text{ m s}^{-1}$ as the spreading radius increases. This should be more representative of the behaviour under field storage conditions.

On a larger scale, the width of a slick spread in the direction of the wind depends including water temperature and amount of product initially available to spread (McArthur 1962). The width is also related to the initial spreading speed. Solvents may be used to increase the spreading rate, however they may decrease the evaporation resistance, and also increase the tendency of the film to collapse (see Section 1.8.9).

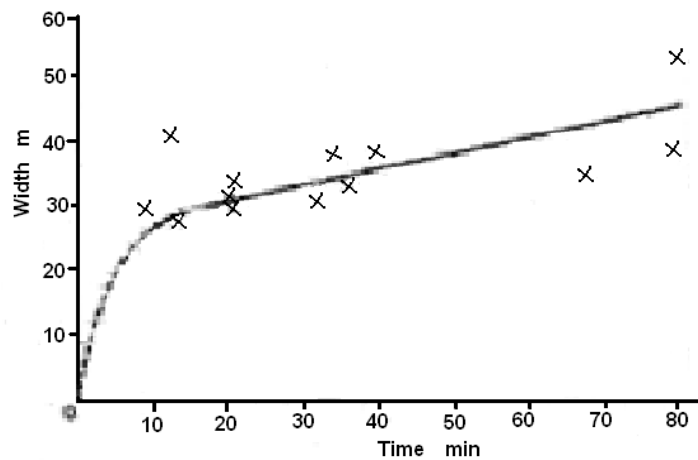


Figure 1.25 Measured width of a surface of hexadecanol slicks as a function of time from initiation. Adapted from McArthur (1962).

The width of hexadecanol monolayer coatings on water at around 10°C and given typical wind speeds of $2\text{-}4 \text{ m s}^{-1}$, were measured by McArthur (1962) in Loch Laggan, in Scotland. The results, depicted in Figure 1.25, show an initial more rapid rate of spread, probably due to the higher initial rate of spreading of 155 mm s^{-1} (Birdi 1934) tapering off as the spreading edge moves away from the source material. At a distance of $\sim 25 \text{ m}$ another process seems to be responsible, spreading at a lower linear rate. It would appear that the spreading force supplied by the monolayer material no longer reaches this distance and the edge spreads out of its own accord from forces occurring at the edge of the slick. McArthur (1962) also comments that larger wind speeds result in narrower slick widths and that higher water temperature would result in wider slicks.

1.8.5 Evaluating the Effectiveness of Evaporation Reducing Films

Two methods are frequently used in comparing the evaporation reducing qualities of surface films (Noe & Dressler 1967). The first is a laboratory method which measures the specific resistance of the surface under no-wind conditions compared to a clear water surface under similar no-wind conditions, called the *specific evaporation resistance*. It can be measured by placing a desiccant (LiCl) at a known distance (several mm) above the water surface and measuring the increase in

weight of the desiccant as it absorbs water vapour after a designated time (Archer & La Mer 1955). Measurements performed in this way for both clear water and layer-covered water can be substituted into an equation developed by Langmuir and Schaefer (1943) to obtain a value for the specific evaporation resistance of the monolayer:

$$r = a(e_0 - e) \cdot \left(\frac{t}{m_m} - \frac{t}{m_w} \right) \quad (1.26)$$

where a is the area of water surface under study, e_0 and e are the equilibrium concentrations of water vapour above the clean water surface and the film-coated surface, respectively, $\frac{m_m}{t}$ is the evaporation rate of water surface covered with the film and $\frac{m_w}{t}$ is the evaporation rate of pure water. The term $(e_0 - e)$ is the driving force of evaporation across the surface layer, with units kg cm^{-1} . Equation 1.26, with its driving term $(e_0 - e)$, and its flow/current term $\left(\frac{t}{m_m} - \frac{t}{m_w} \right)$ is analogous to Ohm's law in electricity, namely $R = \frac{V}{I}$.

The **Evaporation reduction** (Noe & Dressler 1967) is an alternative quantity, usually expressed as a percentage given by:

$$\text{Evaporation reduction} = \frac{m_w - m_m}{m_w} \quad (1.27)$$

where m_w and m_m are the evaporated masses over a specific time for a water body with a clean water surface and with a monolayer respectively.

The specific evaporation resistance term tends to be used to characterize films under laboratory conditions, while evaporation reduction tends to be used to gauge the total effectiveness of the monolayer to preserve water in the field. Data obtained for both and the important differences will be discussed in the following sections. In practical terms on large storages only the evaporation reduction term is used, as in Chapter 5, as there is too many processes occurring to characterise the surface. This leaves the important measureable; evaporation reduction to determine effectiveness.

1.8.6 The impact of monolayers on evaporation rates

There are two theories which could explain the evaporation of water through an absorbed monolayer:

The diffusion theory

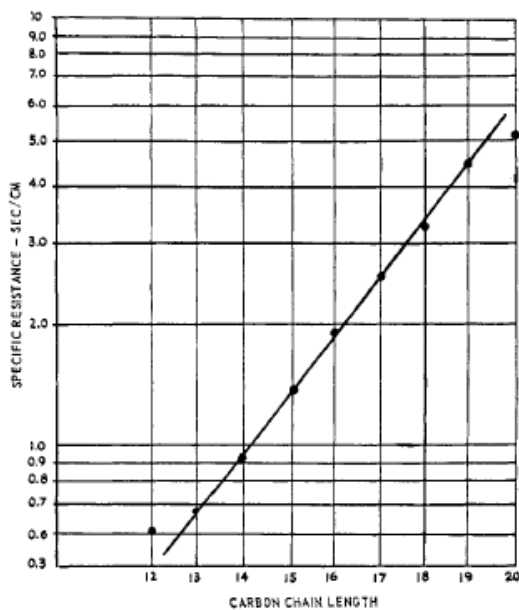
This theory of evaporation is based on Fick's first law (Barnes & La Mer 1962:19; Ward & Trimble 2004). It quantifies the movement of molecules from a region of higher concentration to a region of lower concentration. This equally applies to the diffusion of water molecules through surface oil films floating on water (Langmuir & Schaefer 1943) or through vapour diffusion layer that exists

just above the surface of water into the open air. If the system is time independent, that is, when the concentration of the layer within the diffusion volume does not change with respect to time, the diffusion flux J ($\text{moles m}^{-2}\text{s}^{-1}$) of water through the layer will be proportional to the concentration gradient.

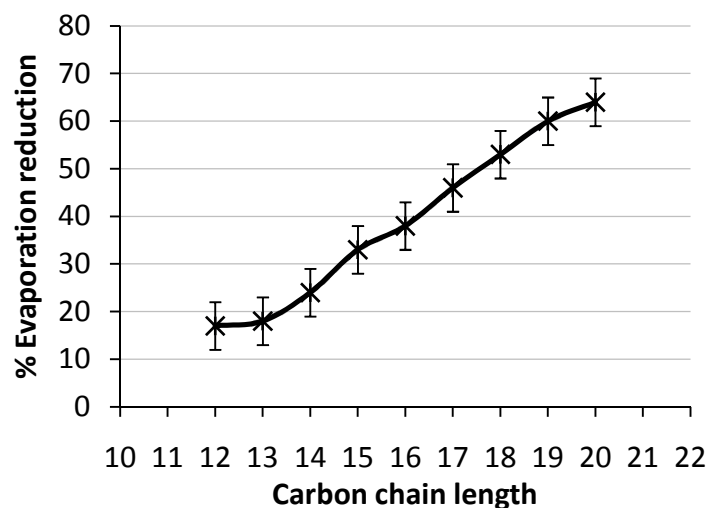
$$J = -D \frac{\partial \phi}{\partial x} \quad (1.28)$$

where D is the diffusion coefficient ($\text{m}^2 \text{s}^{-1}$) and $\frac{\partial \phi}{\partial x}$ is the concentration gradient (mol m^{-4}) through the layer of thickness x . Fick's diffusion law is observed to be relevant to relatively thick surface active films such as oils (Langmuir & Schaefer 1943) but not to a monolayer which is only one molecule thick (Barnes & La Mer 1962).

However the relationship between monolayer thickness; determined by carbon chain length and specific resistance, appears to be exponential in nature (Archer & La Mer 1955; La Mer 1962) as shown by data gathered by Noe (1967) in Figure 1.26(a). Thus monolayers do not appear to obey Fick's law. To explain the behaviour of the monolayers the characteristics of the molecule need to be taken into account.



(a)



(b)

Figure 1.26 (a) Relation of specific evaporation resistance to chain length for even and odd primary alcohol monolayers, showing the exponential behaviour. Source; Noe *et al* (1967). (b) Relation of chain length to % evaporation reduction at 30 °C. Data extracted from Noe *et al* (1967).

Interestingly there does seem to be a linear relationship between the evaporation reduction and carbon chain length as reported by Noe & Dressler (1967) in Figure 1.26(b) and in data obtained by Foulds & Dressler (1968).

The energy barrier theory

An energy barrier limiting vaporization accounts for this exponential relationship shown in Figure 1.26(a). This was first suggested by Langmuir and Schaefer (1943) and later developed by La Mer *et al* (Navon & Fenn 1971). It explains the monolayer evaporation resistance in terms of an activation energy barrier to diffusion through the monolayer. This equates the evaporation resistance to the energy acquired by water molecules which have to pass through a closely packed solid crystal in order to vaporize. The resistance to evaporation, an intrinsic property of the surface, can be written as:

$$r = ke^{E/RT} \quad (1.29)$$

where r is the specific resistance, E is the experimental activation energy. For the alcohols the activation energy is 1154 J/mole for each methyl CH_2 group on the chain added to 27 000 J/mole for the head group (Barnes & La Mer 1962), R is the gas constant, T is the temperature (K), and k is a constant. Experimental data relating the natural log of the evaporation resistance r and surface pressure π appears to be linear within the limits of the particular surface state (solid S or liquid condensed LC) (Barnes & La Mer 1962:21) and this has been confirmed in the results obtained by Barnes & La Mer (1962) and La Mer & Aylmore (1961) in Figure 1.27. These figures show that specific resistance is proportional to surface pressure above 15 mN m^{-1} . This provides evidence in favour of the energy barrier theory, showing that r is related to π . Moreover, it shows that maximum effectiveness of monolayers, is gained by maximising π .

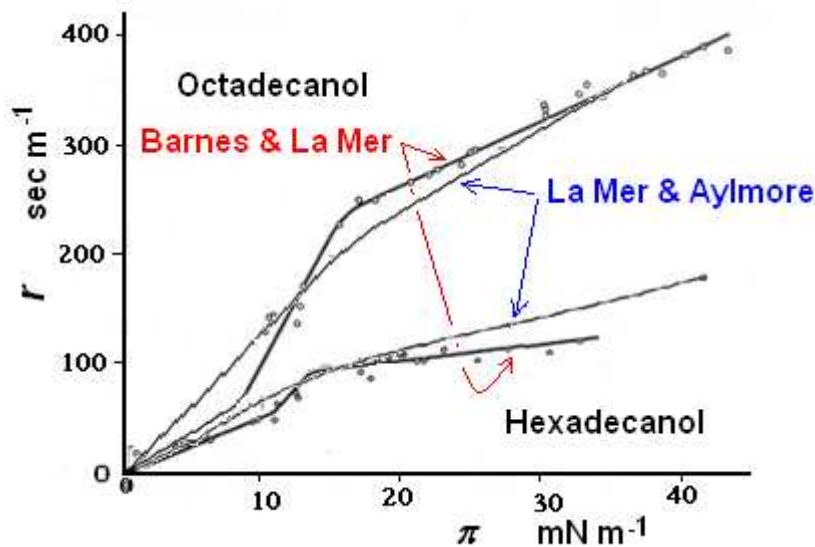


Figure 1.27 Specific resistance r for the full range of surface pressures π for hexadecanol and octadecanol. Above 15 mN m^{-1} the relationship shows as being fairly linear. Adapted from; Barnes and La Mer (1962) and La Mer & Aylmore (1961).

Alteration of air structure

Wind creates waves on storages, increasing the surface area and altering the air structure above the surface. The effect of monolayers in lowering wave amplitude, in turn may affect the wind structure, lowering the friction velocity U^* (see Equation 5.1) and decreasing evaporation as a result (Wu 1971). This is discussed in further detail in Chapter 5.

1.8.7 Effect of temperature

Evaporation resistances for hexadecanol and octadecanol have been measured by Barnes & La Mer (1962) and are shown in Figure 1.28. It can be seen that the evaporation resistance decreases with increasing temperature, nearly halving for a temperature rise of 10°C. This trend is quite different from figures of evaporation reduction on larger wind tunnels which suggest an evaporation reduction of 90% at a relatively high air temperature of 49 °C (Ghumman 1971)(see Section 5.2.1).

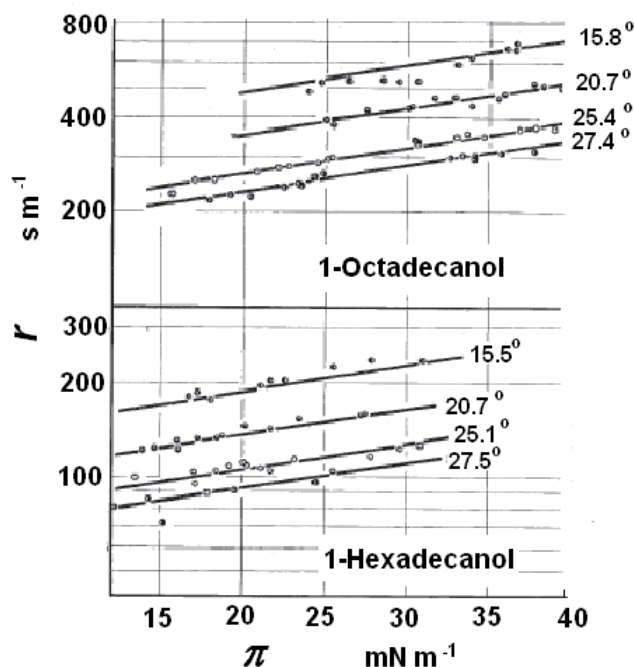


Figure 1.28 Effect of temperature on specific resistance r for the range of surface pressures π . Adapted from Barnes & La Mer (1962).

1.8.8 Compounds tested for evaporation reducing monolayers uses

Whilst the discussions thus far have been supported by data collected from a small range of candidate chemicals for monolayer, there is actually a wide range of potential candidates that possess the necessary combination of hydrophilic and hydrophobic ‘ends’. A compilation of exemplar molecules is provided in Table 1.2 along with some of their key properties including initial spreading speed, equilibrium surface pressure, evaporation resistance and an indication of their usage. This data has been sourced from Birdi (1934), Archer & La Mer (1955), Deo *et al.*(1961) and Weast (1974).

Table 1.2 Properties of chemicals that form monolayers

Chemical Name	Common Name	Melting point °C	Initial Spreading speed m s^{-1}	Equilibrium. surface pressure @25 C mN m^{-1}	Maximum evaporation resistance s m^{-1}	Evaporation reduction usage
---------------	-------------	---------------------	--	--	---	-----------------------------

Alcohols

1- Dodecanol	C12 alcohol	44	0.308			
1-Tetradecanol	C14 alcohol	39	0.265	46.5	42 @30 mN m^{-1}	
1-Pentadecanol	C15 alcohol	44		43		
1-Hexadecanol	C16 alcohol Cetyl	49	0.155	39.5	140 @30 mN m^{-1}	Used extensively Maximum pressure gained using spreading rate 20.7 g/hectare (Mansfield 1959).
1-Heptadecanol	C17 alcohol	54		41		
1-Octadecanol	C18 alcohol Stearyl	58	0.0085	35.2	390 @30 mN m^{-1}	Used extensively
1- Nonadecanol	C19 alcohol	62				
1-Eicosinol	C20 alcohol	71	0.0081	32.6		
1-Docosanol	C22 alcohol		0	27.6	1400 @30 mN m^{-1}	
cis-9-Octadecen-1-ol	Oleic alcohol	13-19			0	

Acids

Dodecanoic acid	C12 acid	44	0.295		-	
Tetradecanoic acid	C14 acid	58	0.135	15		
Hexadecanoic acid	C16 acid	63	22	9.7 *		
Heptadecanoic acid	C17 acid	62			140	

Octadecanoic acid	C18 acid Stearic acid	70	0	2 7.8*	230	
	Linoleic acid	5				
Nonadecanoic acid	C19 acid	66			390	
Eicosanoic acid	C20 acid Arachidic	75		5.4*	520	
Docosanoic acid	C22 Behenic acid			3.4*		
<i>cis</i> -9-Octadecenoic acid	Oleic Acid	14		31~	0 (Sebba & Briscoe 1940) Used for testing monolayer with no evaporation resistance	

Alkoxy Ethanols

n-Docosanoxy ethanol					1370 @30 mN m ⁻¹	
n-Tetradecanoxy-ethanol				48.6		
n-Hexadecanoxy ethanol				50.4	30 @30 mN m ⁻¹	
n-Octadecanoxy-ethanol				48.9	320 @30 mN m ⁻¹	
Ethyl octadecanoate					410 @30 mN m ⁻¹	
Cholesterol					10 @30 mN m ⁻¹	No effect on evaporation (Birdi 1934)

Calcium compounds

Calcium eicosanoate					1090 @30 mN m ⁻¹	
Calcium nonadecanoate					800 @30 mN m ⁻¹	
Calcium					560	

octadecanoate					@30 mN m ⁻¹
---------------	--	--	--	--	------------------------

* (Heikkila, Kwong, & Cornwell 1970)

~ (Rus 2003)

Table 1.3 Commercially available evaporation reducing, surface active layers

Product	Characteristics
<p>Aquatain liquid.</p> <p>Thought to be polydimethyl siloxane mixed with other hydrocarbons.</p> <p>Form: Liquid.</p>	<p>This is a commercial product, and therefore the exact ingredients are not given. By measurements of refractive index; 1.419 using five replicates, this is in the middle of the range for the polysiloxanes. However this is slightly different from polydimethyl siloxane. NMR tests show that ¾ of the proton signal matches a methyl group attached to silicon. So an educated guess would be polydimethyl siloxane (PDMS) with long carbon chain material added. However it was suspected that different purchases of the product contained different combinations.</p> <p>The density of a sample of Aquatrain purchased in a 20 litre drum was measured to be 903.5 kgm⁻³</p> <p>Application rate</p> <p>0.2 µm of thickness (2 litres/hectare) every 10 days (www.aquatrain.com 2008).</p>
<p>Water \$aver</p> <p>Hexadecanol mixed with lime particles to increase spreading</p> <p>Form: Powder</p>	<p>This product seems to use similar materials and preparation of the film as explained in the United States Patent 6303133 (O'brien 1998)</p> <p>A block of a mixture of hexadecanol and octadecanol is difficult to break apart into suitable sized particles in the field. Water\$aver overcomes this by mixing them with sodium hydroxide, which has the effect of producing a powder which has the capability of being stored without clumping with a particle size of less than 20 µm . When the sparingly soluble sodium hydroxide is ionized it produces positively charged small particles, which also enhance the spreading of the monolayer. The ratio of mixing is 1 part alcohol mixture to 5 parts sodium hydroxide for which inexpensive pre-powdered agricultural lime can be used.</p> <p>Application rate</p> <p>1 kg /hectare every 2.5 days (www.flexiblesolutions.com 2009).</p>

Si-ro-seal	C16 alcohol min 80%
Produced by CSIRO in 1956 for storages of up to 2 acres	C18 alcohol max 10% C12 and C14 alcohols max. 5% Lower alcohols max 0.5%
Form: Powder	Unsaturated alcohols max 4% Iodine value max 3%

The properties summarized in Table 1.2 are largely dependent on the shape of the molecule and how they pack in a solid lattice at maximum surface pressure where evaporation resistance is expected to be at its greatest. A good example of the impact of chain geometry is octadecanoic acid which possesses a straight carbon chain and *cis-9* octadecanoic acid which possesses a bent carbon chain. Octadecanoic acid packs into a neat lattice, while *cis-9* octadecanoic acid cannot pack neatly leaving holes, and therefore has little evaporation reducing ability.

1.8.9 Spreading Methods

There are two approaches to applying monolayers onto the surface of a water body; either in solid form (Tiblin, Florey, & Garstka 1962; Vines 1962) involving the application of pellets, flakes or powder, or as a liquid where the monolayer has been dissolved in a solvent (Dressler 1962; Roberts 1962).

Numerous methods of dispensing monolayers in pellet, flakes, powder and solution form were tested by Grundy (1962). Based on the measured evaporation reduction Grundy indicated discharging a solution from the upwind edge of the storage gave the best results. Tiblin *et al.* (1962) suggests the best method of application will for a given reservoir will be based on external factors including bank structure, weather condition (for example prevailing winds).

Recently there has been a trend towards liquid dispensing. Dissolved monolayers are easy to store in liquid form and the solvents have a much higher spreading rate. The solvent then volatilizes quickly, allowing the monolayer to assemble over the surface (Gericke, Simon-Kutscher, & Hühnerfuss 1993). A summary of some common solvents used to disperse monolayers is given in Table 1.4.

Table 1.4 Tested Solvents

Chemical	Effectiveness
n Hexanol	Produces an impervious monolayer in the lab (Gericke, Simon-Kutscher, & Hühnerfuss 1993).
Petroleum ether (Mix of low boiling	Retained in the monolayer leading to the formation of holes causing a decrease in evaporation resistance (Archer & La Mer 1955; La Mer & Robbins 1958; La Mer & Barnes 1959), decreasing the evaporation

point alkanes)	resistance at all pressures (La Mer, Healy, & Aylmore 1964).
Ethanol	May be included in monolayer; reducing the evaporation resistance (Gericke, Simon-Kutscher, & Hühnerfuss 1993)
Hexane	Often used as not retained in monolayer (Gericke, Simon-Kutscher, & Hühnerfuss 1993; La Mer, Healy, & Aylmore 1964).
Chloroform	Often used as not retained in monolayer(Gericke, Simon-Kutscher, & Hühnerfuss 1993).
Kerosene	Found to be effective in trials by Grundy (1962) in East Africa and McArthur(1962) in Scotland at 2% w/w. Retained at low pressures, though is effectively squeezed out of the monolayer at high pressures (La Mer, Healy, & Aylmore 1964)

1.8.10 Degradation of Monolayers

Assuming candidate monolayers exhibit the desirable attributes of evaporation resistance, spreading rates and low toxicity, there remains the issue of resilience. Monolayers, like any surface materials on a water body are subjected to an array of environmental factors that may ultimately degrade their performance.

Bacterial

Hexadecanol and octadecanol monolayers are susceptible to bacterial degradation. *Pseudomonas* and *Flavobacterium* have been shown to build up numbers and degrade hexadecanol with prolonged use under laboratory conditions (Chang, McClanahan, & Kabler 1962). They also acquire field samples from the surface after sustained application of 0.3 kg of hexadecanol day⁻¹ and measured an increase in *Pseudomonas*, *Alcaligenes* and *Aerobacter* populations from virtually none to a value in the order of millions ml⁻¹. Laboratory tests conducted on small troughs show this concentration is capable of reducing the lifetime of the monolayer (measured by a reduction in surface tension) from 1-2 days to several hours. High populations of these bacteria affected the spreading rate from crystals, as the crystals were surrounded by feeding bacteria. Chang *et al.* photographed *Pseudomonas* surrounding and feeding on rice grain-size crystals of hexadecanol impairing the spreading rate.

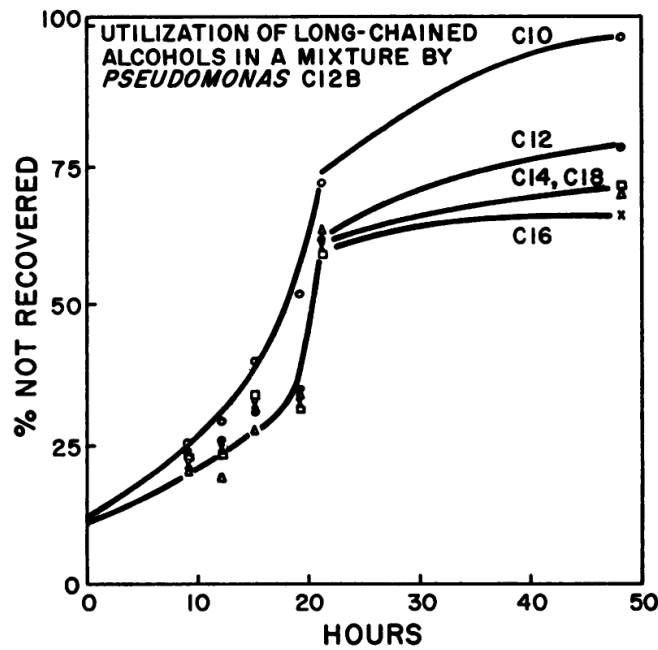


Figure 1.29 Utilization of alcohol monolayers by a culture of *Pseudomonas C12B*. Source; (Williams 1966).

Williams *et al.* (1966) investigated the degradation of C₁₀–C₁₈ primary alcohols by a strain of *Pseudomonas* called C12B (Figure 1.29), finding that all these monolayers were utilized, degrading their effectiveness in reducing evaporation. It was noticed that the number of bacteria increased rapidly on water covered with the alcohols. After a period of adaptation, the bacteria could reduce the effectiveness of monolayers within 24 hours effecting the evaporation reducing properties.

In field trials, 3 months trial performed on Lake Hefner, Oklahoma has shown an increase in bacteria generally, though no adverse affect on water quality. The results showed an evaporation reduction of 9% under difficult conditions (Department of the Interior 1959).

Wind

Wind drifts the surface, including monolayer downwind affecting coverage and creates turbulent waves affecting the integrity of the coverage. The deleterious and advantageous effects of wind are discussed in detail in Chapter 5. Field trials by many researchers such as made by Tiblin *et al* (1962) in Australia and by McArthur (1962) in Scotland led them to conclude that of major importance is the influence of wind. Any dispensing and detection methods would therefore need to be designed to allow for, and take advantage of the effects of wind.

Volatilization/Emulsification

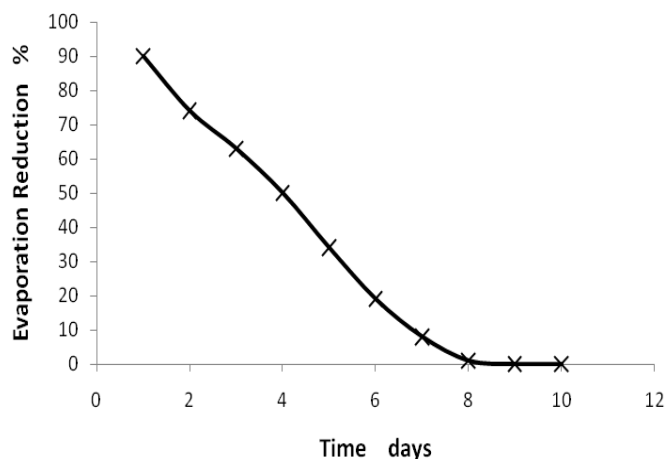


Figure 1.30 Evaporation reduction (%) of hexadecanol as a function of days following initial application. Temperature 49 °C with 1.1 m s⁻¹ wind speed. Adapted from Ghumman (1971).

The lifetime of applied monolayers on a water surface is also limited by volatilization, emulsification and dissolution. For pure hexadecanol volatilization is the most significant loss on large areas (Mansfield 1962), particularly as hexadecanol has a very small solubility of 0.08 ppm at 33 °C (Krause & Lange 1965). Warm temperatures and solar radiation increase the volatilization, decreasing the effective lifetime of the monolayer, as shown by the data gathered in Figure 1.30 by Ghumman (1971) for warm conditions of 49 °C.

Impurities

Pure samples of monolayer material are obtainable for study purposes, however cost effective larger quantities may suffer from several alcohols of varying chain length, as well as other impurities.

Chemical impurities often have a deleterious effect on the evaporation reducing capabilities of a candidate molecule. For example impurities trapped in a monolayer can result in “holes” being formed in the monolayer lattice, resulting in a lower evaporation resistance. La Mer & Barnes (1961) noted this impact and went so far as to say “It is possible that evaporation resistance itself as a measure of purity”. They explain that using dyes to ‘label’ monolayers, for example to be able to visualize their extent on a water body is a sensible development, however dye molecules can create holes in the lattice.

Once the monolayer has been dispensed it is vulnerable to impurities residing in the microlayer. This is a layer where the concentration of particles is considerably greater than that in the water immediately below, containing surface active impurities including organic matter and microbes (Wangersky 1976). Also natural impurities such as plant waxes may also be incorporated into monolayers once applied on a water body reducing the evaporation resistance. (Barnes & La Mer 1962; Craig *et al.* 2007).

1.9 Detecting the presence of monolayers: The scope of this thesis

Despite all the work carried out on monolayers for over 50 years, they are not in common use today. One of the main reasons seems to be the irreproducibility of results in field trials due to uncertainty in assessing coverage.

Large scale deployment of monolayers was completed in the 1960s, by Vines, Manson, Barnes, Jarvis and La Mer, who all meticulously explored the possibilities and obstacles to widespread use on evaporation reduction on water storages. Successful dispensing of large scale field trials in these experiments, however, was always labour intensive. It involved the use of a boat (Vines 1962), or switching on dispensers mounted on the upwind bank (Grundy 1962). Monitoring of the coverage required was manually assessed by observing wave damping (McArthur 1962) or using indicator oils (Adam 1937). The labour costs involved in following these dispensing and monitoring procedures add significantly to the cost/ML saved and have impeded the use of monolayers. So an automatic monitoring and dispensing system is long overdue, both to reduce observation and dispensing costs and to respond quickly to changes in weather conditions to optimize evaporation reduction by ensuring maximum coverage.

The cost per ML saved is not markedly different between the main commercial evaporation reducing products (Craig *et al.* 2005) ranging from \$250-400 per ML; while the average cost per ML for purchasing water in the Murray-Darling basin for the year 09/10 is \$1000 per ML (GDH Hassall 2010), around twice the cost. The cost per ML saved for monolayer techniques would be improved greatly by ensuring maximum coverage and reducing labour costs by utilizing an automated detection/dispensing deployment of monolayer.

The coverage of evaporation reducing layers is largely dependent on the effects of wind, volatilization, and biological degradation. A relatively low wind speed may completely uncover large water storages in a matter of hours. The advice given by manufacturers of the surface active layers, “Aquatain” and AquaSaver is to apply a standard amount at a standard interval. This blind approach might work quite well in swimming pools, where an overestimation of the required amount has minimal costs and spreading characteristics still result in complete coverage. However on larger surfaces the larger amount of product means dispensing needs to be more accurate, and spatial dosing and monitoring becomes more important as the surface moves in response to wind and waves.

In the preceding sections, we have already seen that, despite monolayers forming an extremely thin surface active layer, they have the ability to reduce evaporation. In addition, they also, reduce surface tension, increase viscosity and alter the temperature flux resulting in an altered water temperature profile. These changes make convenient bases to test for potential diagnostic indication of monolayer in categories of; the retardation to surface motion (reduction in surface tension and an increase surface viscosity), water temperature profile changes (contact), alteration to interactions with electromagnetic radiations (emissivity, spectral absorption and remote surface temperature), and effects of wind.

In the following chapters, this thesis will introduce the underlying physics behind each of these categories representing changes occurring to and around the surface that occur with the addition of monolayer and provide some preliminary experimental measurements to indicate the realistic potential of each technique as a means of detecting the presence/absence of monolayers. The most

promising candidate will be identified and the remaining chapters will focus on the design, construction, calibration and preliminary testing of a practical sensor.

Detection techniques that already have been developed under laboratory conditions have been scrutinized for suitability and reliability under the more adverse field conditions. New methods will have been investigated on the laboratory scale and extended to field use if found promising.

So the challenge for this work is the development of a sensor that automatically tests the surface, for monolayer coverage, so that this information can be used as a feedback loop for a dispensing system. Dosing can then be carried out according to the existing state of the surface and other relevant environmental conditions. Both the economical use of monolayer material, a reduction of labour costs and assured best coverage decrease the ongoing costs of monolayer would make it a more viable option for conserving water.

In regard to an investigation into a reliable indicator that can be used on open water storages, the chapters contain the following material:

Chapter 2 examines the changes to surface tension and viscosity created by monolayers and attempts to find reliable indicators of monolayer presence using a horizontal surface tension float, and by measuring the increased decay of artificial waves. The temperature profile is examined in Chapter 3 showing that monolayers do have some effect on the temperature changes that occur at the surface, relative to deeper levels. Measurements were made to determine whether monolayers alter the reflection or absorption of light in Chapter 4 with the interesting result that although IR (InfraRed) thermometers are not effective at detecting the increase in temperature on a large surface, on a small sampling surface, under windy conditions, definite differences were evident. The effects of wind are measured in Chapter 5 showing the surprising result that evaporation differences are amplified with the use of an artificial wind produced by a small fan. Chapter 6 consists of piecing together the evidence of earlier chapters to build a wind assisted surface temperature monitoring device (WASP) which can potentially discern the presence of monolayer by the alteration in evaporation. The final chapter (7) outlines key achievements, outcomes and some ideas on how future monolayer systems may benefit from this work.

Chapter 2. Surface Tension and Surface Waves: Detection Techniques

The most often quoted indication of monolayer coverage on storages is the reduction in wave amplitude leading to clearly defined smooth patches on a partially-covered storage. Monolayers affect the surface by lowering surface tension (see π -A isotherms, Section 1.5.2), and increasing the surface viscosity (Goodrich 1962); both acting to decrease wave amplitude (Behroozi *et al.* 2007). Wave speed is also affected by the reduction in surface tension (Brown 2005:55). These surface changes caused by monolayers are examined in this chapter with a view to identifying reliable measurable changes that may facilitate automated detection. A manual detection method based on surface tension already has been developed using indicator oils (Barnes & Gentle 2005) and a summary of this method is also presented.

2.1 Horizontal and vertical force transducers for directly measuring surface tension

The reduction in surface tension of water is an indication of the presence of a surfactant such as a monolayer (Hühnerfuss, Walter, & Kruspe 1977) as shown by the success in using indicator oils (Section 2.2) for detection.

It is not uncommon, however, for water bodies to have a surface tension lower than that for pure water. Surfactants from either biological or anthropogenic causes may reduce the pure water surface tension. Surface pressures of 3-12 mN m⁻¹ for biogenic oil slicks were measured by Garrett (1965) at sea on Chesapeake Bay. On rivers water bodies and puddles around England, Goldacre (1949) measured surface pressures varying from 0-30 mN m⁻¹. He noted that the lowest surface pressures were found in rivers and streams where moving water would clear the surface to a greater degree, and the highest in stagnant ponds and lakes. Therefore water storages, which tend to contain still water would tend to naturally possess a higher surface pressure (lower surface tension), making surface tension detection methods more difficult.

Surface tension is used to characterize monolayers often using Langmuir troughs, as described in Section 1.8.1. These measurements are taken under controlled still surface conditions where surface tension is monitored using the vertical Wilhelmy plate. Unfortunately the Wilhelmy plate method will not work with any surface turbulence present, as it uses an extremely sensitive computer controlled transducer to obtain surface tension values from the vertical weight of the suspended plate. Even with the use of a stilling well under field conditions to combat waves, vertical measurements like the Wilhelmy plate and similar laboratory methods would be difficult as they have a very limited range of movement and need to be zeroed for a specific water height. Therefore these measurements are unmanageable in determining surface tension in the field.

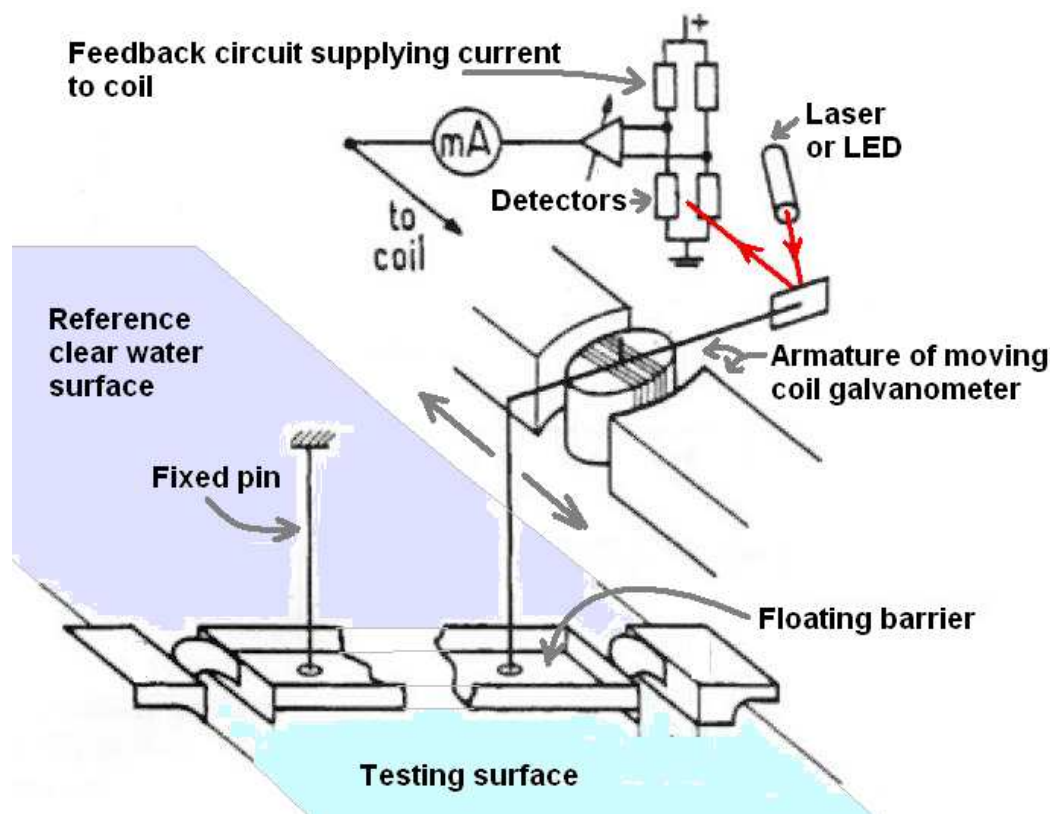


Figure 2.1 Horizontal surface tension transducer. Adapted from Perez & Wolfe (1994).

Surface tension can also be measured horizontally using floating barriers. This has been successfully performed under laboratory conditions by Perez & Wolf (1994), who monitored the force on a barrier separating a reference water surface from the testing surface. They constructed the mechanism by removing the casing on a disused quality moving coil ammeter, and positioning it, so that the end of the indicator needle could be attached to one end of the barrier as shown in Figure 2.1. One side of the barrier was a reference clear water surface, and the other a testing surface. Differences in surface tension between the two surfaces apply a force to the barrier which will move the needle. Changes to the needle angle alters the angle of a mirror attached to the other end of the needle altering the direction of the reflected beam which is normally incident on a region between two photo resistors (labelled detectors). Light on either resistor activates a feedback circuit which alters the current in the ammeter forcing the needle back to the original position. So the mechanism is a transducer, where the current in the coils of the armature are measured as an indication of force on the needle.

The amount of current required is calibrated to the surface tension differences between the two sections of water, and this in turn is calibrated to the amount of monolayer present. Perez & Wolf found in measuring surface tension the device has a precision of 0.5% under ideal conditions when properly calibrated.

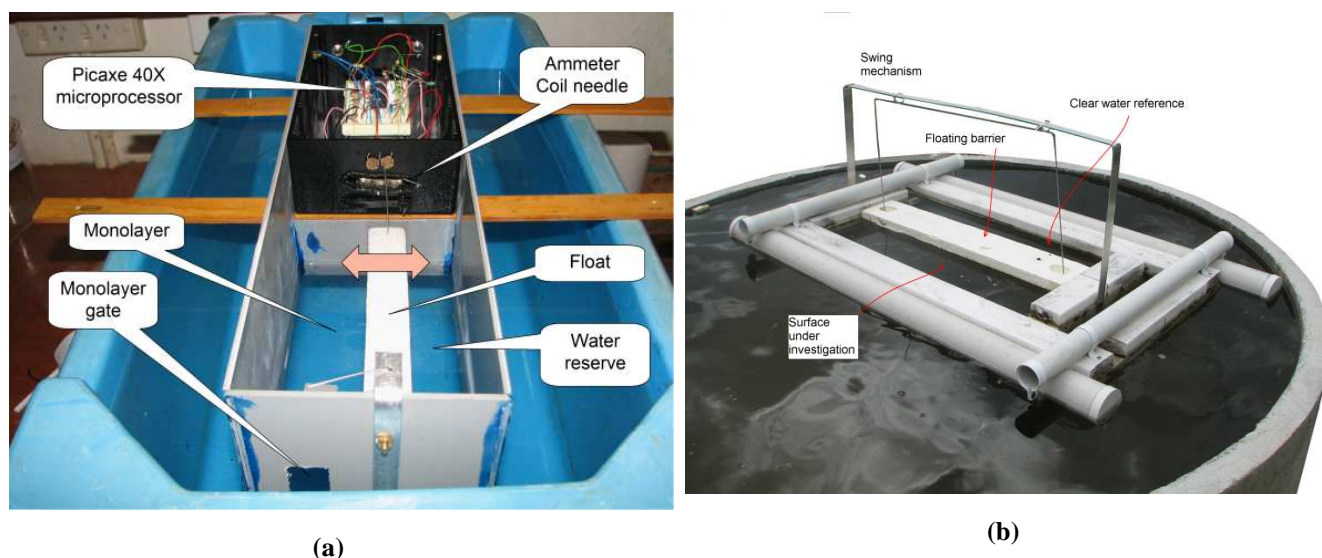


Figure 2.2 Devices constructed to monitor surface pressure by measuring the force on a barrier between a reference clear water sample and the tested surface. (a) Has a floating polystyrene barrier 18 cm in length, while in (b) the barrier has been enlarged to 1.0 m to provide a larger force.

In this current project several mechanisms (Figure 2.2) were constructed to attempt to gain similar results. A working model similar to the Perez-Wolf mechanism was constructed with a barrier of length 18 cm (Figure 2.2(a)) but several obstacles were found in its application to field conditions. The main ones were motion of the barrier arising from motion of the whole device and waves entering the access gate. There was also difficulty in finding an appropriate material which would fill the gaps at both ends of the barrier, float, and be flexible enough not to impede the free movement of the barrier. For this size barrier, the maximum difference in horizontal force would be 7 mN m^{-1} which was found to be too small to be measured even in moderately rough surface conditions. To increase the force on the barrier, larger models were constructed using a 1.0 m swinging barrier as pictured in Figure 2.2(b). This provided a larger force, and was easily measured under still conditions indoors. However when the model was floated in a larger trough outdoors, wind affected the floating barrier swing system badly. It also proved difficult to keep the reference water free from contamination from monolayer. Furthermore it was found that floating debris such as leaves tended to accumulate in the sampling area obstructing the free movement of the barrier. When these obstacles were combined with the observations above that the surface tension of water storages is often below the value for pure water (Goldacre 1949)(B. Albrecht Pers. Comm. 2009), it was considered monitoring surface tension horizontally presented too many obstacles to be useful in the field and was not pursued any further.

2.2 Indicator oils

Another method for determining the surface tension of water, and hence the presence of a monolayer involves the use of indicator oils. The test consists of placing an oil droplet carefully on top of a selected water surface with an eye dropper and observing the spreading behaviour. The spreading behaviour depends on the difference between the contracting forces around the oil drop

and the expanding force of the surface of the liquid (the subphase). Spreading will occur when the sub phase surface tension (γ_{as}) exceeds the sum of the surface tensions of the air/indicator oil (γ_{ao}) and the oil/subphase (γ_{os}) according to Barnes & Gentle (2005):

$$\gamma_{as} \geq \gamma_{ao} + \gamma_{os} \quad (2.1)$$

The value of subphase surface tension (γ_{os}) beneath the oil can be inferred by observing the spreading behaviour using a range of oils whose surface tension is known. Thus, the surface pressure of any *in situ* film can be estimated. A range of indicator oils that have been used for this purpose are listed in Table 2.1

Table 2.1 List of some reported indicator oil sets

Authors	Product	Comments made																		
Adam (1937) claims a precision of 1 mN m^{-1} using sea water.	Ratio of white oil from Shell-Mex (approximately 87 % of higher paraffins and 13 % of naphthenes) and dodecanol. Calibration was performed on sea water. The surface pressures for distilled water were thought to be 7% lower, however it was uncertain whether this was outside the inaccuracy of the experiment.	Ratios suggested by Adam																		
		<table border="1"> <tr> <td>% of dodecanol</td> <td>Surface pressure against which slow spreading occurs mN m^{-1} for sea water</td> </tr> <tr> <td>0.05</td> <td>Very slow spreading even on clean water</td> </tr> <tr> <td>0.07</td> <td>1</td> </tr> <tr> <td>0.1</td> <td>3</td> </tr> <tr> <td>0.2</td> <td>6</td> </tr> <tr> <td>0.3</td> <td>12</td> </tr> <tr> <td>0.5</td> <td>16</td> </tr> <tr> <td>0.7</td> <td>19</td> </tr> <tr> <td>1.0</td> <td>22</td> </tr> </table>	% of dodecanol	Surface pressure against which slow spreading occurs mN m^{-1} for sea water	0.05	Very slow spreading even on clean water	0.07	1	0.1	3	0.2	6	0.3	12	0.5	16	0.7	19	1.0	22
		% of dodecanol	Surface pressure against which slow spreading occurs mN m^{-1} for sea water																	
		0.05	Very slow spreading even on clean water																	
		0.07	1																	
		0.1	3																	
		0.2	6																	
		0.3	12																	
		0.5	16																	
0.7	19																			
1.0	22																			
Langmuir and Schaeffer (1939)	Various types of oils including a mixture of petroleum jelly and motor oil	Both expansion of oil and colour was used as an indicator																		
(Goldacre 1949)	Tricresylphosphate Castor oil Oleic acid	The expansion of the oil was indicated by the movement of particles of dust resting on the film.																		

Timblin <i>et al</i> (1962)	Dodecanol in a light mineral oil	The film surface pressure could be ascertained to within 5 mNm ⁻¹
(Hühnerfuss, Walter, & Kruspe 1977)	1-Dodecanol with nonspreading paraffin oil.	The ratio found by Zisman (1941), as quoted by Garrett & Barger(1970) is 0.2, 0.5, and 1.0% dodecanol-1 dissolved in paraffin oil giving spreading pressure values of 3.0, 11.0 and 17.5 mN m ⁻¹ respectively (Zisman, 1941).
McArthur (1962)	Oleic Acid (tests for 32mNm ⁻¹) Castor oil (tests for 17 mN m ⁻¹) 15% solution of ethyl myristate in liquid paraffin (tests for 7 mN m ⁻¹)	
Barnes and Gentle (2005)	Benzene (72.6 mN m ⁻¹), Aniline (48.8 mN m ⁻¹), Oleic Acid (48.1 mN m ⁻¹) Octanol (36 mN m ⁻¹)	Oleic acid and octanol were most useful. Benzene tests for a high surface tension and Aniline partially drops through the surface.

Over many years there has been widespread use of indicator oils in testing for the presence of surface active layers. The initial surface tension needs to be ascertained before using the indicator oils to detect surface pressure (Adam 1937). For a clear surface with no monolayer $\pi = 0$, and with full pressure coverage $\pi = 40 \text{ mN m}^{-1}$ for hexadecanol, however these are relative to the initial clear water surface tension. For instance if an irrigation channel is being tested for monolayer, and the surface tension was already halved by impurities, the indicator oil would never spread, and therefore not show any surface pressure. This was noticed by Bruce Albrecht (Pers. Comm. 2009), who tried to test irrigation channels, and found that oleic acid (surface tension 48 mNm^{-1}) would not spread on a clear surface due to a low surface tension created by impurities. This is in contrast to testing carried out in this work on small local farm dams which showed good initial spreading for oleic acid.

Surface tension of tap water and distilled water (on tap in the Stokes building, University of New England) was checked with the indicator oil oleic acid. The drop spread in tap water, indicating tap water had a surface tension above 48 mN m^{-1} , while the distilled water performed badly with a surface tension below this value. For this reason only tap water was used for all experiments, as it better represents water from a storage.

The use of indicator oil is an efficient manual way of determining the presence of monolayer if calibration tests are carried out to check the initial surface tension, suitable indicator oils can then

be chosen. There are also possibilities for portable kits to be used by water storage owners, to test coverage on small storages. On larger storages, this would probably be too labour intensive to test various points around the surface. The scope of this work is to focus on automatic testing, and despite the low cost and ease of measurement there seems little chance of automating this method of testing.

2.3 Surface waves



Figure 2.3 Appearance of a spreading hexadecanol mixture (WaterSaver™) under light winds (Craig *et al.* 2007).

The nature of waves that propagate along the surface of a water body is as much a reflection of the physical characteristics of the water itself as it is of external conditions such as wind speed. The difference in waves created by a hexadecanol (WaterSaver™) is displayed in Figure 2.3. Consequently, it is feasible that characteristics of surface waves can be used as an indicator of the physical characteristics of water body. The following section first examines the underlying physics of surface waves, and discusses possible avenues for detecting/quantifying the presence of monolayers using surface wave characteristics. One of the most promising characteristics is selected and an experiment designed, conducted and results presented.

2.3.1 Nomenclature used

For the following discussion the reference frame origin is placed on the water surface with Cartesian axes as shown in Figure 2.4

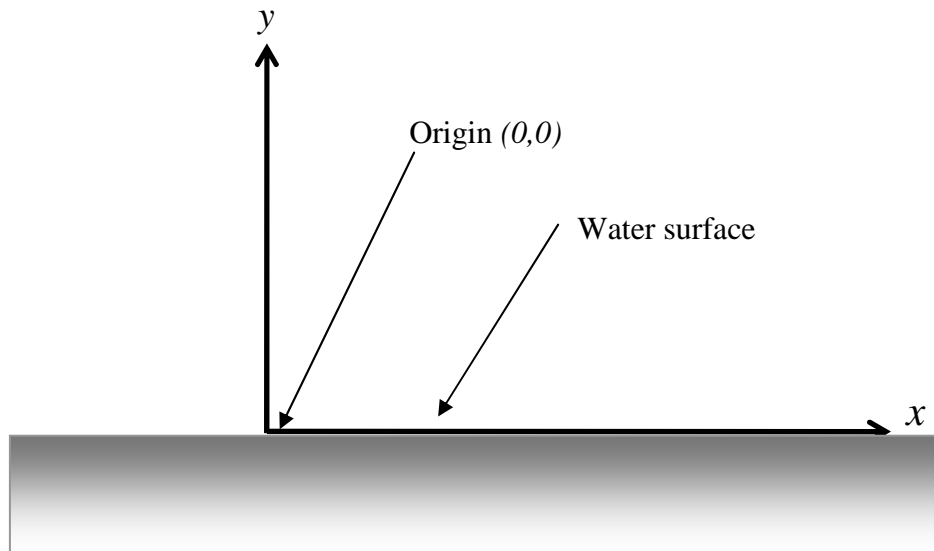


Figure 2.4 Position of axis with respect to water surface.

Table 2.2 Fluid dynamics terms

<i>Symbol</i>	Quantity	Units
λ	Wavelength	m
f	Frequency	Hz
T	Period	s
$\omega = 2\pi f$	Phase speed	rad s ⁻¹
$k = \frac{2\pi}{\lambda}$	Wave number	m ⁻¹
h	Vertical distance from surface. Height if positive, depth if negative.	m
v	Wave velocity	m s ⁻¹
v_g	Group velocity	m s ⁻¹
A	Amplitude = maximum distance from equilibrium point $y = 0$.	
γ	Surface tension – an unequal force of cohesion drawing surface molecules into the bulk liquid. It can be measured as the magnitude of a force acting normal to the interface per unit length of the film at equilibrium, or the surface energy: the energy required to increase the surface area of the liquid by a unit amount.	N m ⁻¹ or J m ⁻² .

η	viscosity measures a fluids resistance to flow. It is defined as η in $F = \frac{\eta}{A} \frac{dv}{dy}$	Pa s
g	acceleration due to gravity	m s^{-2}
ρ	density	kg m^{-3}
Φ	velocity potential is defined so that the derivative is the velocity $\nabla\Phi = v$	$\text{m}^2 \text{sec}^{-1}$
Ψ	stream function is a constant along steam lines. Stream-lines are curves such that no fluid crosses.	$\text{m}^2 \text{sec}^{-1}$

2.3.2 Wave velocity

There are two types of waves that propagate along water surface which are categorized according to the main restoring force. Gravity waves are large waves, such as ocean waves, where the amplitude is of the order of metres and the reaction force acting to return the surface to equilibrium is gravity ($\lambda > 2.3 \text{ cm}, f < 13 \text{ Hz}$). Capillary waves are small ripples where the main restoring force is surface tension ($\lambda < 2.3 \text{ cm}, f > 13 \text{ Hz}$). This demarcation point between these two types of waves will be found later in Section 2.3.6.

2.3.3 Gravity waves- Static method

One method for deriving the wave velocity equates the maximum falling velocity of the water surface with the velocity on a crest (Oertel 2004).

If we assume the liquid has no viscosity, or is inviscid, then one dimensional flow along a stream tube can be described by Bernoulli's equation;

$$p + \rho gh + \frac{1}{2}\rho v^2 = \text{constant} \quad (2.2)$$

where p is pressure, ρ is density, g is the acceleration due to gravity, h is the height of the fluid and v is the velocity. The term ρgh describes changes to pressure due to height, and the term $\frac{1}{2}\rho v^2$ describes changes in pressure caused by velocity.

Dividing by ρg gives

$$\frac{p}{\rho g} + h + \frac{v^2}{2g} = \text{constant} \quad (2.3)$$

The term $\frac{p}{\rho g}$ is the height of the wave above equilibrium position $y = 0$ that generates the pressure p by its weight, and is therefore called pressure height .

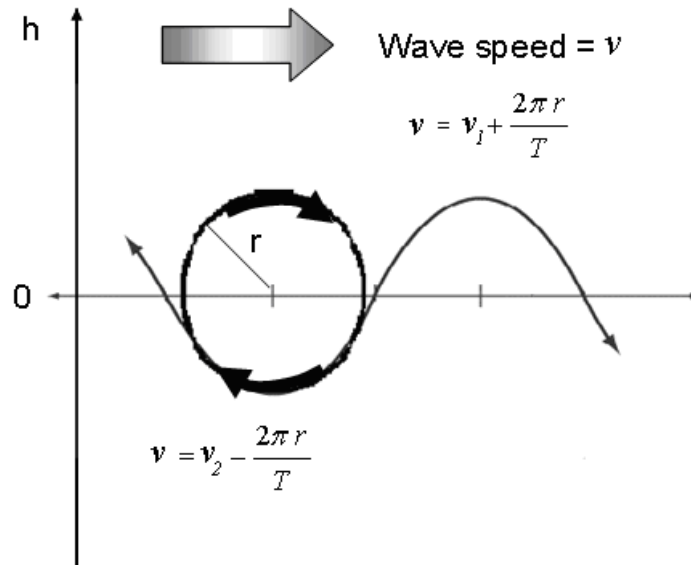


Figure 2.5 Comparison of streamline velocities v at crest and trough positions.

The term $\frac{v^2}{2g}$ is the height that a body would have to fall to achieve a velocity of v by free fall. A circular path of a particle lying on the surface is defined by a radius r , with a period of revolution T . The velocity of the circle is then $\frac{2\pi r}{T}$.

If the wave velocity is v , the flow velocity on the crest of the wave; $v_1 = v + \frac{2\pi r}{T}$, and that in the trough is $v_2 = v - \frac{2\pi r}{T}$ as depicted in Figure 2.5.. Because the pressures are equal, the term $\frac{p}{\rho g}$ remains constant.

Bernoulli's equation comparing a crest with a trough reduces to:

$$v_2^2 - v_1^2 = 4gh = 4gr \quad (2.4)$$

Expanding v_1 and v_2 , the left side is equal to $\frac{8\pi v}{T}$. Rearranging this for v gives:

$$v = \frac{gT}{2\pi} \quad (2.5)$$

As the radius term cancels out, the wave velocity is independent of the height of the wave.

Substituting $T = \frac{\lambda}{v}$ to eliminate T gives:

$$v = \sqrt{\frac{g}{k}} \quad (2.6)$$

This relationship holds for inviscid waves and is a good approximation for water. It has been derived assuming the only restoring force is in the vertical direction and is gravity.

2.3.4 Capillary waves- Dynamic method

Gravity acts over all wavelengths, however at small wavelengths surface tension is most effective, acting like a stretched membrane and reducing surface area (Kenyon 1998). This result in a restoring force lowering crests and raising troughs, which increases with decreasing wavelength.

If the effects of gravity are ignored, the wave velocity term for capillary waves can be derived as follows:

The static solution of Laplace's equation for pressure just below the surface of waves of very small amplitude (small kA value), where the radius of curvature of the crests is the same for crests and troughs due to surface tension is (Kenyon 1998):

$$\Delta p_1 = \frac{2\gamma}{R} \quad (2.7)$$

where Δp_1 is the difference between the static pressure at the crest and the static pressure at the trough and R is the principle radius of curvature of the surface. Within the surface of the water, the pressure is greatest in the concave trough and lowest in the crest.

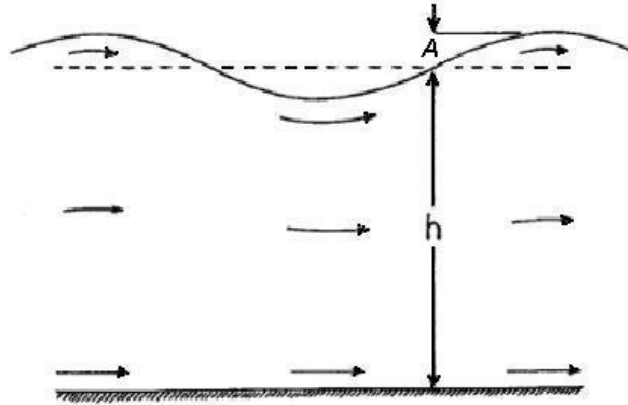


Figure 2.6 The steady frame of reference employed by Einstein (1916), in which the wave is static and the water is moving to the right. Using this frame the maintenance of the wave is provided by a balance between static pressure and dynamic pressure along a surface streamline. Adapted from Kenyon (1998).

If the surface tension is ignored, and the static conditions are now changed to a dynamic moving wave, then a frame of reference that follows the wave shape is used (Einstein 1916; Kenyon 1998). In this ‘steady’ frame of reference the wave appears still and the fluid moves in the opposite direction. This would mean that if the fluid is moving from left to right as drawn in Figure 2.6. This means that the wave is moving from right to left with respect to the fluid. It is then easy to equate the static pressures with the opposing dynamic pressures along the surface streamline. If a surface wave with small amplitude is considered, the flow speed is faster in the troughs than the average fluid speed, and at the crests it is slower, due to the natural circular motion of the wave (Figure 2.6).

The Bernoulli principle states that for inviscid and incompressible fluids, the speed of streamlines can be related to the pressure according to:

$$p = \text{constant} - \frac{1}{2} \rho v^2 \quad (2.8)$$

where the constant remains the same for each streamline.

The faster the streamline flows, the lower the pressure at that point in the streamline. The lower velocity in the wave crest, compared to the trough, increases the pressure at the crest. The Bernoulli variation in pressure tends to increase the height of the crest and lower the height of the trough, and the amplitude of the wave increases.

The dynamic pressure difference is then:

$$\Delta p_2 = \frac{1}{2} \rho \left(v + \frac{\Delta v}{2} \right)^2 - \frac{1}{2} \rho \left(v - \frac{\Delta v}{2} \right)^2 = \rho v \Delta v \quad (2.9)$$

where $\Delta v/2$ is the variation in fluid speed caused by the wave. The variation is assumed to be the same at crest and trough which is reasonable for very small kA .

The pressure difference between crest and trough caused by surface tension is opposite in sign to the dynamic pressure difference. Therefore:

$$\Delta p_1 = \Delta p_2 = \frac{2\gamma}{R} = \rho v \Delta v \quad (2.10)$$

In order to evaluate this equation, the variation in velocity Δv needs to be expressed in terms of conservation of mass between the crests and troughs of the wave.

$$\left(v + \frac{\Delta v}{2}\right)(h - A) = \left(v - \frac{\Delta v}{2}\right)(h + A) \quad (2.11)$$

where h is the depth of influence of the wave. The effect of the wave diminishes with depth, however this does not affect the result (Kenyan 1983).

This leaves:

$$2vA = \Delta v h \quad (2.12)$$

Influence depth has also been calculated by Kenyon (1998) as

$$h = \frac{1}{k} \quad (2.13)$$

This derivation shows that the depth of influence of the wave is proportional to the wavelength, though independent of surface tension and amplitude of the wave.

By substituting Equation 2.10 into Equation 2.12 to remove Δv , then Equation 2.13 to remove h , Equation 2.11 reduces to:

$$v^2 = \frac{\gamma}{\rho R k A} \quad (2.14)$$

A formula commonly used to calculate radius of curvature for small amplitudes (Burington 1948) is:

$$R = \left[\frac{\partial^2 y}{\partial k^2} \right]^{-1} \quad (2.15).$$

If a sinusoidal shape is assumed, then:

$$y = A \sin kx \quad \text{and} \quad R = \frac{1}{k^2 A} \quad (2.16)$$

Substituting these into Equation 2.14 results in:

$$v^2 = \frac{\gamma k}{\rho} \quad (2.17)$$

This velocity of fluid in the steady frame of reference is also the wave velocity in a fixed frame of reference. This is the wave velocity due to surface tension term, derived by equating the static and dynamic forces.

Adding the already derived gravity term (Equation 2.6) yields, the Kelvin's dispersion equation:

$$v^2 = \frac{\gamma k}{\rho} + \frac{g}{k} \quad (2.18)$$

This relationship predicts the velocity of a surface wave based on the restoring forces of both gravity and surface tension. The values of each of these terms as a function of wavelength is shown in Figure 2.7.

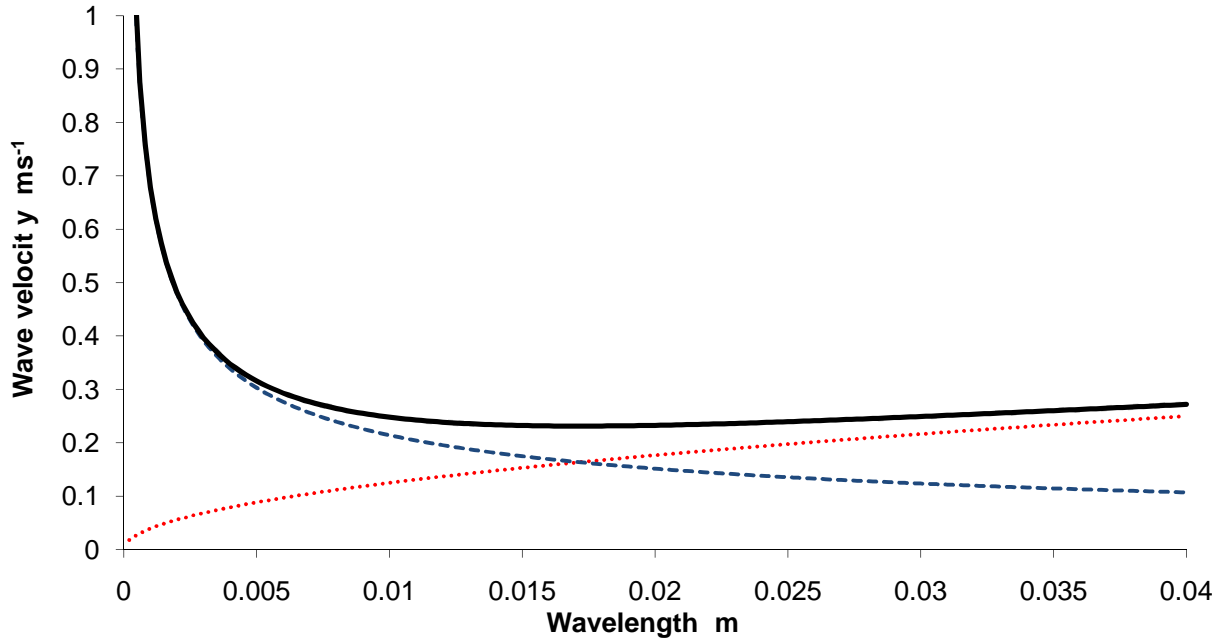


Figure 2.7 Both capillary (red dotted line) and gravity (blue dashed line) values adding to give the total wave velocity as described in Kelvin's dispersion equation (Equation 2.18).

2.3.5 Effect of depth on wave velocity

The effect of water depth on wave velocity is an important consideration if wave speed is going to be used as the basis of detecting alterations in the nature of the water surface. The dispersion equation of Equation 2.18 assumes there are no 'bottom' effects. If a shallow trough is used, the influence of the depth as a function of wavelength was derived by Lamb (1932:364) by applying the continuity equation $\nabla \cdot v = 0$. Integrating and assuming irrotational forces acting gives Laplace's equation which can be used to describe the surface wave action. If ϕ is defined as the velocity potential the continuity equation is written:

$$\frac{\partial^2 \phi}{\partial x^2} + \frac{\partial^2 \phi}{\partial y^2} = 0 \quad (2.19)$$

with the condition that $\frac{\partial \phi}{\partial n} = 0$ at a fixed boundary where n is a vector normal to the boundary.

It can be shown that waves exhibiting simple harmonic motion, with the time factor being $e^{i(\omega t + \epsilon)}$ have a velocity potential given by:

$$\omega^2 \phi = g \frac{\partial \phi}{\partial y} \quad (2.20)$$

where ω is the phase velocity ($\omega = ck$), which has the solution:

$$\omega^2 = gk \tanh kh \quad \text{or} \quad c^2 = \frac{g}{k} \tanh kh \quad (2.21)$$

This term can be incorporated into Kelvin's dispersion equation to including the effects of depth:

$$v^2 = \left(\frac{\gamma k}{\rho} + \frac{g}{k} \right) \tanh kh \quad (2.22)$$

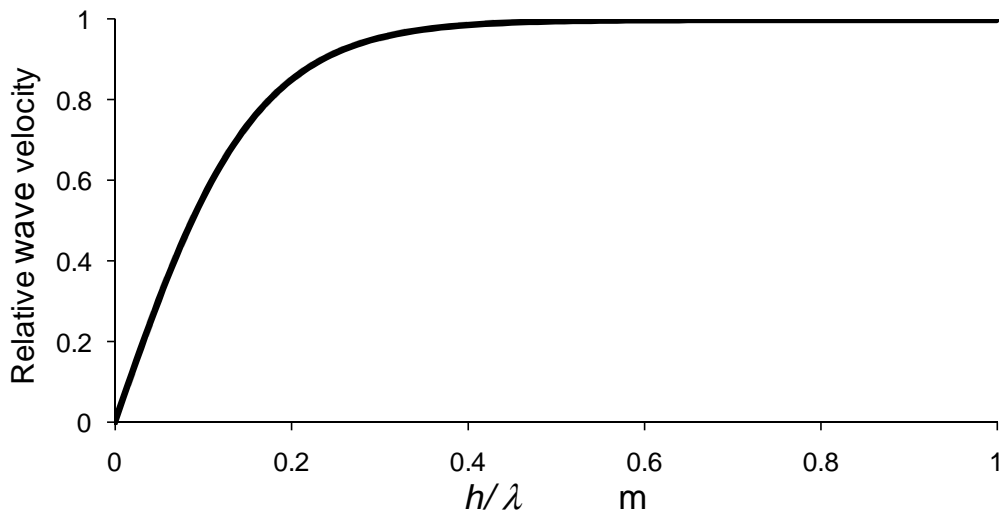


Figure 2.8 Theoretical relative wave velocity expressed as a ratio of depth h and wavelength λ using Equation 2.21.

Observation of Figure 2.8 shows that the attenuation of wave velocity only occurs for depths smaller than $\frac{1}{2} \lambda$. For capillary waves a reduction in velocity only occurs with depths shallower than several cm. For larger gravity waves, depth effects are easily observed in ocean waves as they approach shore with the characteristic rising of the wave tops. Here the wave fronts slow down, decreasing the wavelength and compacting the wave horizontally, resulting in an increase in amplitude and a sharper peak. It is also responsible for refracting ocean waves so the wave front becomes more parallel to the beach.

2.3.6 Minimum wave velocity

Kelvin's dispersion relation (Equation 2.18) combines the velocity of gravity waves, which increases with increasing wavelength, with the velocity of capillary waves, which decreases. There is a velocity minimum between these two restoring forces which can be found by determining k corresponding to the stationary point (Filippov (2000:120)

$$\frac{\partial v^2}{\partial k} = 0 \Rightarrow -\frac{g}{k^2} + \frac{\gamma}{\rho} = 0 \Rightarrow k_{\min} = \sqrt{\frac{g\rho}{\gamma}} \quad (2.23)$$

The corresponding wave velocity, v_w can now be calculated by substituting into the dispersion equation (Equation 2.19)

$$v_w^2 = \sqrt{\frac{g}{k} + \frac{\gamma k}{\rho}} = 2\sqrt{\frac{\gamma g}{\rho}} \quad (2.24)$$

In the case of a clear water interface at 20 °C: $\gamma = 0.073 \text{ Nm}^{-1}$, $\rho = 1000 \text{ kg m}^{-3}$ and $g = 9.8 \text{ m s}^{-2}$ the calculated wave velocity is $v = 0.231 \text{ m s}^{-1}$ and the calculated wavelength is 1.71 cm. The corresponding frequency which this occurs is 13.5 Hz.

A decrease in wave speed is predicted by Kelvin's equation (2.18) with addition of monolayers to the surface due to the lowering surface tension altering the capillary term. The difference in wave speed between clear water and monolayer would also be expected to increase with increasing frequency, as the wavelength decreases.

2.4 Experimental determination of wave velocity in the presence of a monolayer

2.4.1 Generation and observation of capillary waves

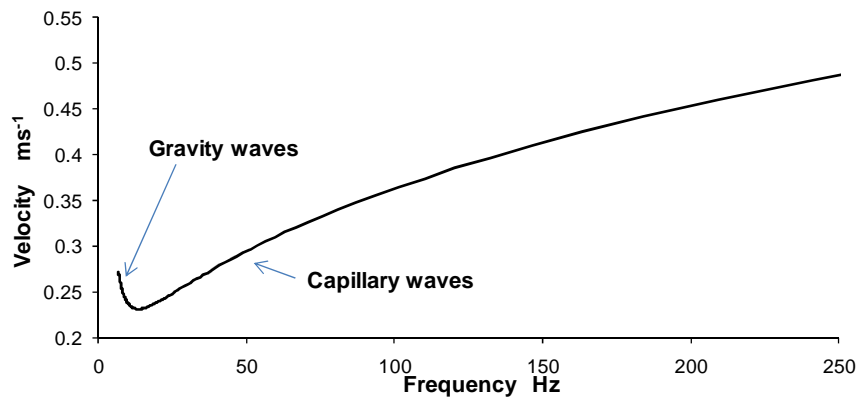


Figure 2.9 Theoretical wave velocity for water, calculated using Kelvin's dispersion equation.

The use of moving air to generate waves results in waves of variable (and unpredictable) structure, generally limited to wavelengths corresponding to gravity waves, shown on the left side of the velocity minimum in Figure 2.9. Furthermore wind cannot reinforce capillary waves, since the velocity is decreasing with increasing wavelength (decreasing frequency), shown on the right side of the minimum (Gottifredi & Jameson 1968). Clearly this approach is unsuited to the generation of capillary waves.

Higher frequency surface waves can be generated in the range of 1-600 Hz using a mechanical device, such as a paddle attached to an acoustic speaker Behroozi & Behroozi (2006).

Waves with frequency higher than 600 Hz are often excited using an electrocapillary blade. This consists of a thin blade positioned just above the water surface, to which a few hundred volts AC is applied between the blade and the underlying fluid (Miller 2003) this produces waves of amplitude around 0.5–5 μm (Behroozi *et al.* 2007).

A possible method for measuring the decrease in velocity caused by monolayers would be to produce a single pulse, and measure the time taken to traverse a set distance. This transference of energy would however, result in measurement of the group velocity (Lighthill 2005:240) where $v_g = \frac{3v}{2}$ (See Appendix 1). This method would require a wave detector and accurate timing.

Alternatively, a train of waves could be produced and the wave velocity (phase velocity) ascertained from measurement of the wavelength. There are two frequency regions of interest for carrying this out. For low frequencies with larger wavelength, direct physical measurement of the wavelength can be made using a submerged graduated scale and strobed light. At higher frequencies, 350-700 Hz the crests behave like a diffraction grating creating a reflected diffraction interference pattern from incident laser light. By measuring the fringe spacing, and knowing the frequency from the driving signal, the velocity can be calculated.

Both these two measurements of wavelength were experimentally tested to examine the plausibility of detecting changes in wave velocity as an indication of monolayer coverage.

Hexadecanol decreases surface tension (Chapter 1), while increasing the surface viscosity (Saylor, Smith, & Flack 2000). The theoretical change in wave velocity due to halving the surface tension can be calculated from Kelvin's dispersion equation (Equation 2.18). This is a reasonable approximation to the effects of hexadecanol, since the effects of the viscosity and elasticity on wave velocity are negligible (Brown 2005:55).

Graduated scale technique

Surface waves were generated in a volume of tap water using a single plane styrene paddle 10 cm in length and 0.23 mm thick, attached to a 40 W 4 Ω speaker (Targa X-100 300 W, Philippines), by a hollow plastic tube. This was attached to the lower part of a plastic wine glass (shaped like a funnel) that was glued to the cone of the speaker with contact glue as shown in Figure 2.10(a). The speaker was driven with a sinusoidal waveform produced by a signal generator (Hewlett Packard 3312A, USA) which was amplified using an audio amplifier (Akai AM2350, Japan). It was found necessary to cushion the rim of the speaker on the stand with Styrofoam packs to minimize vibrations. Normally the rim would be attached to a solid frame, however with the weight of the speaker and Styrofoam cushioning, this was found unnecessary (Figure 2.10(b)).



(a)



(b)

Figure 2.10 (a) Paddle attachment to speaker.(b) Position of driving speaker fitted on a stand above the trough.

A high powered white light-emitting diode (LED) was powered by the same signal generator to provide a strobing illumination source with which to view the generated waves, shown in Figure 2.11. Under these illumination conditions the waves appear stationary, allowing the direct visual measurement of the wavelength using a ruler graduated in millimetres placed on the floor of the trough. Allowance needs to be made for the angle of divergence of the LED as the fringes shown are around 5 cm under the surface. The combination of known modulation frequency, f and measured wavelength, λ was used to determine the wave velocity, v , using $v = \lambda f$.

The hexadecanol used was obtained from stores, which was originally purchased from The British Drug Houses Ltd. (BDH). Other than being “technical” grade, no statement of purity could be found. As a monolayer, hexadecanol has the ability to reduce the surface tension by $\sim 40 \text{ mN m}^{-1}$ with full pressure coverage. At room temperature it forms solid white crystals, which can be dropped onto the water surface. The monolayer formed quickly spreads and covers a small surface in a matter of seconds. This is evidenced by the movement of the crystals apart as monolayer forms between them. While ever there is excess crystals on the surface, there is full surface pressure, and this is a very convenient way of knowing the surface pressure. The surface tension can be checked at any time by simply adding a pinch of crystals to the edge. If they do not move apart, the monolayer at full pressure is present. A photograph of the experimental apparatus is given in Figure 2.11.

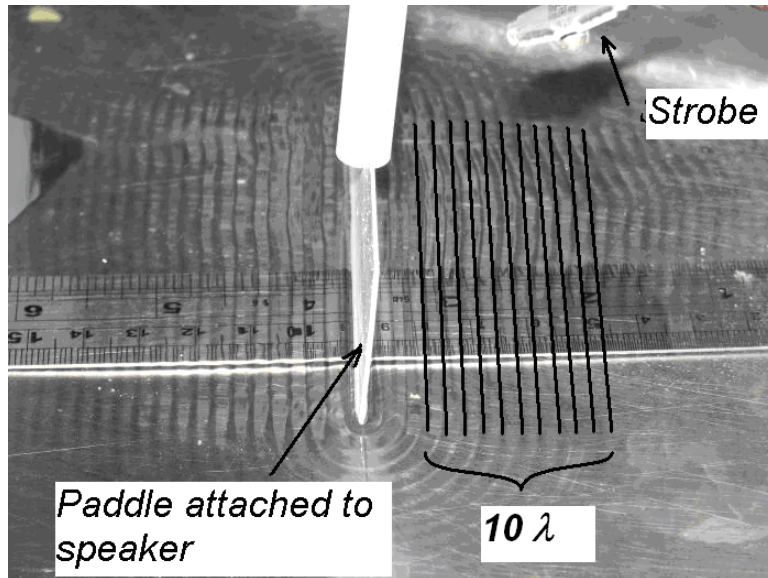


Figure 2.11 Setup for graduated scale technique running at 120 Hz. The strobe light on the upper right appears to hold the waves still so that the measurement of wavelength can be made.

The full possible frequency range of 8-250 Hz was investigated. Below 10 Hz the strobe did not show the peaks very well. Above 250 Hz the wavelengths were becoming too small to be counted. The velocity of waves corresponding to the measured wavelengths is shown in Figure 2.12 for both a clear water surface (black crosses) and a hexadecanol monolayer (red vertical crosses). Superimposed on these values are the theoretical velocity for pure water surface tension (72 mNm^{-1}) (solid black line) and that for half this value, similar to the surface tension of monolayer (red dashed line) is also shown, for comparison. These were determined by substituting these values of surface tension into Kelvin's dispersion equation (Eq. 2.18). The air temperature was 22-24 °C.

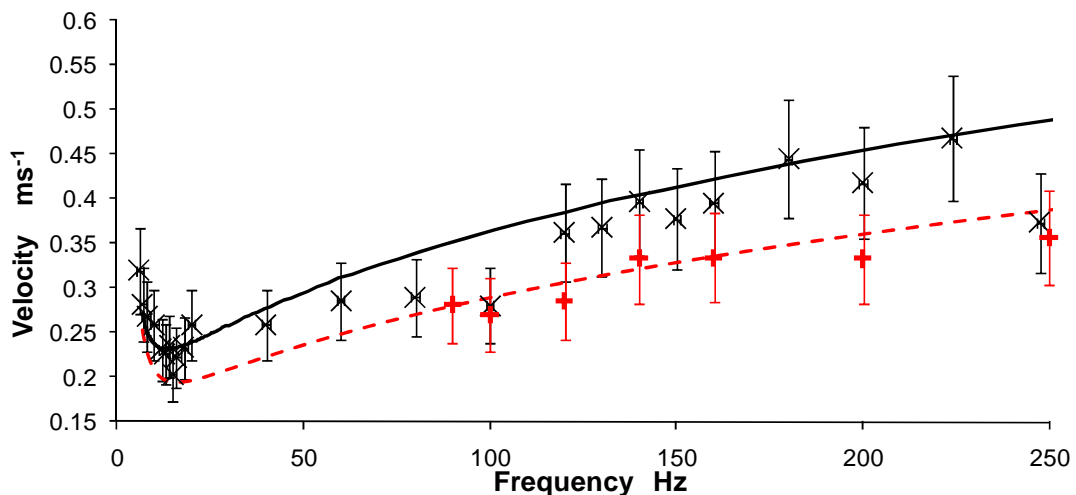


Figure 2.12 Theoretical and experimental values for surface velocity. Clear water (black), experimental (crosses) and theoretical (solid line). Hexadecanol (red), experimental (vertical crosses) and theoretical (dashed line). Uncertainty is estimated at 15% of value.

It can be seen that there is a measureable difference between the two plots. In the case of clear tap water, it can be seen that most of the data gathered for the capillary waves indicate a lower surface

speed than the theoretical values, indicating the surface tension was below that of pure water. The monolayer values fairly well reflect the theoretical 36 mN m^{-1} surface tension plot.

Measurements are more difficult using higher frequencies above 200 Hz due to the small size of the waves. Unfortunately this the frequency region where most difference is evident. Increasingly small waves may be difficult to measure visually, however their size moves them into an area where laser diffraction measurements are possible, and this will be tested next.

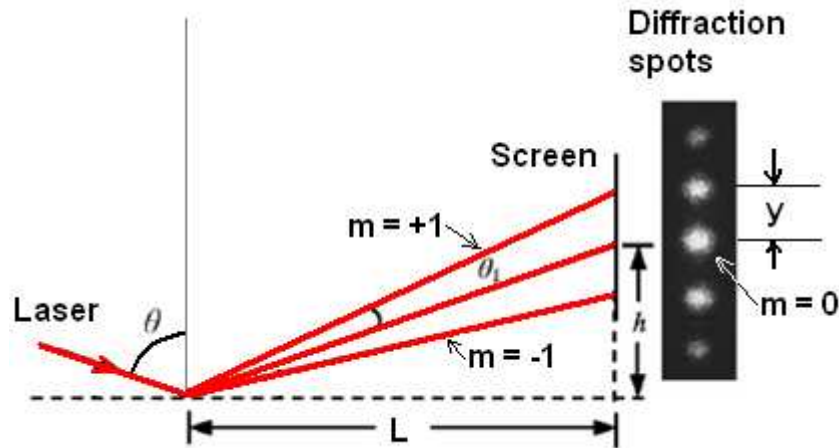


Figure 2.13 Diffraction pattern formed from laser reflection off capillary waves.

Diffraction pattern technique

The same wave generating apparatus was used as for the preceding experiment. A 20 mW He-Ne laser ($\lambda_{\text{He-Ne}} = 632.9 \text{ nm}$, 1135P Spectra-Physics, Oregon USA) was reflected from artificially generated capillary waves at the largest angle of incidence possible (74°) in order to clear the rims of the trough, and create an observable diffraction pattern on a screen at a distance of 3.5 m away (Figure 2.13). With this configuration, the wavelength of the generated waves, λ can be calculated from the separation of the diffraction maxima, y , and the wave-screen distance, L , using (Zhu *et al.* 2007):

$$\lambda = \frac{\lambda_{\text{He-Ne}} L}{y \cos 74^\circ} \quad (2.25)$$

Again, the combination of known modulation frequency, f and measured wavelength, λ was used to determine the wave velocity, v , using $v = \lambda f$.

For a clear diffraction pattern observed on the screen, the amplitude of the modulation paddle source was required to be approximately twice the magnitude than for the ruler measurements previously carried out. Accurate determination of the diffraction maxima or minima proved problematic owing to the poor contrast. This constrained the useable frequency range to between 400 and 617 Hz. For a frequency above 617 Hz the maxima appear to be separated by too large an angle and become too faint, while below 400 Hz the maxima become too close together and could not be clearly delineated. The results, showed an increase in average distance between diffraction fringes with increasing frequency, as would be expected. These results can be checked by

calculating the velocity at each wavelength using the capillary term of Kelvin's dispersion equation.

Photographs were taken of the diffraction pattern so that the separation of the maxima could be accurately determined using the image viewing software "Microsoft Paint". The distance between fringes was calculated from an average of as many fringes as visible (since the order angle is quite small). An example of the analysed image for the frequency of 617 Hz for clear water is shown in Figure 2.14(a).

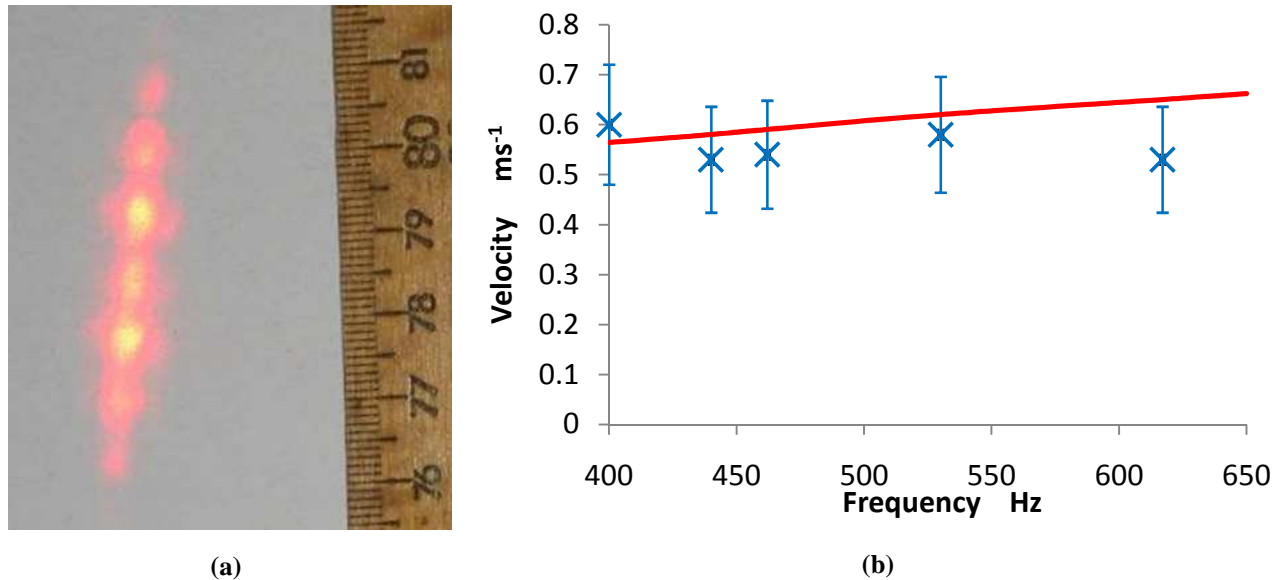


Figure 2.14 Results of diffraction of He-Ne laser off capillary waves. (a) Diffraction pattern produced by a laser beam reflected off the surface of surface waves. Modulation frequency = 617 Hz. (b) Comparison of measured velocities calculated from wavelengths (×), compared to theoretical velocities (—). Uncertainty was estimated at 20% of the velocity.

The results for tap water are shown in Figure 2.14(b). The measured wave velocities calculated from the measured wavelength show values slightly below the theoretical wave speed. This is again consistent with surface tension values slightly below pure water. However, when hexadecanol is added to the surface, the diffraction pattern disappears, and it was found impossible to obtain the diffraction pattern with monolayer.

The most likely causes would be a much larger damping coefficient at these frequencies leading to extinction of the waves much closer to the paddle. The ideal paddle sampling distance for water was found to be several cm and this distance was too large for monolayers. Repositioning of the laser closer to the paddle failed to produce any diffraction pattern.

2.4.2 Conclusion

Both the graduated scale and the diffraction pattern techniques showed differences with the addition of monolayer, and both also drawing attention to the initial decreased surface tension of storage (tap) water.

The manual measurement of wavelength is impracticable in a field situation, least of all as the basis of an automated system. Similarly, the laser diffraction technique requires the ability to accurately identify and position the diffraction maxima/minima, which in a controlled laboratory environment proved difficult owing to the width of these features. Indeed, like the ruler technique, the uncertainty in the derived wave velocities was comparable to the requirement of detecting a change in wave velocity resulting from the presence of a monolayer. It is conceivable that more accurate location of the diffraction pattern features could be achieved using a linear charge-coupled device (CCD) detector array and appropriate shape-fitting of the intensity profiles (e.g.(Zhu *et al.* 2007)). However, if this technique was extended to a field situation, parameters such as wave-sensor distance and laser incidence angle need to remain fixed, and this is difficult if the water level changes relative to the physical location of the source and sensor components. Coping with changing water levels would mean using a floating device; however this could mean instability in the laser incidence angle, which would alter the required position of the sensor. Stabilising the mechanism would mean using a static fixture to hold the apparatus against lateral movement, though allowing vertical movement due to altering water levels.

The results thus far suggest the velocity of a surface wave is not suitable for detecting the presence of a monolayer under field conditions. The diffraction method pointed to damping as showing potential differences and therefore is another physical characteristic that can be investigated.

2.5 Wave damping effects in the presence of a monolayer

The well known metaphor, “pouring oil on troubled waters” likens the calming effect on a person’s emotions to the fact that pouring oil on a water surface reduces the amplitude of surface waves. This can clearly be seen in Figure 2.15(a); a picture taken of an oil spill from the tanker, the Exxon Valdez.

The crude oil floating away from the tanker can be seen to be reducing the amplitude of wind generated surface waves causing an increase in specular reflection. Surface active layers generally, have a similar effect to oil, particularly in damping smaller waves. Figure 2.15(b) shows the spreading of hexadecanol across a water storage with a clearly defined downwind edge.

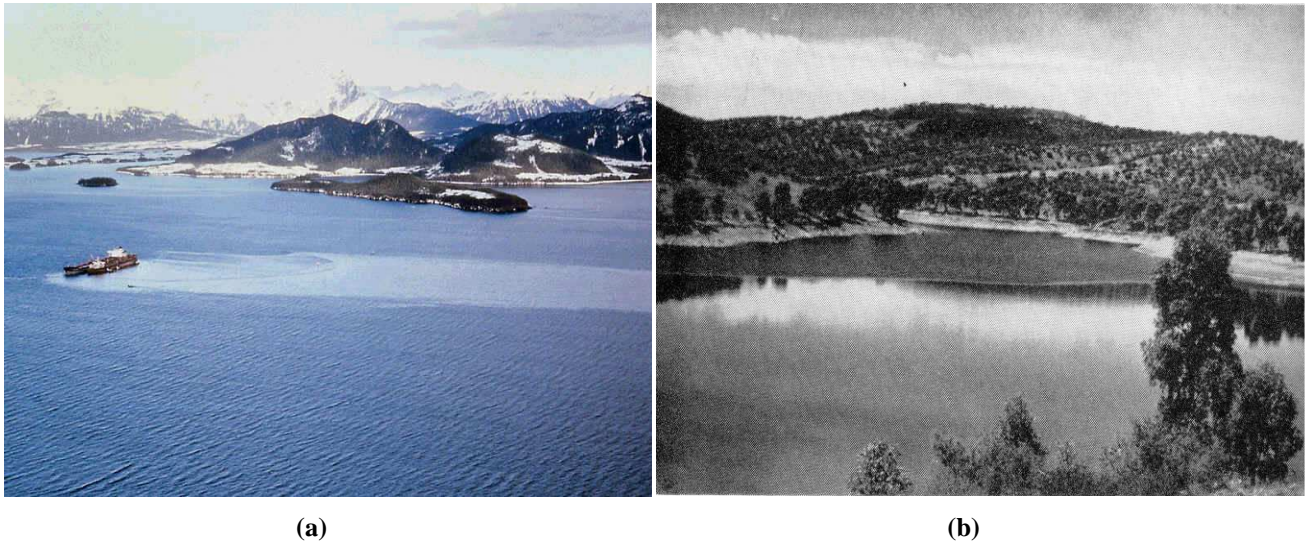


Figure 2.15(a) Oil Slick from the Exxon Valdez. Source; Solcomhouse (2009). (b) Spreading of Hexadecanol on Umberumberka Reservoir, Broken Hill (Vines 1962).

However, the clear evidence of wave calming in Figure 2.15(a) and (b), results from the ability to directly compare (and contrast) the regions of the water surface with and without the monolayer (or oil). If there is no monolayer present, or if the water surface is fully covered, this method cannot be used. Also the wind needs to be favourable. For low wind speeds below 1 m s^{-1} (Gottifredi & Jameson 2006) no waves are generated by winds to be damped in either background water or monolayer covered sample. For waves above 9 m s^{-1} , there is too much turbulence and the monolayer disappears (Tiblin, Florey, & Garstka 1962:184).

The cause of the increased damping is due to both the decrease in surface tension, and increase in viscosity, both leading to an increased dissipation of energy. Each will now be discussed in Section 2.5.3.

2.5.1 Microwave radar

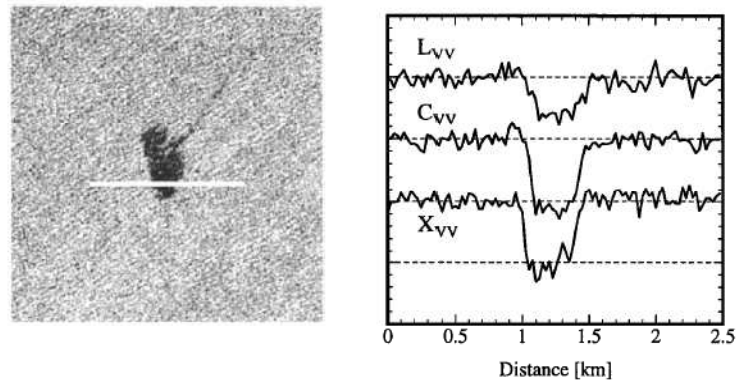


Figure 2.16 Scanlines through SIR (spaceborne imaging radar) SAR image aboard the space shuttle Endeavour, in the L, C and X bands of an oily alcohol slick at sea in the German Bight. The image on the left is in the X band. Each of the vertical dashed lines corresponds to a 10dB reduction in intensity. Source; (Gade *et al.* 1998).

Radar provides data concerning ocean roughness; the backscatter (intensity received) increasing as the wave height increases (Campbell 1996). So wind conditions and damping of films can be estimated, with an area of still water showing as a darker area.

Amongst the satellite methods, Synthetic aperture radar (SAR) has been shown to be the most efficient in detecting oil slicks (Karantzalos & Argialas 2008). SAR can operate under any conditions; day and night under clouds (Fingas & Brown 2000). The most suitable wavelengths are in the C ($\lambda=3.75-7.5$ cm) or X (2.5-3.75 cm) band, with the optimal wavelength for detection at 3-7 cm, as shown on the backscatter intensity in Figure 2.16.

The damping of waves is more efficient at smaller wavelengths, and therefore these bands give better results than the larger wavelength L (15-30 cm) or P (>1 m) bands. An antenna is used to emit and receive a “backscattered” radar signal for which the received signal is proportional to the sea surface roughness. Rough surfaces backscatter a large amount of energy back to the antennae, while smooth surfaces reflect the energy away from the antenna. Therefore rough surfaces produce bright signatures, while calmer smooth areas have dark signatures. This can be explained by looking at the two processes involved in backscattering microwave radar at the water surface, with the incident angle determining which is dominant. At small angles of incidence, below 20° , the backscattering is mainly by specular reflection, while at larger angles, Bragg scattering becomes dominant (Valenzuela 1978). No film detection is possible with specular reflection, while Bragg scattering forms a resonance through interaction of the radar signal with cm-scale capillary and short-gravity waves. This produces maxima in received power, at a resonance which occurs when the water surface wavelengths are of comparable in size to the radar wave length, as depicted in Figure 2.17.

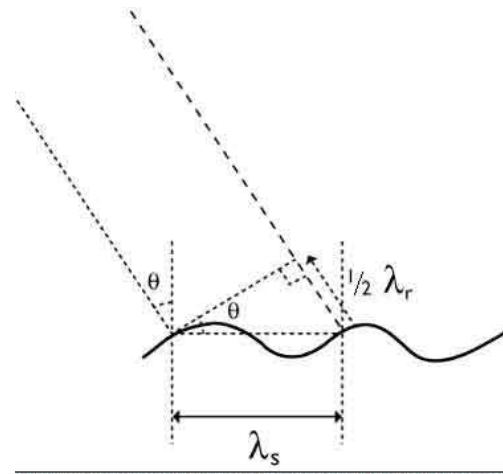


Figure 2.17 Phase interference for radar backscatter.

Maximum backscatter occurs when there is constructive interference, which occurs when:

$$\lambda_s = \frac{\lambda_r}{2 \sin \theta} \quad (2.26)$$

where λ_s is the wavelength of the waves, λ_r is the wavelength of the radar, θ is the incident angle of the radar on the surface.

Generally the wave-damping effect of oil slicks, biogenic films and monolayers causes a darkening of the covered area surrounded by brighter regions on an image. Because this detection method is dependent on damping of waves, the wind generation of the waves is important. With larger wind velocities, not only do the size of large gravity waves increase, but so do the radar-sized resonant Bragg waves (Valenzuela 1978). Wind speeds 3-6 m s⁻¹ are ideal to create a contrast between clear ocean and film. Wind speeds need to exceed a certain threshold of between 2-3 m s⁻¹ in order to generate Bragg-sized waves (Alpers & Espedal 2004). Depending on the thickness of the film, a wind speed above somewhere between 10-14 m s⁻¹ makes the film undetectable (Alpers & Espedal 2004), caused by mixing in the upper ocean layer, and redistributing the film by breaking waves. Some other natural processes can produce a similar image with equal contrast such as quite common biogenic films from aquatic animals and plants (Alpers & Espedal 2004) internal waves, upwelling, low wind areas, “greasy ice”, rain and floor topography, all damp Bragg waves and these need to be eliminated.

2.5.2 Longitudinal Marangoni waves

As discussed previously, the surface area of any surface films changes as a result of the circular ‘motion’ within waves and this is resisted by the dilational elasticity of a surface film. This causes longitudinal waves, called Marangoni waves, to propagate in the film. The longitudinal behaviour of Marangoni waves leads to a higher energy dissipation due to the inertial mass of the water-film system (Alpers & Huhnerfuss 1989). The restoring force for Marangoni waves is a tangential force associated with surface tension gradients which are determined by the viscoelastic properties of the

surface film (Alpers & Hühnerfuss 1988). As a consequence, Marangoni waves draw energy from the capillary waves and increase the damping effects.

The fact that the Marangoni waves are strongly damped is the reason why these waves have long escaped detection. Their existence was verified experimentally by Lucassen (1968) who performed experiments with monolayers at a frequency of 200 Hz and found that the dilational elasticity modulus is several times greater than that found using force-area curves. Whilst Lucassen found that many monolayers that were sufficiently compressed were able to transmit longitudinal waves, he observed that for some monolayers such as hexadecanol and palmitic acid their appearance had a transient nature, possibly caused by collapse of the monolayer due to compression by the wave generator. To regenerate the wave a repeated compression of the monolayer was required. He found cholesterol and lecithin monolayers gave the best reproducible values for wavelength and damping of longitudinal waves (Lucassen 1968).

As both Marangoni and transverse waves co-exist on film-covered water and the wavelength of each is frequency dependent, there is a frequency at which the wavelengths of the two types of waves coincide (Figure 2.18(a)), when resonant coupling occurs. This has been observed to be in the range of 3-8 Hz. At this frequency, the increased coupling between the transverse and Marangoni waves results in a maximum damping efficiency (Lucassen 1968; Vogel & Moebius 1989). Alpers and Hühnerfuss (1988) observed the amplitude of the decaying waves using radar backscatter (the damping ratio calculated in decibels (dB)) and confirmed this frequency range. Experimental data confirming the effect of Marangoni waves has been found by Gade (2005) in a wind tunnel Figure 2.18(b).

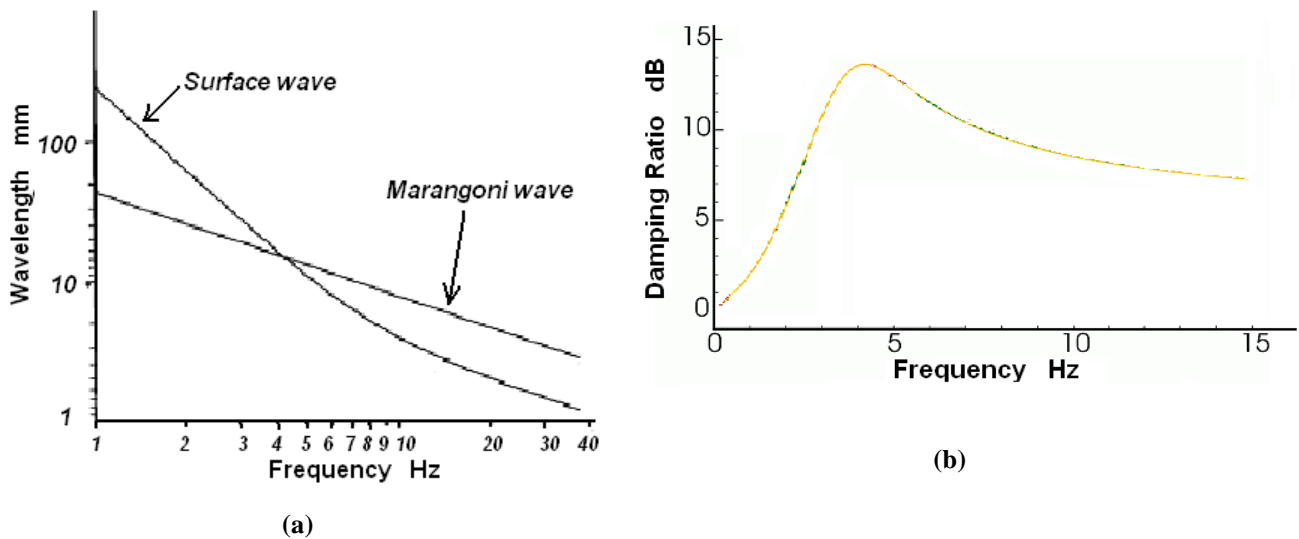


Figure 2.18 Marangoni waves. (a) Wavelength- Frequency region where they occur for a surface covered with hexadecyl-trimethylammonium bromide (CEM3AB). Adapted from Alpers & Hühnerfuss (1988). (b) Theoretical damping of hexadecanol. The damping ratio compares damping with monolayer compared to a clear water surface. Adapted from Gade (2005).

Gade (2005) has calculated the theoretical damping for hexadecanol with an absolute value of dilational elasticity ε of 0.0345 N m^{-1} at full pressure for these frequencies. These are shown in (b). The maximum damping occurs at 4.2 Hz with a reduction in wave amplitude, compared to clean water by 10-25 dB.

Experimental results gained by (Hühnerfuss *et al.* 1981) (Figure 2.19) using the monolayer-hexadecyl-trimethyl-ammonium-bromide, show how the Marangoni effects create damping at low frequencies, and larger damping occurring at higher frequencies. The wave energy was calculated from amplitude measurements using a single thin wire ($40 \mu\text{m}$ diameter tungsten) resistance probe in a wind tunnel under winds of 8 m s^{-1} .

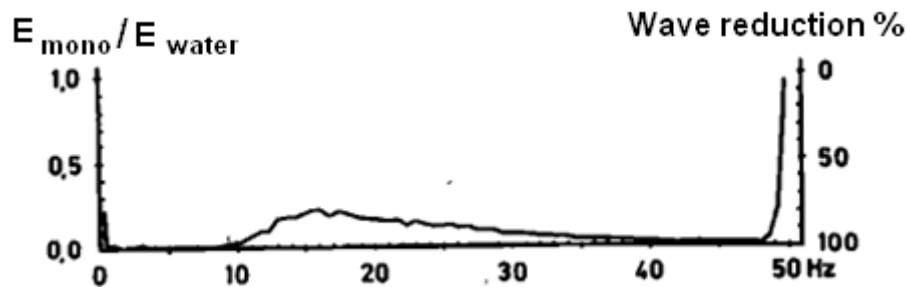


Figure 2.19 Experimental results from (Hühnerfuss *et al.* 1981), showing reduction in wave energy interaction with Marangoni waves (left hand peak), and due to viscosity caused by dilational elasticity (right hand asymptote) for hexadecyl-trimethyl-ammonium-bromide monolayer.

2.5.3 Damping of water waves

Energy is dissipated as capillary waves propagate along a clean water surface damping wave and reducing their amplitude (Figure 2.20). The two main effects which affect damping for water are viscous interaction with the water floor, and viscous drag due to the internal elliptical motion of the particles within the fluid itself. This elliptical motion gradually decreases with increasing depth, so for troughs with a depth exceeding $\frac{1}{2} \lambda$ this energy dissipation is insignificant as explained in Section 2.3.5. This work is primarily concerned with deep water so troughs were always used with a depth larger than $\frac{1}{2} \lambda$.

The wave function describing the local disturbance associated with a surface wave can be considered the combination of the sinusoidal function (the waveform) and an exponential decay function (energy loss):

$$\psi = e^{-\delta x} \cos kx \quad (2.27)$$

where ψ is the wave amplitude, δ is the exponential decay coefficient (m^{-1}) and x is displacement. Both terms in this equation can be visualized using Figure 2.20.

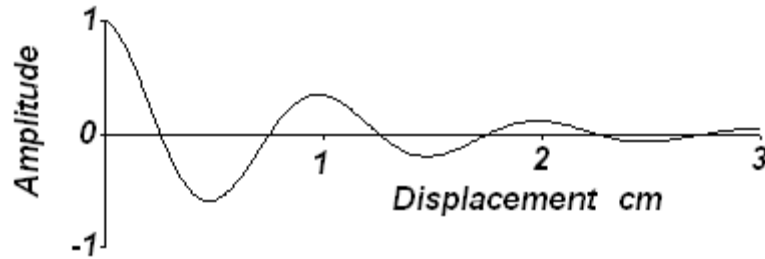


Figure 2.20 Damping of surface waves.

2.5.4 Damping due to bulk viscosity

For clear water Lamb (1932:624) derived the loss of energy by allowing for the effects of viscosity due to internal motion of the wave. The viscosity of the bulk liquid is the controlling factor in damping clean water. For capillary waves where the wavelength is $\lambda < 0.5$ cm, the amplitude decay factor due to viscosity is:

$$\delta_v = \frac{2\eta k^2}{\rho v_g} \quad (2.28)$$

where δ_v is the exponential decay due to bulk viscosity, η is the dynamic viscosity of the bulk liquid, ρ is the density of the liquid and v_g is the group wave velocity.

The group velocity $v_g = v - \lambda \frac{dv}{d\lambda}$ is rather difficult to calculate. For capillary waves it can be equated to wave velocity in the relation:

$$v_g = \frac{3v}{2} \quad (\text{See Appendix 1}) \quad (2.29)$$

On substitution this leaves: $\delta_v = \frac{16\pi^2\eta}{3\rho\lambda^3 f}$

This is still a rather cumbersome relation to use however as the damping constant is proportional to frequency and the frequency variable is on the denominator.

An approximation for δ_v based on experimental results under similar conditions for water (Goodrich (1962) is

$$\delta_v = \frac{8\pi\eta f}{3\gamma} = \alpha f \quad (2.30)$$

which eliminates the need to calculate the group velocity. Interpreting Goodrich's (1962) results, the damping frequency coefficient α is 0.113 s m^{-1} for water at 20°C . This is an empirical relationship estimating damping due to internal viscous energy losses which can only be used on water which has stress free surface. This relationship also displays an inverse relationship between

surface tension γ and damping coefficient δ . A reduction in the restoring force (surface tension), results in larger wave amplitude for the same amount of input energy. Larger wave amplitudes correspond to proportionally larger fluid element velocities and shear rates leading to a higher damping coefficient (Behroozi *et al.* 2007).

2.5.5 Damping due to a non-zero surface dilational elasticity

Monolayers resist surface compression (McArthur 1962), as they possess non zero dilational elasticity (Section 1.8.3). Thus the presence of a monolayer creates an elastic surface with higher viscosity than clean water (Behroozi *et al.* 2007) and this interferes with the natural circular motion of wave propagation (Goodrich 1962). The resulting viscous energy losses lead to a higher damping rate (Alpers & Huhnerfuss 1989). This surface damping likely occurs for all waves, however it is much more noticeable in small gravity waves as shown from experimental data in Figure 2.19. For the purposes of investigating the potential of wave damping as the basis of an objective sensor of monolayer presence/absence or quantity, it is instructive to examine the underlying physics in more detail.

The dilational modulus, ε , of a surface describes the change in the surface tension γ that occurs with a fractional change in area A of a given surface element. It is defined as:

$$\varepsilon = \frac{d\gamma}{d(\ln A)} \quad (2.31)$$

For a sinusoidal wave of phase speed w , the modulus alters because of the many possible relaxation processes occurring after the deformation, which is dependent on frequency. Therefore the modulus can be separated into static and dynamic parts (Bonfillon & Langevin 1993):

$$\varepsilon = |\varepsilon|e^{i\theta} = \varepsilon_0 + i\varepsilon_v \quad (2.32)$$

where θ is the phase lag between the stretching of the surface and a corresponding change in surface tension. The real part of the dilational modulus ε_0 , is called dilational elasticity which can be calculated from the gradient of the π - A isotherms (Section 1.8.3). Its value varies widely depending on the gradient and phase of the representative isotherm. Behroozi (2007) measured a value for octadecanoic acid of 3-4 mN m⁻¹, however Gottifredi & Jameson (1968) estimates a higher value of at least 10 mNm⁻¹ for most monolayers. The imaginary part is the time-dependent dilational viscosity, from which the surface dilational viscosity η_d can be calculated using $\varepsilon_v = \eta_d \omega$ (Behroozi *et al.* 2007; Caseli 2005). Kolevzon(1999) has shown by theoretical considerations that η_d generally has a value of around 10⁻⁴ mN s m⁻¹ for monolayers. Experimental measurements of octadecanoic acid at 20 °C, reported by Behroozi (2007) showed a higher value of η_d of 2-5 × 10⁻⁴ mN s m⁻¹. This term is directly related to the frequency-dependent damping of waves. The nature of the energy losses associated with wave damping is difficult to determine due to the complicated nature of energy coupling into surface compressional modes (Behroozi *et al.* 2007). However it is important to note that the surface modulus limits horizontal movement of the surface and that its effect increases with frequency.

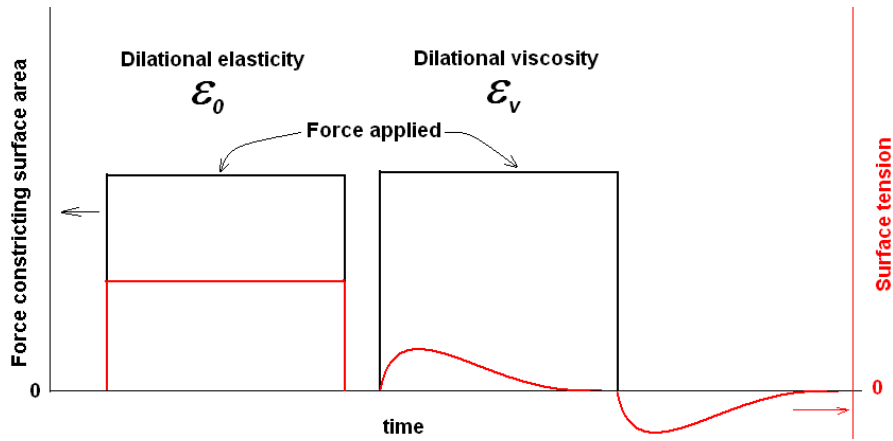


Figure 2.21 Difference between elastic and viscous behaviour.

The difference between the real and imaginary parts of the dilational modulus is depicted in Figure 2.21. The real part is the elastic change in surface tension corresponding to a change in surface area as shown on the left side. Similar to a rubber band, the change to surface tension is held, and is therefore called elastic dilational modulus. A surface such as monolayer possessing non-zero dilational elasticity changes surface tension, in accordance with area/molecule and it remains at that value. Dilational viscosity (shown on the right), on the other hand, causes a delayed momentary change in surface tension as a result of changing the surface area, and is therefore proportional to frequency of waves.

As a transverse capillary wave passes, the circular motion of the fluid elements that make up the wave naturally compress the surface at wave fronts and stretches it on the rear of the wave, so energy is coupled into compressional waves not unlike compressions and rarefactions of a longitudinal wave. A monolayer on the surface will resist these compressions (Goodrich 1962) as shown in Figure 2.22. The circular motion of the wave fluid elements immediately below the monolayer become elliptical as tangential shear forces limit their horizontal motion. This elliptical motion similarly results in greater shear between successive layers of water below, drawing away energy more rapidly due to viscous dissipation, which results in an increase in damping (Behroozi *et al.* 2007). It has been determined that the drag interaction of hydrophilic films must exist to a depth of at least 0.03 mm (Jarvis 1962; Schulman & Teorell 1938).

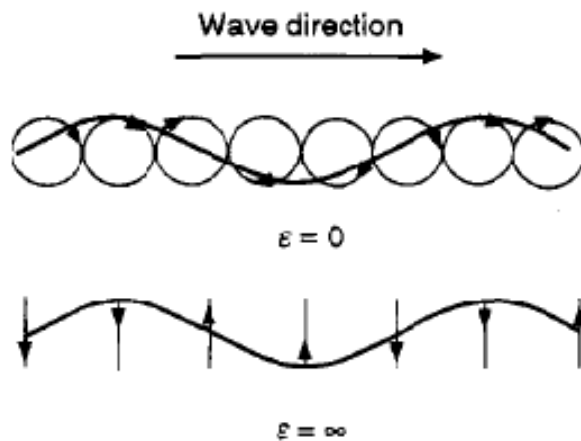


Figure 2.22 The movement of surface elements when the dilational modulus is zero and infinity. Source (Barnes & Gentle 2005).

Theoretical calculations made by McKenna & Bock (2006) suggest there are large velocity gradients set up in the top 0.3 mm which lead to viscous energy dissipation in cases of large dilational elasticity of 30 mN m^{-1} . The wave studied was 15 Hz under a wave crest with amplitude to wavelength ratio of 1:20.

Imaging of capillary wave compression, on crests and dilation effects on troughs on monolayers was first provided by Korenowski *et al.* (2006). They used circular waves of wavelength 2 mm (240 Hz) and an insoluble monolayer compound comprising a stilbazolium dye molecule attached to a C_{22} chain. A 532 nm wavelength, unfocussed, 8 mm in diameter laser beam was directed at 60° to the surface. The crests and troughs exhibited sufficient contrast to enable them to be photographed, with dark areas represent higher concentrations of dye at the crests and the lighter areas corresponding to lower dye concentrations in the troughs. The equilibrium still surface concentration of dye on the surface was estimated to be $0.288 \mu\text{g cm}^{-2}$. While in the troughs and crests of their circular waves they observed surface concentrations of $0.250 \mu\text{g cm}^{-2}$ and $0.330 \mu\text{g cm}^{-2}$, respectively. These results show clearly the compaction of monolayer on the wave crests, and dilation in the troughs. McArthur (1962) also noticed this compression of hexadecanol on the crests of waves on a 770 Ha loch in Scotland. He describes a breakdown of monolayer on the water surface into “fine filaments” on the crest of waves before disappearing again in the lower pressure area of troughs.

Damping of partial pressures of monolayers

Investigators have found that there appears to be an optimum ‘concentration’ of surface film to facilitate damping via coupling between transverse and Marangoni waves (Lucassen (1968). Tailby & Portalski (1961) showed that certain, and relatively low concentrations of the detergent “Teepol L” were sufficient to almost completely eliminate visible ripples. Higher concentration of the detergent either has no greater effect, or actually restored the waves. For monolayers, there too appears to be a complex relationship between damping constant and surface pressure (Lapham, Dowling, & Schultz 2001). For the frequency region 100–1000 Hz the relation between damping per area of film molecule film shows a maximum corresponding to the transition region between the ‘gas’ (G) and ‘liquid’ (LE/LC , ‘liquid expanded’ and ‘liquid condensed’) phases of the monolayer (Dysthe 1986; Garrett & Zisman 1970). This complex was explained in terms of energy absorption of the surface film caused by changes to the intermolecular arrangement as well as by changes in the “drag” or hydrogen-bonding interaction between the film and water surface (Garrett & Zisman 1970). Measurement of the damping constant of oleic acid was performed by Jarvis *et al.* (1967) at a frequency of 60 Hz on sea water. They also found the damping increases with the change of phase from gas to liquid, then rises to a maximum value at relatively low film pressure of 11 mN m^{-1} . Based on experiments, Wang (1994) noticed that as surface pressure increases, the beginning of surface damping by the monolayer occurs when the width of the forming LE regions is larger than the wavelength of the capillary wave. It follows that the monolayer itself can physically ‘slip’ over the surface of the capillary wave. Once the liquid regions are larger than a

wavelength both extension and contraction are being applied, creating the viscous damping behaviour.

2.5.6 Surface damping effects due to monolayers.

Damping due to a reduction in surface tension

Both a reduction in surface tension, and possession of dilational elasticity caused by monolayers contribute to the damping coefficient. Behroozi (2007) found these can be separated by adding 5% acetone (by weight) to pure water. The mixture has a similar surface tension (54.5 mN m^{-1}) to olive oil (52 mN m^{-1}) (Nova Scotian Institute of Science 1956:54) being tested, however possessing no dilational elasticity. The density of the mixture (990 kgm^{-3}) is also close to that of water. Using a frequency of 307 Hz, the acetone-water had a damping coefficient of 47 m^{-1} compared to pure water with 37 m^{-1} ; consistent with the inverse proportionality between damping coefficient and wave frequency in Equation 2.30.

At the same frequency of 307 Hz the damping coefficient for olive oil was found to be of 102 m^{-1} , more than double the effects of decreasing the surface tension. This indicates that most of the damping for monolayers originates from the dilational elasticity. For the olive oil monolayer this would equate to only 15% of the increased damping due to the reduction in surface tension, while the remaining 85% is due to the viscous dissipation from the dilational elasticity Behroozi (2007).

Damping due to the dilational elasticity ϵ_0 of monolayers

As discussed previously (Section 2.5.5), the circular wave motion causes contraction of the surface at wave crests and extension in the troughs (Lamb 1932:628). This action creates no energy loss for a clear water fluid as there is no change in surface tension (Earnshaw & Hughes 1991). However, when there is resistance to compression (Davies & Vose 1965), as in the case of monolayers, the surface resists the lateral component of the circular motion, increasing the velocity gradients at the surface (Wang 1994) creating viscous energy losses underneath. The consequent motion of the surface and of the attached substrate layer occurring in the direction of increasing surface tension causes a drag on the liquid, increasing the rate of energy dissipation (Davies & Vose 1965), resulting in additional surface damping.

Water particles responding to the circular motion of waves are hindered by the horizontal immobilization of the surface caused by the monolayer. For a completely laterally immobile surface, the surface dilatational elasticity $\epsilon_0 = \infty$. Then the decay constant, δ_s for the displacement amplitude is (Lamb 1906:571):

$$\delta_s = \frac{\sqrt{\frac{\eta k^2 \omega}{8\rho}}}{v_g} \quad (2.33)$$

where v_g is the group velocity η is the dynamic viscosity of the fluid, and ρ is the density of the fluid.

The total damping amplitude decay could be assumed to be the sum of the two energy loss mechanisms; $\delta = \delta_v + \delta_s$ in the equation:

$$A = e^{-(\delta_v + \delta_s)x} \cos kx$$

However the experimental evidence of Vines (1959) indicates δ is much less than the addition of the two terms, and the discrepancy increases with increasing frequencies.

Given this chapter is not so much concerned with the delineation of the components of any differences in damping as a result of monolayers, rather that there is or is not a difference when a monolayer surface is compared to that of clean water, a combined empirical damping term δ will be used.

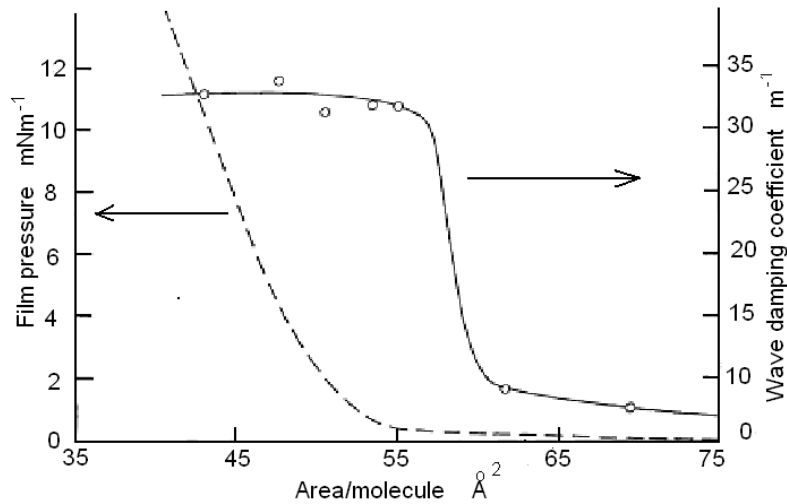


Figure 2.23 Wave damping coefficient; Solid curve plotted with isotherm; dashed line, for oleic acid at 60 Hz. (Jarvis *et al.* 1967).

Damping at a fraction of full monolayer pressure

Determination of a monolayer partial surface pressure therefore would seem unobtainable due to the lack of linearity between surface pressure and damping coefficient. In any case, a full pressure monolayer should show a measureable increase in damping over a clear water surface, particularly for smaller capillary waves, as shown by results obtained by Jarvis *et al.* (1967) for oleic acid (Figure 2.23). These results also show the drastic increase in damping occurring around the phase change of gas (G) to liquid (LE) as noticed by Wang (1994).

To determine the ease of measurement and this damping difference, several methods of detecting the damping coefficient using artificially generated waves and non-contact methods of damping monitoring were conducted. The most promising methods are shown below.

2.6 Experimental measurements of wave damping in the presence of monolayers

2.6.1 Amplitude of capillary waves from a single paddle using a reflected laser beam.

Measuring the wave-damping coefficient associated with capillary waves poses a challenge; especially given the rapid decay of these waves compared with larger waves, and small amplitudes, of order μm , being measured (Behroozi *et al.* 2007; Goodrich 1962). A He-Ne laser beam reflected off the surface will ‘dance about’ as a result of waves passing under the incident beam. Here the modulating nature of the wave surface will regularly modulate the angle between the surface normal and the incident beam. The change in incident angle will in turn modulate the reflection angle and hence the positions of the reflected laser beam on a distant screen (Figure 2.24). The geometry of the laser path can be used to determine the wave amplitude. If the wave amplitude is measured at a series of points with the distance between them known, then the damping characteristics can be determined, without needing to know the distance to the wave source.

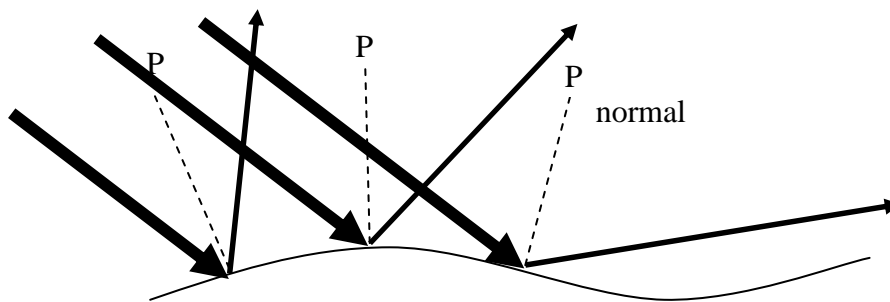


Figure 2.24 Schematic diagram depicting the varying laser incident angles (heavy arrows) on the surface of water as the surface normal (dash lines ‘P’) varies as wave moves through the point of incidence. Light arrows depicts varying reflection angles.

2.6.2 Shape of waveform

The ratio of maximum elevation to the wavelength A/λ has an effect on wave profile, and wave velocity (Lamb 1932:417). It is convenient, when discussing the wave shape to refer to the kA value, where k is the wave number and A is the amplitude. It was shown by Rayleigh (1847), that the shape of the wave is determined by the kA value.

For low kA values such as 1.1×10^{-3} the wave is sinusoidal, as determined by using theoretical predictions of wave shape (Lamb 1932:418) as shown in a comparison of a sine wave and the predicted shape in **Figure 2.26**.

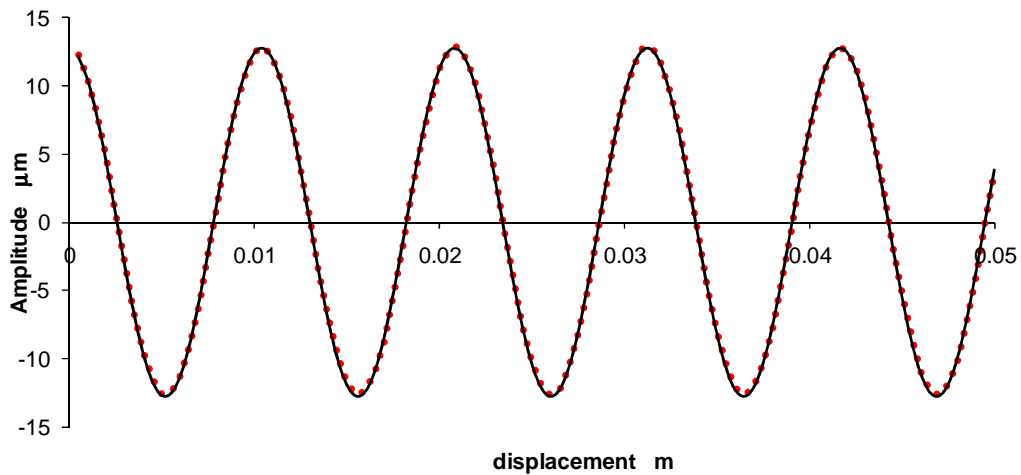


Figure 55 Low value of kA . This plot is 20 Hz with $k = 603 \text{ m}^{-1}$ and A of $12.81 \text{ } \mu\text{m}$; therefore a kA value of 1.1×10^{-3} . No difference in maximum gradient is seen between a $\cos kx$ shape; solid black line and the trochoid; red dashes.

At higher values of kA , such as 0.367, a trochoid shape begins to become evident. Trochoids can be visualized using a point on the circumference of a rolling drum, where the point is moving in the opposite direction to the direction of motion (Figure 2.26). The amplitude used is 1 mm, and at the lowest wave velocity wavelength of 1.71 cm. The trochoid shape only occurs in gravity waves where kinetic and potential energy do not form a linear relationship with height, so it requires less water to be moved higher in the crests to equal the energy involved in depressions of less amplitude.

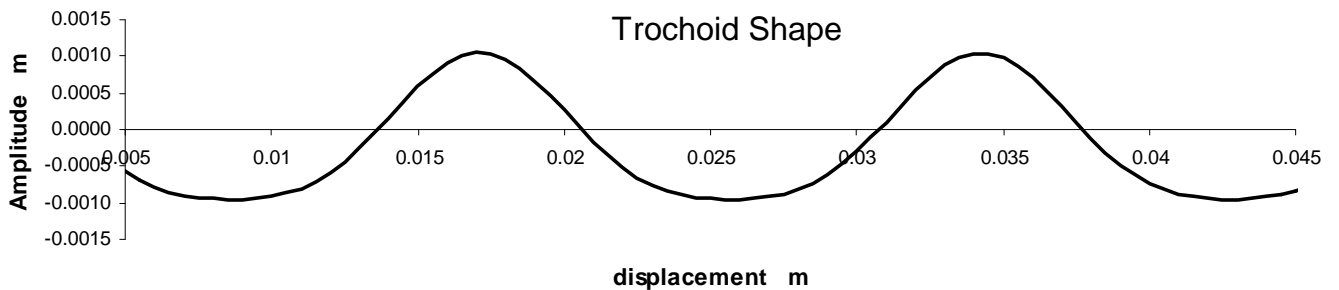


Figure 2.26 The profile of the trochoid is shown below for a kA value of 0.367. This corresponds to an amplitude of 1 mm at the lowest wave velocity wavelength of 1.71 cm.

Capillary waves have the surface tension acting to restore the wave equally for both the crests and troughs and are therefore sinusoidal in shape. Some of the measurements are gravity waves (frequency $< 13 \text{ Hz}$) however the amplitude is small, of the order of micrometres. So for wave reflection measurements the kA value is very small and a sinusoidal wave shape can be assumed.

The instantaneous amplitude is therefore:

$$y = A \sin kx \tag{2.34}$$

so the gradient would be

$$\frac{dy}{dx} A \sin kx = -Ak \cos kx \quad (2.35)$$

and the angle corresponding to this will then be

$$\theta_g = \tan^{-1}(-Ak \cos kx) = -\tan^{-1}(Ak \cos kx) \quad (2.36)$$

The angle of incidence α (measured from the perpendicular) of the laser needs to be smaller than this angle for the laser radiation to remain in contact with the wave surface. Above this angle, values of scattering is only measured for part of the wave

An angle perpendicular to this can be found by adding 90° to determine the angle perpendicular to the surface

$$\theta_p = -\tan^{-1}(Ak \cos kx) + 90^\circ \quad (2.37)$$

Perpendicular to wave

$$\theta_p = -\tan^{-1}(Ak \cos kx) + 90^\circ$$

Laser angle of incidence from perpendicular

$$\theta_i = \alpha - \theta_p \quad \text{so}$$

So

$$\theta_i = \alpha - [-\tan^{-1}(Ak \cos kx) + 90^\circ] = \alpha + \tan^{-1}(Ak \cos kx) - 90^\circ$$

Half the angle of scatter is then

$$\begin{aligned} \theta_r &= \theta_i - \theta_p = [\alpha + \tan^{-1}(Ak \cos kx) - 90^\circ] - [-\tan^{-1}(Ak \cos kx)] \\ &= 90^\circ - \alpha + 2 \tan^{-1}(Ak \cos kx) \end{aligned} \quad (2.38)$$

The maximum can be found by letting $\cos kx = 1$

$$\text{Max } \theta_{\max} = 90^\circ - \alpha + 2(\tan^{-1} Ak) \quad (2.39)$$

and the minimum by letting $\cos kx = -1$

$$\text{Min } \theta_{\min} = 90^\circ - \alpha + 2(\tan^{-1} Ak) \quad (2.40)$$

The difference, or angle of scatter would therefore be:

$$\theta_s = 4 \tan^{-1} Ak \quad (2.41)$$

Now, if the gravity term in the dispersion equation (Equation 2.18) for wave velocity is ignored for capillary waves (see Figure 2.7), this leaves

$$v^2 = \frac{\gamma k}{\rho} \quad (2.42)$$

Dividing by $\lambda^2 = \left(\frac{2\pi}{k}\right)^2$ leaves $f^2 = \frac{\gamma k^3}{\rho 4\pi^2}$ (2.43)

On rearranging

$$k = \sqrt[3]{\frac{f^2 \rho 4\pi^2}{\gamma}} \quad (2.44)$$

So the angular spread of reflection $\theta_s = 4 \tan^{-1} \left[A \left(\sqrt[3]{\frac{f^2 \rho 4\pi^2}{\gamma}} \right) \right]$ (2.45)

The amplitude can therefore be calculated from the scattering angle using a rearrangement

$$A = \frac{\tan\left(\frac{\theta_s}{4}\right)}{\left(\sqrt[3]{\frac{f^2 \rho 4\pi^2}{\gamma}}\right)} \quad (2.46)$$

This relationship overestimates amplitude by around 30% at low frequencies around the velocity minimum at 13 Hz due to dropping the gravity term in the dispersion equation. However this overestimation reduces to below 5% by 50 Hz, and continues to lower with increasing frequency.

Materials and Methods

A single plane styrene paddle attached to a speaker, as described in Section 2.4.1 was positioned above a trough was made of a plastic 200 litre drum sliced in half. which was filled with tap water as shown in Figure 2.57.

The paddle speaker assembly produces a region of linear waves, which can be used to assess the damping constant.

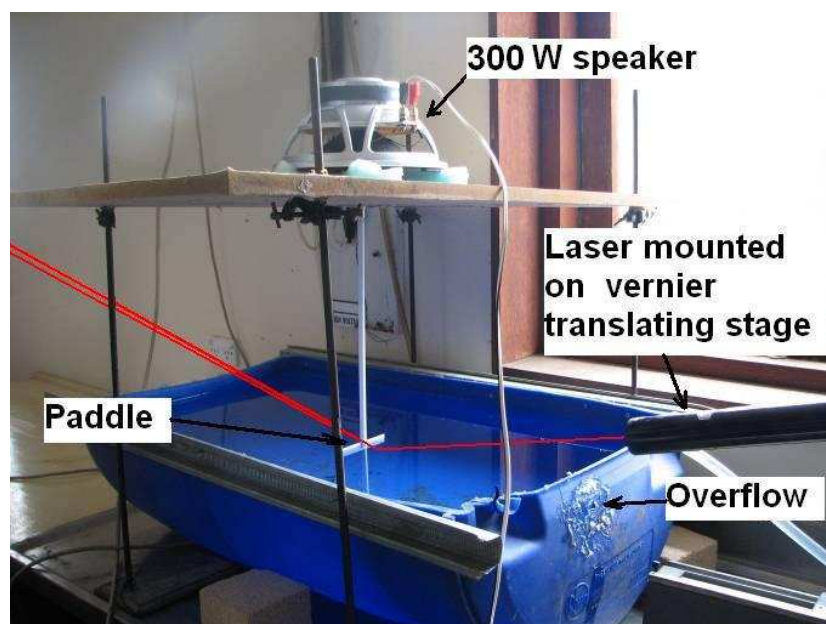


Figure 2.57 Single paddle with incident laser mounted on vernier scale.

A 20 mW He-Ne laser ($\lambda = 632.9$ nm, 1135P Spectra-Physics, Oregon USA) was attached to a vernier translating stage capable of translating the point of incidence of the laser beam on the water surface with an accuracy of 0.1 mm. The laser beam was directed at an angle of incidence at the water surface (still water) of 74° , with a point of incidence ranging from 5-15 mm from the paddle. The reflected beam, and its modulation in response to generated capillary waves was projected onto a distance screen, positioned at a distance of 4.10 m from the point of incidence on the water surface, and oriented normal to the mean beam direction.

Once the waves were initiated, the modulated reflection pattern of the laser beam on the screen was photographed (Figure 2.58) and the amplitude of the beam modulation found by comparing the upper and lower extremities with a co-located ruler using the drawing software Microsoft Paint.

The amplitude of the modulated laser beam was measured as a function of the distance between the point of incidence and the paddle; here the point of incidence was varied using the laser translation stage. For each resulting amplitude-distance curve, the decay constant δ was calculated using an exponential curve fitting for a full set of measurements of translating the laser as shown in Figure 2.59. The δ values were determined for the full range of frequencies 60–420 Hz, which would show a useable exponential decay curve, at intervals of 60 Hz.

This method was used for samples of clean water and water with a hexadecanol monolayer at full pressure (excess crystals floating on the surface).

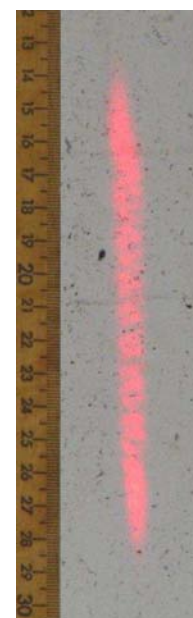


Figure 2.58 Reflection pattern on screen with a co-located ruler used to gauge its length in image processing software.

Results and Discussion

A typical graph of measured wave amplitude versus distance from paddle is shown in Figure 2.59 for hexadecanol monolayer with waves generated at 60 Hz. The smooth line drawn on this graph is that generated using an exponential curve-fitting routine in MS Excel 2003 (Microsoft Corporation, Seattle, USA). Certainly the data follows the exponential shape as predicted by Equation 2.27 and is similar to results obtained by Lucassen (1968) using a vibrating bar attached to two speakers, and a piezoelectric wave sensor used to convert the wave motion to an AC signal. The deviations from the exponential shape occurred often in data, and were thought to be caused by resonance vibrations in the paddle, speaker or supporting stand.

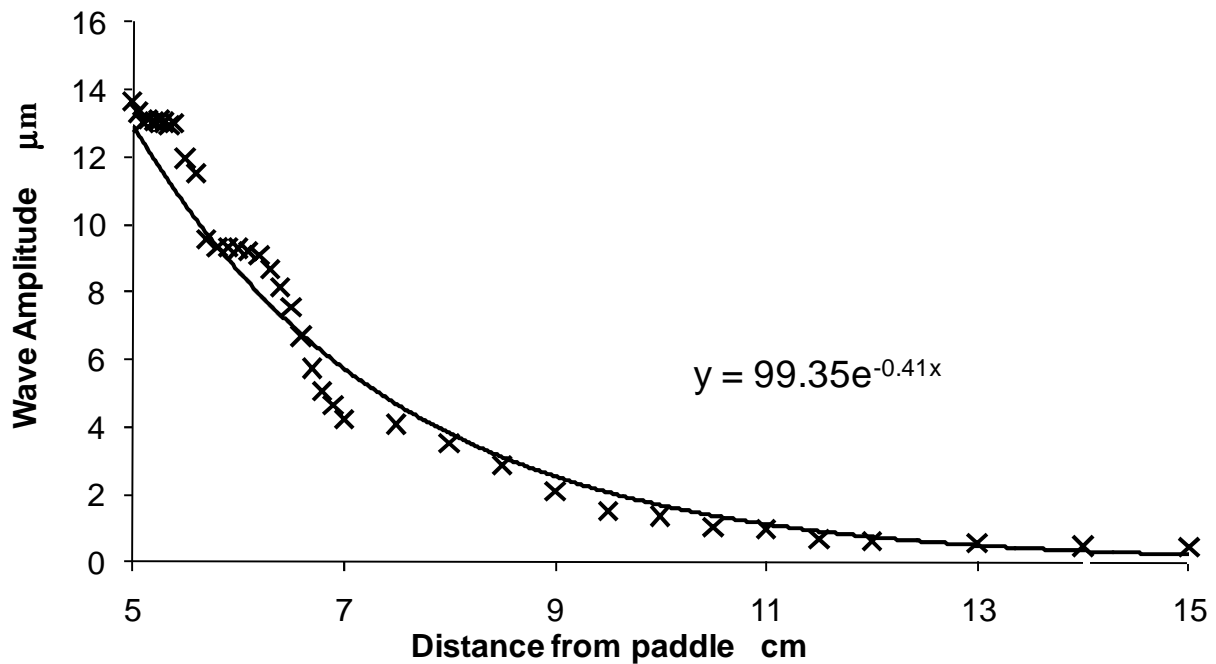


Figure 2.59 Typical wave amplitude decay for hexadecanol surface @60 Hz. An exponential trend line was fitted with the result showing a decay constant of 41 m^{-1} .

In practise, acquiring smooth data profiles required careful location of the point of incidence of the laser beam on the water surface. Positioning the beam too close to the paddle displaced the reflected beam (and its modulation envelope) away from the co-located ruler, possibly due to the wave shape being non-sinusoidal. Positioning the point of incidence too far away from the paddle gave a modulation amplitude that was too small to accurately quantify using the image viewing software. Accurate amplitude measurement (i.e., to within +/- 15%) was achieved using observed beam modulation amplitudes ranging 3-150 mm.

The initial results of the experiment proved confusing as all water and hexadecanol runs showed the higher damping constant indicating the presence of monolayer; no matter how vigorous the cleaning of the trough between measurements. It was only after the trough shape was modified to include an overflow point and water allowed to run into the trough and overflow into the sink for several hours before tests for clear water were carried out that a difference in the clean water and monolayer could be observed. It transpired that both Garrett & Zisman (1970) and Vines (1959)

also encountered similar problems and, indeed, came up with a similar design solution to overcome the extreme sensitivity of the clean water measurements to contamination by a monolayer.

The resultant decay constants δ for monolayer and clear water are shown in Figure 2.60. Also depicted in this graph are results obtained for hexadecanol from Goodrich (1962) using a cathetometer to physically measure wave height, and for water from Davies & Vose (1965) using the measured height at which a beam of light focussed by the troughs.

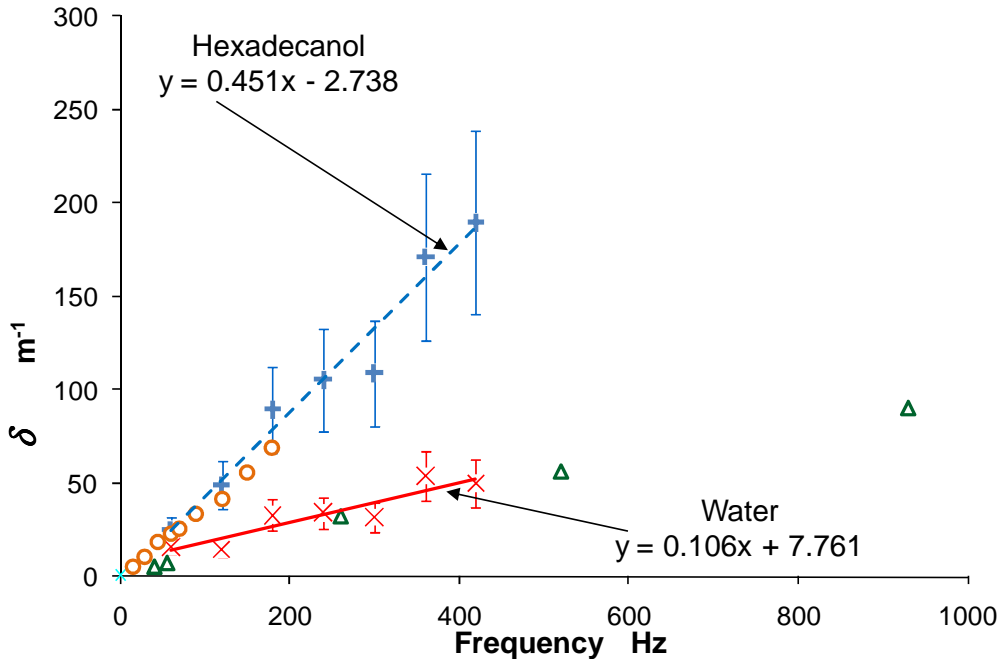


Figure 2.60 Measured decay constants for water (×) and hexadecanol (+) as a function of paddle frequency. For comparison, the results of Davies & Vose (1965b) (△) measuring clear water, and Goodrich (1981) (○) measuring hexadecanol are also plotted. Error bars of our experimental results are ± 1 sd.

Theory predicts a gentle bend in the decay constant plotted against frequency as predicted by Lamb's equation for surface damping, assuming a laterally immobile surface (Equation 2.33). The curve originates from the change in group velocity v_g with frequency. The data reviewed from other researches such as Goodrich (1962) and Vines (1959) show straight lines, and therefore curve fitting to straight lines will be used to simplify the interpretation.

The frequency gradient of δ for water in Figure 2.60 is 0.106 s m^{-1} , which compares favourably with the value from Vines' data (0.154 s m^{-1}) and the value quoted by Goodrich's empirical relation (Equation 2.30) of 0.113 s m^{-1} . The gradient for the hexadecanol results is 0.451 s m^{-1} , which is higher than Goodrich's value of 0.375 s m^{-1} . However it is evident from Figure 2.60 that Goodrich's data points follow the experimental trend line closely and that the gradient difference is primarily the result of the less-accurate experimental values acquired at higher frequency in this current work. Vines (1959) acquired a much higher value of $\delta = 0.749 \text{ s m}^{-1}$ but this was derived from only two frequency values.

The increase in magnitude of the error bars is indicative of the increasing difficulty in measuring the oscillation amplitude profiles. At higher frequencies the increased damping 'compresses' the distance out from the paddle over which waves can be monitored; the waves are dampened into extinction in a much smaller distance.

An alternative method of observing the wavelength can be found by laser scattering using a technique used by Miller (2003) and Lucassen (1968). Here the wavelength of the waves are directly observed by locating a photodiode at the zero-modulation point of the laser beam on the distant screen. The Lissajous figures in Figure 2.61 were created on an oscilloscope screen by connecting the x -axis (time-base input) to the voltage output of the photodiode and the y -axis to speaker amplifier. In Figure 2.61(a) the x and y -inputs of the oscilloscope are triggered to give an ‘in-phase’ signal whereby the particular point on the water surface and the paddle modulation frequency are set to be in phase. As the point of incidence of the laser beam is translated away from the paddle, the modulation signal of the laser beam and that of the paddle move out of phase (Figure 2.61(b) and (c)). Ultimately a translation value will be reached when the signals return to in-phase, corresponding to a translation of the point of incidence by $\lambda/2$ from the original laser incidence point (Figure 2.61 (d)).

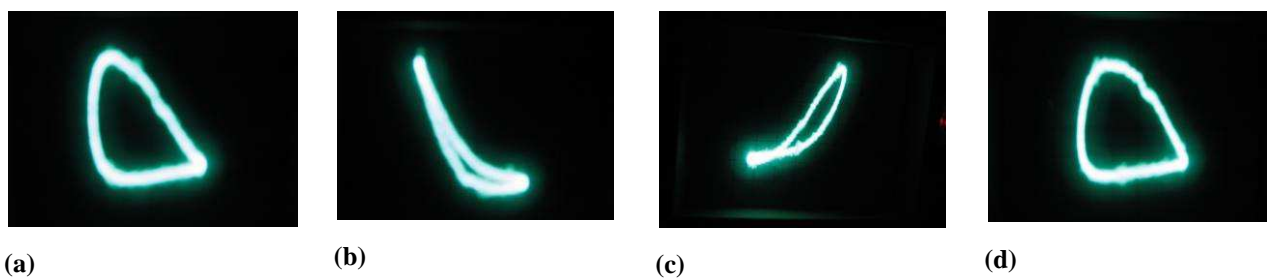


Figure 2.61 Lissajous figures derived by placing a photodiode at the location of the reflected laser beam incident on clear water. The x -axis of the oscilloscope trace is driven by the intensity modulation of the moving laser beam and the y -axis is driven by the sinusoidal current for the paddle amplifier. Phase difference between the two input signals, corresponding to translation of the laser’s point of incidence by a) 0, (b) $\lambda/8$, (c) $3\lambda/8$, and (d) $\lambda/2$ out from the paddle.

Irrespective of whether the amplitude or the relative phase of the beam oscillation on a distant screen is used to examine the waves on the water surface, the physical extent of the waves out from the single paddle, and subsequent contraction with increasing frequency limits the application of these techniques for monitoring of the decay constant for clean water and for water plus monolayer. Indeed the data of Figure 2.60 shows a frequency limit beyond which it was difficult to observe any waves whatsoever, at 420 Hz. Increasing the amplitude of the paddle modulation did provide an increase in the beam oscillation amplitude however it was found that overtones introduced by the speaker and mounting assembly degraded the water wave pattern and hence the oscillation pattern. In order to overcome this limitation, it is instructive to examine an alternative paddle construction that allow more effective coupling of paddle energy into the water. One method of efficiently coupling a disturbance from one oscillating medium into another is through resonance coupling, relying on the generation of standing waves in the latter medium.

2.6.3 Standing waves

The formation of standing waves in water depends on the propagation velocity of waves, which are determined by the surface tension and density of the fluid as predicted in Kelvin’s Equation (2.18).

Standing waves are particularly interesting for monolayer detection as there is a very distinct series of frequencies corresponding to the capillary wave velocity which supports the standing wave. The standing wave is easy to detect by the increase in wave amplitude, compared to nearby frequencies, and occurs when the distance available to the standing wave is equal to an integral number of wavelengths. Any change to the wave velocity produced by monolayers will change the conditions leading to a loss of conditions leading to standing wave, and therefore a lowering of wave amplitude.

This method has been used by Alexander (1985), who filed a patent in which a point wave generator to create circular waves in circular trough as shown in Figure 2.62(a) which, it was claimed could monitor or measure the surface tension of fluids automatically, using the frequencies corresponding to generated standing waves.

In this work a preliminary experiment using a point-source wave generator made from paper clip wire, resulted in the production of waves with no visibly perceptible amplitude, due to the small area in contact with the surrounding waver. The waves appeared near the pin, and were not large enough to reach the rim, so there was no possibility of observable standing waves. The length of excitation was increased by using a rim wave generator of diameter 72 mm (which was suggested in Alexander's patent) as depicted in Figure 2.62(b), and study the wave pattern inside. This resulted in observable standing waves, detectable by an increase in wave height inside the wave generator at some frequencies. However the circular waves behaved unpredictably in reflecting incident laser radiation. The circular waves meant the positioning of the laser affected the type of reflection strongly, moving the reflection pattern laterally and unpredictably. So although standing waves were now seen, the frequencies which led to them were not reliably found, and when a standing wave formed, the internal wave behaviour was too unpredictable. Sometimes the wave pattern showed as being elliptical with a double centre.

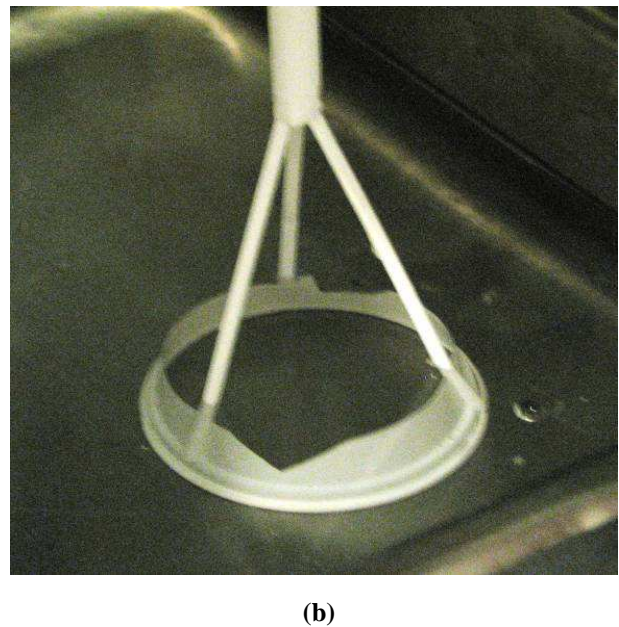
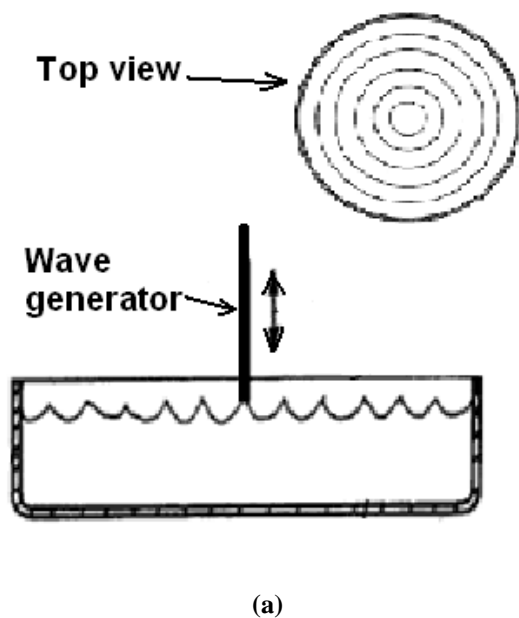


Figure 2.62(a) Standing waves generated from point wave generator. Adapted from the patent Alexander (1985) claiming automatic monitoring of surface tension. (b) Rim wave generator. A suggestion made by Alexander in

the patent application. It produced standing waves with much larger amplitude.

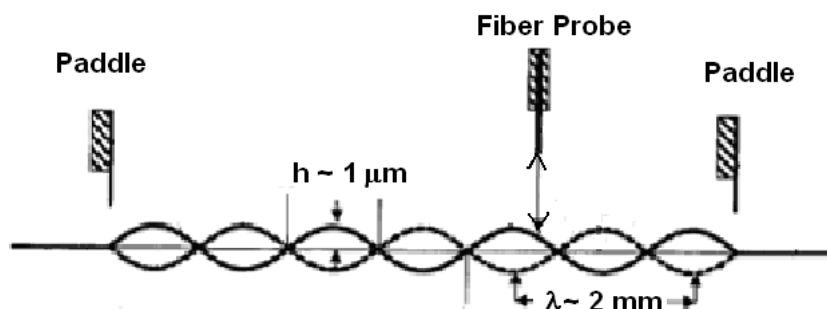


Figure 2.63 apparatus two paddle wave generators generating linear waves and a fibre optic sensor in between.
Adapted from Behroozi (2003)

A stable standing wave was produced between two plane wave generators by Behroozi (2003), as shown in Figure 2.64. An interferometer fibre probe used was used to measure wave height, and was also capable of translation so that it could accurately measure wavelength.

This type of standing wave detection was attempted. However, in order to make the system simpler, rather than using a fibre probe to detect wave amplitude, laser scattering was used. Also both paddles were attached to a single generator, so that they both have the same phase and amplitude. With a stable standing wave, the aim was to examine standing waves and wave decay that may show some signs of change with the addition of monolayer.

Materials and methods

Two solid polystyrene plane wave paddles, 0.23 mm thick and 53 mm long were joined 52.8 ± 2 mm apart on a plastic bridge, as depicted in Figure 2.64. A laser was directed at the region between the paddles at right angles to the paddles, parallel to the wave front, similar to the configuration described in Section 2.4.1. The trough was a stainless steel trough was filled to a depth of ~ 6 cm with tap water. Again, the incidence angle used for the laser was 74° . The amplitude was measured for the range of frequencies from 1-600 Hz.

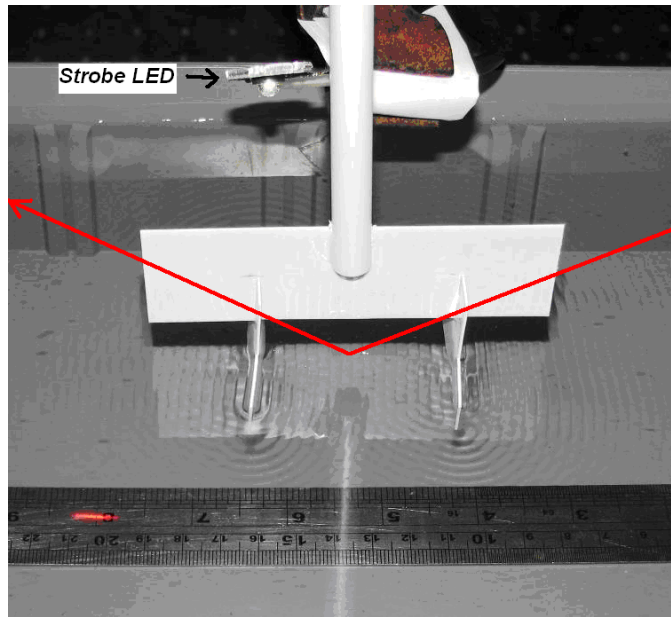


Figure 2.64 The double paddle in water with a laser reflected off the region midway between them. The transmitted laser can be seen reflecting on the ruler. This reflection was never seen to interfere with the reflection off the wave surface.

The wave amplitude was calculated from the amplitude of the beam oscillation using Equation 2.46 in Section 2.6.1. Measurements were obtained for both clear water and for full pressure hexadecanol.

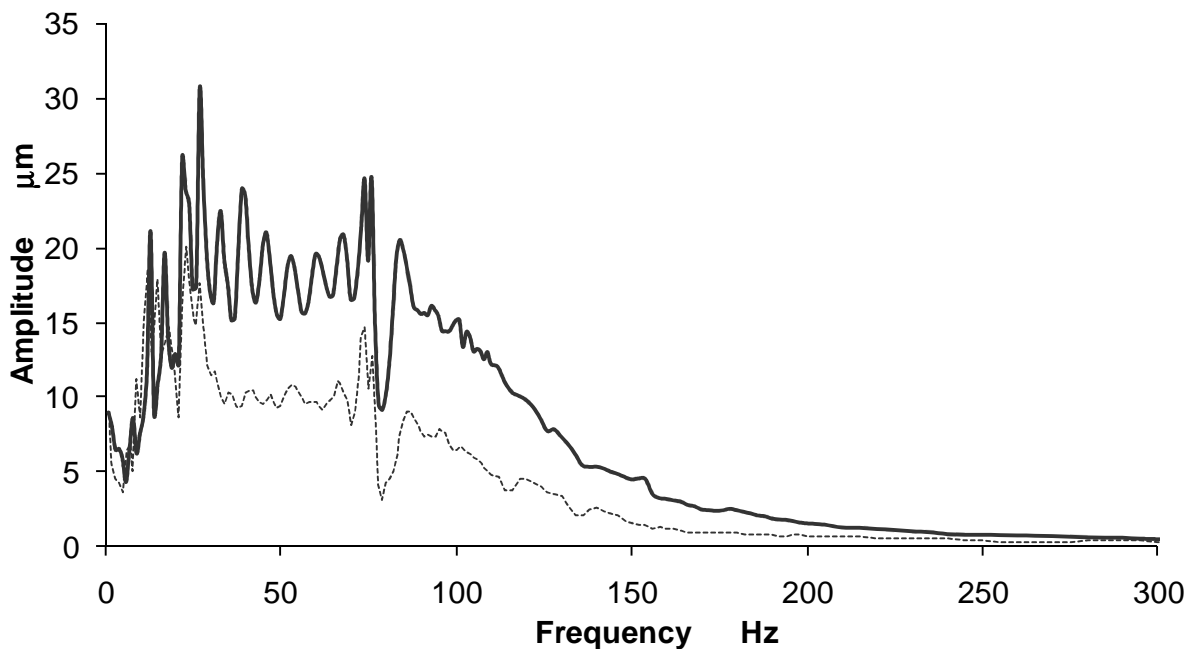


Figure 2.65 Amplitude of capillary waves as a function of paddle frequency for clear water (solid line) and hexadecanol monolayer (dotted line).

Results and discussion

The key features (Figure 2.65) are; a significant difference generally between the amplitudes of a clear water surface and hexadecanol surface, an exponential shape above 75 Hz and undulations caused by standing waves below 100 Hz.

Deficiencies exist, due to the gathering of data are shown below 20 Hz, where reflections from the end of the trough may have lowered the amplitude, and at 77 Hz, where a resonance was formed in the speaker stand, visibly interfering with the production of linear waves.

Amplitude difference and exponential decay at frequencies larger than 75 Hz

The decay in the amplitude with increasing frequency is most likely a combination of the visible contraction of the waves around the paddles due to damping effects as demonstrated in Figure 2.60 and the paddle/water coupling decreasing with increasing frequency. There is also a significant reduction in the amplitudes of the capillary waves between that of clean water compared to that of monolayer. This is particularly evident when the data are smoothed using a polynomial smoothing function of power 3 in the software program “Sigmaplot 10”. The smoothed data is shown in Figure 2.66. The maximum difference between the clear water and monolayer wave amplitude appears to occur around 100 Hz. The damping difference of course increases with amplitude, though the speaker translation reduces with frequency (see **Error! Reference source not found.**(b)).

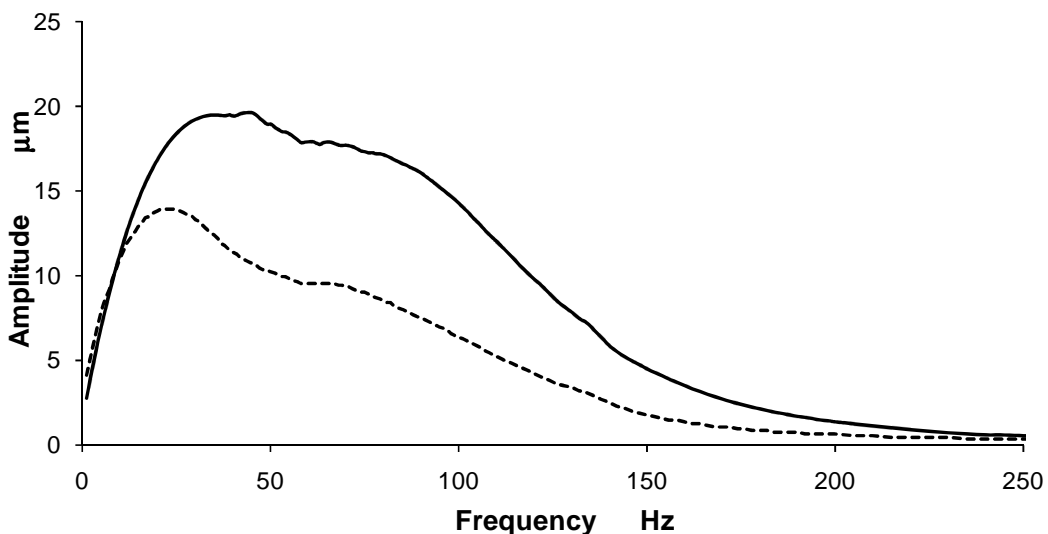


Figure 2.66. Smoothed amplitude-frequency curves for clean water (solid line) and hexadecanol monolayer (dashed line).

The speaker displacement function was determined using the reflection length of a He-Ne laser incident at 86° on a mm scale glued to the speaker. The initial wave measurements were taken at a setting value on the volume dial of 4, which was chosen to give a favourable length of reflection on the screen. The setting of 4 gave virtually no perceptible change in laser beam length, so the setting on the amplifier was increased so that if the shape of the normalized wave remains the same, it can fairly safely be assumed that it would be the same for the lower 4 setting. The larger settings that were chosen were 6, 8, 10 and 12 as these were values that the ruler could measure the full length of the slanted incident beam. The setup is photographed in Figure 2.67. The end of the He-Ne laser

can just be seen on the left side. The normalized results Figure 2.68 show that the frequency response of the speaker displacement is fairly consistent, for different amplitude settings and therefore should apply for the setting of 4 used. This shows that much of the decay of wave amplitude at higher frequencies would be due to a reduction in speaker translation distance. This would produce a smaller amplitude wave initially at the paddle even before the damping begins.

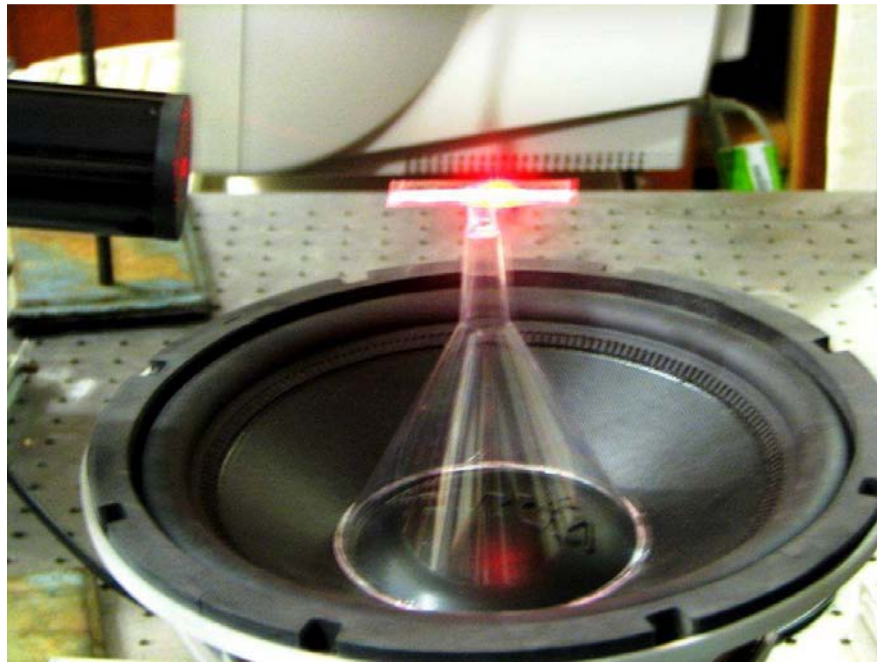


Figure 2.67 Inverted speaker with laser pattern length being measured on ruler.

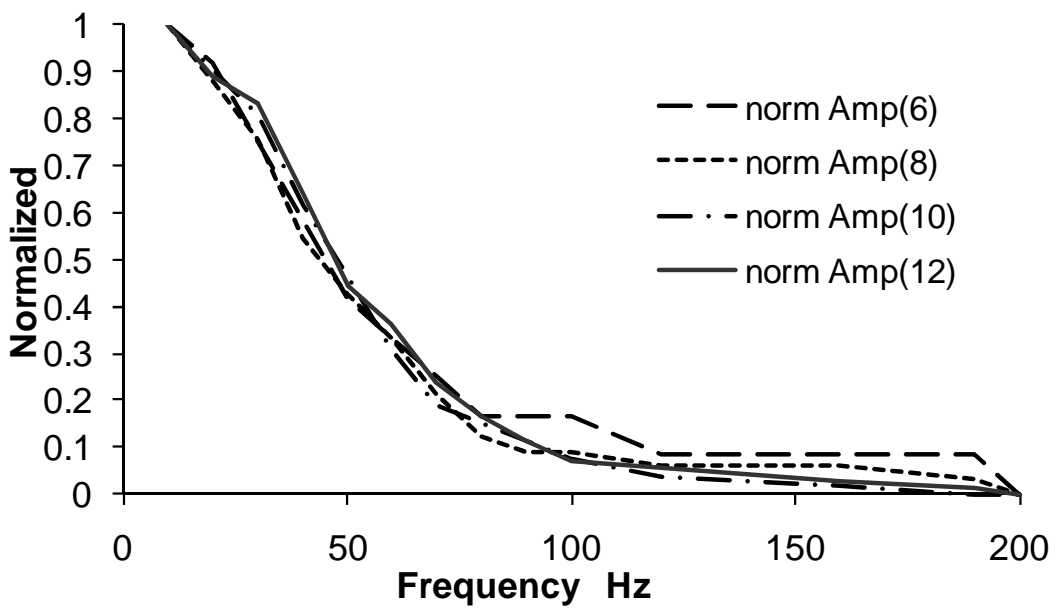


Figure 2.68 Results showing normalized displacement of cone at various settings of amplifier

Harmonics for frequencies less than 100 Hz

For each of the clean water and monolayer data there is an obvious plateau region in the frequency region 25-100 Hz which contains numerous regular undulations. These undulations at specific frequencies are the result of standing waves forming between the paddles, corresponding to an integer number of wavelengths. The first and second harmonics are shown in Figure 2.69.

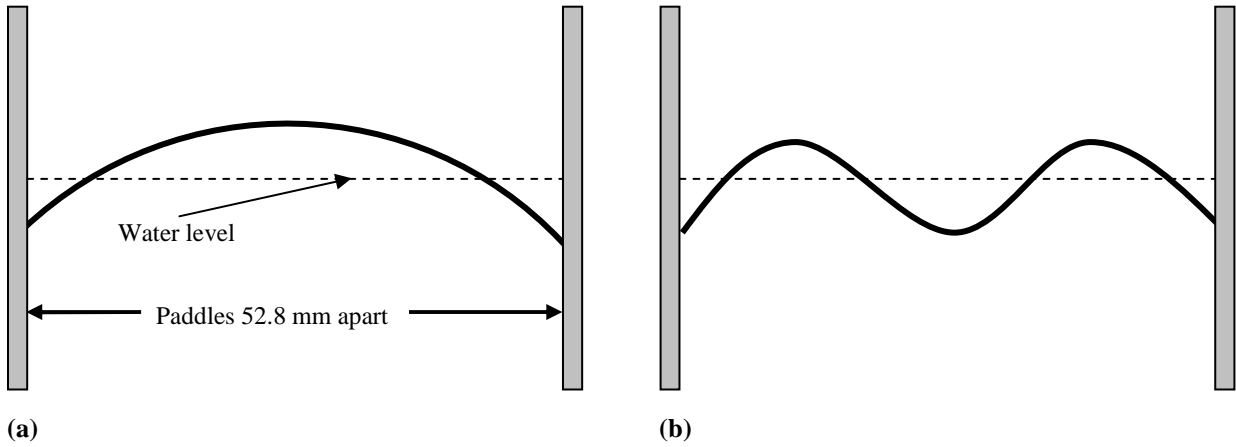


Figure 2.69 Two examples of standing waves generated between the plane-parallel paddles; (a) fundamental and (b) second overtone.

Experimental harmonic frequencies, taken from the maxima in Figure 2.65 are shown in Figure 2.70. The gradual curve in all the results is due to the velocity increasing with frequency for capillary waves (see Figure 2.9). The experimental values lie in between the theoretical harmonic frequencies for pure water at a surface tension of 72 mN m^{-1} (circles at harmonics) and theoretical values for $\frac{1}{2}$ of this value of surface tension (36 mN m^{-1}) (crosses with dotted line).

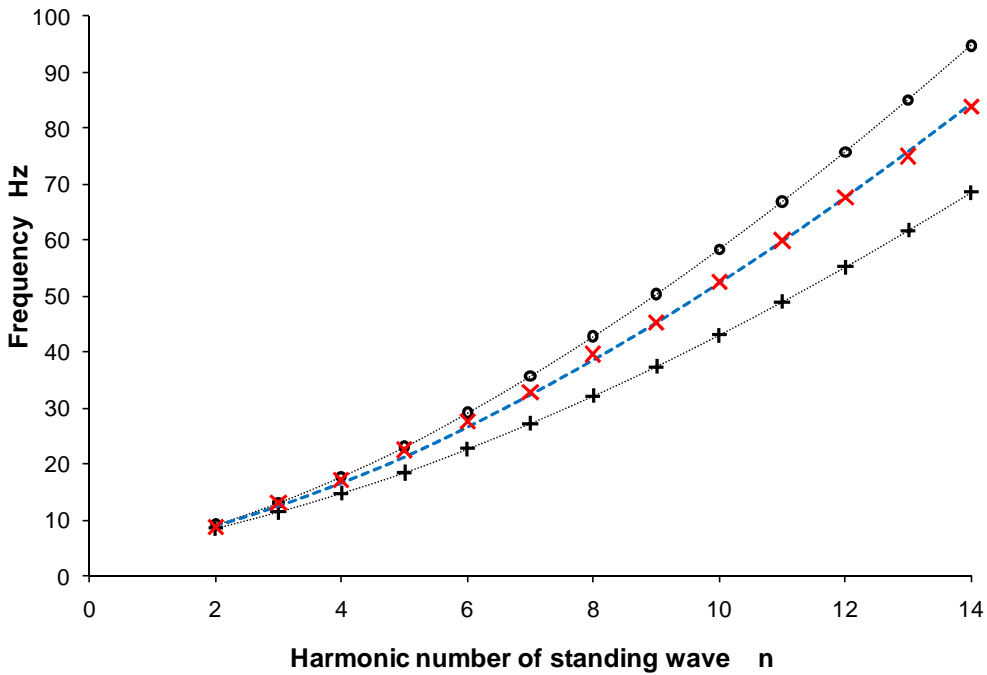
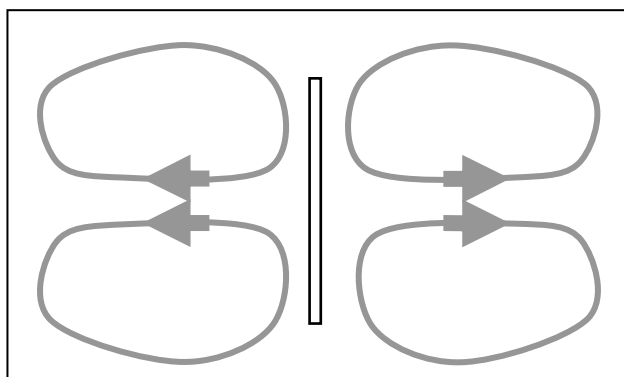


Figure 2.70 Experimental harmonic frequencies (×) compared to theoretical predictions at 72 mN m^{-1} (O) and 36 mN m^{-1} (+). A plotted theoretical value using a surface tension of 57 mN m^{-1} (blue dashed line) showing values close to those obtained.

A line of best fit has been superimposed over the experimental results which was found by trial and error curve fitting to best correspond to a theoretical surface tension of 57 mN m^{-1} . This was found by substituting various surface tensions into Kelvin's dispersion equation, to find the velocity which can then be used in the harmonic relationship. This indicates that tap water used had a surface tension of around this value. Another possibility leading to identical results would be an underestimation of the interpaddle distance by 10%. This is unlikely as the uncertainty of interpaddle distance was 4%. So this is proof that the tap water has a surface tension quite a bit below pure water, and that this tap water may be representative generally of the surface tension of water storages.

An interesting observation occurred when using much higher volume settings on the amplifier, of around 15. The single blade paddle was noticed to force the excess crystals of hexadecanol away from the centre of the paddle. The crystals then circled around and moved to the paddle ends to be again forced away by the centre of the paddle as shown in the diagram below. Vines (1959) makes mention of this effect, which he called "surface mass transport" and goes on to say that for films of low surface pressure, there would be an accumulation at the far end of a tank.

The swirling motion of these crystals showed the force from the paddle was not strong enough to push the monolayer completely away from the paddle. Even when this was occurring the monolayer appeared to swirl around and keep the area near the paddle reasonably covered, as assessed by observing the excess crystals floating on the surface.



2.47 Motion of hexadecanol crystals from a blade paddle with large amplitude.

2.7 Conclusion

Using surface tension as a monolayer indicator shows most contrast when the water surface has a value close to pure water. It was found by using wave velocity measurements and standing waves frequencies, that tap water at UNE, Armidale, fairly typical of water storage surface tension (Pers. comm. Pam Pittaway 2011) possessed a reduced surface tension. It may even happen that in some water bodies the surface tension is reduced to such an extent that monolayer will not spread.

With improved techniques and higher precision equipment both the measurement of wave speed using the graduated scale, and diffraction techniques could be successful for water with an initially high surface tension. The aim of this work however, is to develop techniques for relatively uncontrolled field conditions and in this respect, these techniques were not found useful.

Monitoring the damping of artificially generated waves provided a more reliable method as the damping is a result mainly of increased surface viscosity. However the optimal positioning of the incident laser, was unpredictable and every set of measurements needed adjustment of the laser to discover the ideal incident position of the laser away from the paddle, to obtain an exponential decay curve. So in the field there would be alignment and particularly automation problems.

The standing wave formed between parallel paddles showed an interesting way of measuring surface tension, and shows promise as a laboratory based non-contact method of measuring surface tension, however would require controlled conditions and precision equipment.

The surface of water storages is difficult to stabilize due to variations in height and waves. Methods which do not rely on maintaining a still surface, such as remote and temperature measurements, could offer more robustness and versatility.

Chapter 3. Contact temperature measurements

Evaporation occurring at the surface of water creates a latent energy heat sink, as the molecules with the highest energy vaporise and are lost to the surface, resulting in a lowered average temperature of the remaining water molecules. The existence of a cool skin layer was first noted in Russia in the Neva river by Altberg and Popov in 1934 (Gladyshev 2002). They were surprised to find that small thermistors placed in the top 2 mm showed a measurement of 0.5 °C cooler compared to deeper water. Remote infrared (IR) and contact temperature measurements have since been combined to determine that under typical conditions a clear water body forms a cool skin on the surface mostly due to the effect of evaporation and IR radiation from the water surface (Mobasheri 2006).

The evaporation-reducing effects of monolayers lead to a reduced latent heat drain at the surface, which would be expected to increase surface water temperature. Measurement of vertical temperature profiles, within water near the surface, may represent a very direct way of assessing evaporation. This chapter examines existing knowledge of heat fluxes, and how changes in processes that occur with the addition of monolayers alter the temperature profile. A temperature-dependent detection method would necessarily need to utilize spatial differences, or temporal changes of temperature which occur with the addition of monolayer, due to the difficulty in predicting the absolute surface temperature based on climatic factors (see Section 4.5.3).

3.1.1 Comparisons between contact and remote IR methods of measuring temperature

Measurement of water temperature under the water surface often uses either thermistors or thermocouples. Thermistors are made from a resistor whose resistance is accurately known, and calibrated, against its temperature. A thermocouple is a device that encapsulates the electrical junction between two dissimilar metals, and the thermoelectric effect, which results in the creation of a small (mV), temperature-dependent, potential difference between the two metals. This is accurately known, and calibrated for the temperature of the junction relative to a reference junction usually held at ambient temperature. Both thermistors and thermocouples can be fabricated quite small, with volumes $\leq 1 \text{ mm}^3$ (Gladyshev 2002:7).

Sensor size is critical to the accurate determination of the near-surface temperature profile as it determines not only the 'sensing volume', but also the thermal inertia of the sensor itself. Moreover the bulk of the sensor may influence miniature heat fluxes in their vicinity leading to an altered temperature reading. Before the existence of IR thermometers in the 1950's it was not possible to know whether invasive contact probes such as thermistors and thermocouples actually measured a real cooling at the surface (cool skin), or some imaginary temperature (Gladyshev 2002:6). The lack of precision in measuring temperature using contact methods near an often unstable surface is complicated by a steep temperature gradient which usually exists, greater than any other part of water storages, at around 0.5 °C across the top several mm depths. Even when a thermistor is placed

at the surface, IR radiometer measurements still provide lower values. Eagleton (1965) used simultaneous IR and thermistor laboratory measurements and found IR temperature values were 0.2-0.5 °C lower. This is despite the thermistor being very small; 0.25 mm in diameter, and placed $\frac{1}{3}$ below the flat surface and $\frac{2}{3}$ above the surface covered by the meniscus (Gladyshev 2002).

In the case of laboratory troughs, an estimate of the surface temperature was made by Langmuir and Schaefer (1943), by immersing a mercury thermometer at a depth of 5 mm. The surface cooling temperature was found to be 1 $\frac{1}{2}$ times the deviation from the bulk temperature. Archer & La Mer (1955) found that under laboratory conditions the surface temperature could be estimated to within 1.0 °C by extrapolating the temperature from two thermometers; one placed at the bottom of the trough, and the other just below the surface.

A comparison of airborne radiometer measurements with direct methods at a depth of 1.0 cm for clean water on lake Hefner, Oklahoma, made by Grossman, Bean & Marlatt (1969) found IR thermometer radiometer measurements consistently gave a reading 0.4-0.9 °C below the contact measurements. Ewing & McAlister's (1960) found IR radiometer measurements indicated the ocean surface is up to 0.6 °C cooler than thermistor measurements. Katsaros (1980) measured this figure as 0.5 °C. Handler, Smith, & Leighton (2000) state that in open sea water, the skin layer for the open oceans is 0.1-0.5 °C lower than the bulk. Mobashi (2006) sums up the findings of many authors stating that this value varies from 0.1-1.2 °C for oceans. These are only typical measurements however, as Gladyshev (2002) has noted that while the skin (defined in Section 3.1.3) is usually cooler, for around 85% of oceans and lakes tested, in some conditions, such as warm air and high humidity, a warmer skin forms.

3.1.2 Surface Heat fluxes

The vertical profiles of temperature immediately above and below the surface of an open water body are the result of a number of heat flux mechanisms that occur at the surface and beneath the surface within the water. For the purposes of the ensuing discussion, *surface fluxes* describe the transfer of heat across the air-water interface, while *water fluxes* are those that operate exclusively within the volume of water.

If edge effects are ignored, and there are no flows of water into or out of the storage, the surface fluxes can be summarized as shown in Figure 3.1(a). They comprise latent heat of vaporization, solar irradiance, atmospheric radiation, sensible heat flux, and the emission of surface radiation.

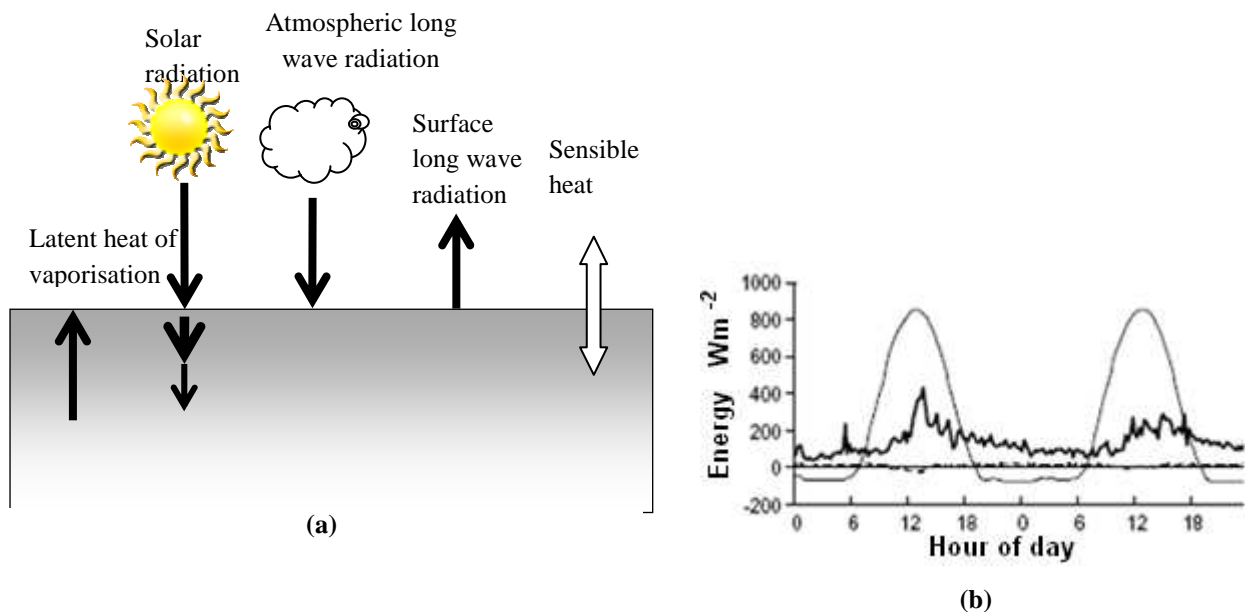


Figure 3.1(a) Typical surface heat fluxes occurring in large water storages. Adapted from Marlatt and Grossman (1968). (b) Relative magnitude of the main surface fluxes operating on a typical small water storage surface. Solar flux; light grey, latent heat flux, black, sensible heat flux; dashed. Source; Tanny *et al.* (2008).

Latent heat of vaporization

As water molecules vaporise from the water surface they absorb energy associated with the latent heat of vaporization L ($=334 \text{ kJ kg}^{-1}$). As the process of evaporation involves the loss of the molecules with the greatest thermal energy from the surface, a heat sink is formed, which is mostly replenished by heat fluxes from bulk water (Barnes & Hunter 1982:48). Methods of estimating the magnitude of water evaporation such as the Penman-Monteith Equation (1.15) require a careful analysis/estimation of the amount of heat available for evaporation. As can be seen in Figure 3.1(b) the highest evaporation rate occurs around the warmest part of the day.

Incident solar radiation

Incident solar radiation on a water surface may be reflected or transmitted according to the Fresnel equations (Section 4.2.1). That portion of radiation that crosses the air-water interface will be transmitted into the bulk volume of water to a depth according to the wavelength dependent transmission characteristics of the water (Campbell 1996). Some of this will be scattered and reflected within the water body (*volume reflection*), and some of this scattered radiation re-emerges as *underlight* back into the atmosphere. Rayleigh scattering by water particles that are small relative to the wavelength favours shorter wavelength radiation resulting in the characteristic blue or blue-green colour. Figure 3.2 depicts the absorption coefficient and effective optical depth of radiation in water.

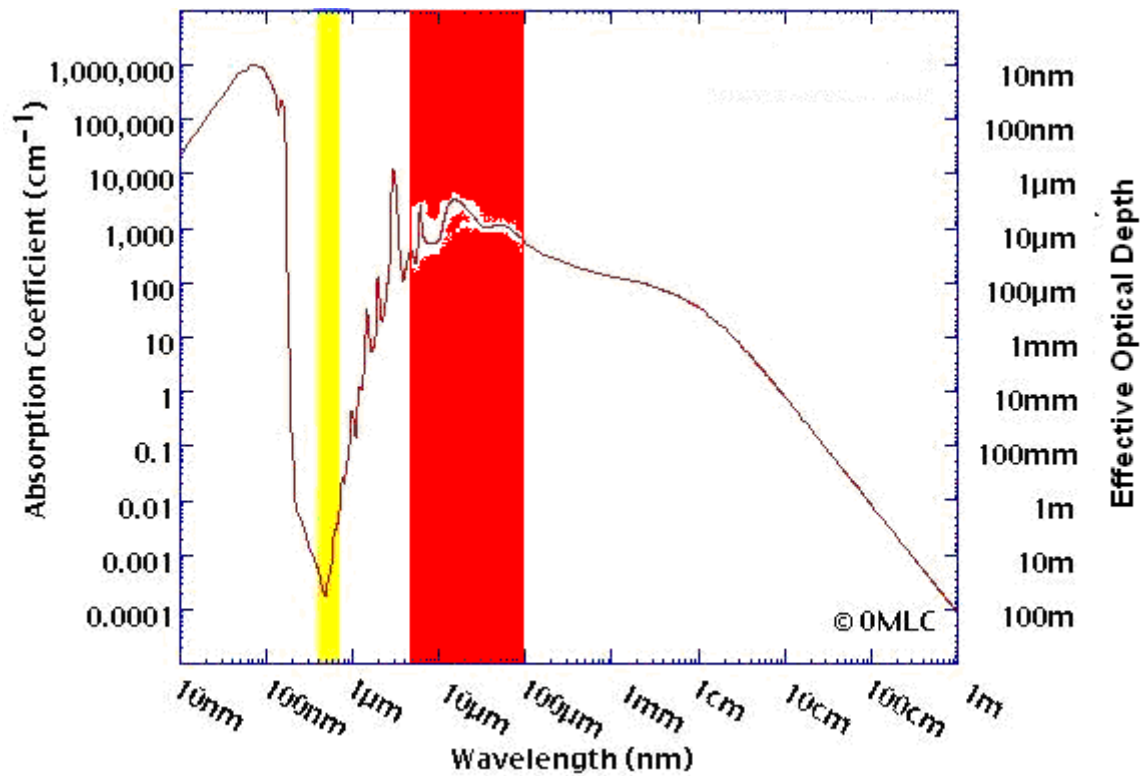


Figure 3.2 Absorption of radiation by water. The yellow bar indicates visible solar radiation (0.3-0.7 μm), while the red bar indicates atmospheric long wave radiation (4-100 μm). Adapted from Segelstein (1981).

The right side vertical axis represents the *effective optical depth*, which is the depth within a material at which the intensity of the radiation inside the material falls to 1/e (about 37%) of the original value at the surface. The left hand side vertical axis is the inverse of effective optical depth called the *absorption coefficient*; the inverse of effective optical depth.

The intensity of radiation penetrating a substance declines exponentially with distance (Jiles 2001) according to:

$$I = I_0 e^{\frac{-z}{\tau}} = I_0 e^{-\alpha z} \quad (3.1)$$

where I is the intensity of radiation at depth within the material, I_0 is the incident radiation, τ is the effective optical depth, α is the absorption coefficient and z is the depth below the surface. The effective optical depth is defined as the depth at which the intensity of the radiation reduces to 1/e (37%) of the original value at the surface. The absorption coefficient represents the inverse of effective optical depth.

As a consequence of its relatively deep penetration, solar radiation has very little effect on the temperature near the surface, with only around 15% of the total sun absorbed in the top few mm (Katsaros 1980). The effect of sunlight at a depth of 10 cm on a cigar-sized thermistor positioned 10 cm below the surface was investigated by Kurzeja & Pendergast (2002) on a lake on the Savannah River, South Carolina, USA. The thermistor was alternately exposed to noon sunlight and shaded for several minutes. The results showed only a 0.1 $^{\circ}\text{C}$ increase in thermistor temperature with exposure to sunlight. The maximum effect of sunlight at solar noon with only a light breeze was estimated at 0.3 $^{\circ}\text{C}$.

Solar radiation penetrating down to a few metres produces a “diurnal warm layer” which is a layer of warm water heated by solar radiation which convects towards the skin layer. The diurnal warm layer needs to be allowed for estimating bulk temperature based on radiometric measurements (Gentemann & Minnett 2008) as measurements performed during the day could overestimate the bulk temperature by as much as 3°C (Yokoyama 1991)

Water bodies which have impurities, such as sediment, are termed turbid and have slightly different spectral properties (Kirk, 1994). The existence of sediment in the water increases volume reflection, and shifts the maximum transmittance window to higher wavelengths, towards the green wavelength region of the spectrum. The transmittance window also widens so that determination of colour is more difficult, and the water appears brighter (Campbell 1996).

Incident atmospheric long wave radiation

Long wave radiation is reflected/emitted by greenhouse gases in the atmosphere, such as carbon dioxide and water vapour. Clouds have the effect of lowering the direct short wave solar radiation, and increasing long wave infrared radiation, thereby increasing the *greenhouse effect* (Ahrens 2007:40). They increase solar global albedo (reflection) by 25% (Campbell 1996), absorb 5% of solar radiation and diffuse 14% downwards to be absorbed by the Earth’s surface in the form of long wave radiation (Byrant 1997) in the IR region of 4-100 μm (BoM 2010). On average, around 45% of short wave solar radiation reaches the ground (Campbell 1996) through clouds. The alteration to effective optical depth of water due to the change in wavelength produced by clouds is shown in Figure 3.2. Whereas the solar radiation (yellow band) has an effective optical depth in the order of metres, the long wave radiation (red band) produced by the atmosphere and clouds are absorbed entirely at the surface with an effective optical depth of the order of tens of μm .

Clouds then, have the effect of delivering more energy to the surface, and less to depths, while at the same time being associated with an increase in humidity, thus lowering evaporation. In addition there is also a moderation of temperatures exists with cooler days and warmer nights (Gabler, Petersen, & Trapasso 2007).

Surface long wave radiation

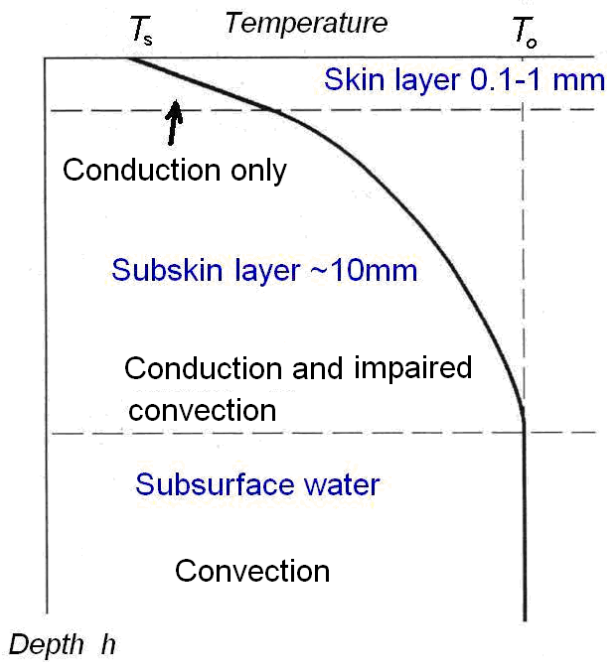
The emission of radiation from the water surface, described by the Stefan-Boltzman equation (Equation 4.5) is dependent on the temperature of the surface and has a maximum in the infrared region at around 10 μm for a water temperature of 20°. Around this wavelength the effective optical depth is 10-20 μm (Figure 4.26), with the maximum depth being sampled using an IR thermometer in the 8-12 μm region is 25 μm (Saylor, Smith, & Flack 2000). Radiance calculations show that a change in surface temperature by a single °C produced by the evaporation reduction of monolayers increases the radiated energy by more than 3% (see Section 4.1.1).

Sensible heat flux

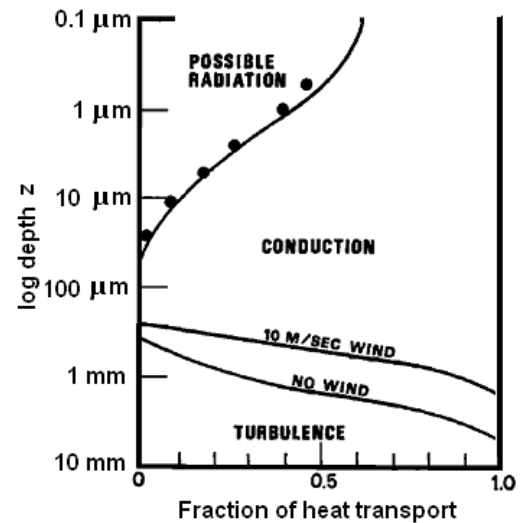
The flux of energy that results from a temperature difference between water and its surroundings, which is not contributing to a change of phase is known as sensible heat flux (American Meteorology Society 2009). So sensible heat fluxes are reactive heat fluxes in which the temperature of a warmer body is assuming equilibrium with its immediate surroundings which include conduction, convection and radiation. In the situation of water storage surfaces; sensible heat fluxes are energy exchanges between the water and adjacent air, which do not include latent heat, or distant sources of radiation such as the sun and clouds.

3.1.3 Water heat fluxes

The greater the rate of evaporation occurring, the cooler the surface becomes. An equilibrium temperature distribution within the water column will be reached where the heat lost by evaporation at the surface is just balanced by the heat gained from the surroundings (Jarvis 1962). There are two processes which transfer heat to the surface in water from within the water body. **Conduction** is the transfer of heat along a temperature gradient from higher temperature to lower (Gates 1980:268), which does not involve a net movement of molecules. **Convection** involves the transfer of heat within a fluid by the relative motion of warmer and cooler parts of the fluid (Penny 1945). The equilibrium vertical temperature gradient beneath the surface of a water body is the net result of the main vertical heat flux mechanisms. Under typical conditions, there is an upward-directed heat flux within the upper part of the water column supplying the cool, higher density surface with heat from lower levels. To visualize the connection between the heat flux, and temperature gradient, the situation can be compared to electricity. The electrical current along a simple, single circuit loop (heat flux) is the same at all points along the loop, and the voltage drop (temperature) is steeper across areas of higher resistance. Thus, the temperature gradient is proportional to the heat flux resistance. In order to discuss the near-surface heat fluxes within a water column, a brief discussion of the vertical 'structure' of the near-surface water column is necessary. The near-surface zone is differentiated into three distinct layers according to the dominant heat transference process (Donlon *et al.* 2002; Gladyshev 2002; Mobasher 2006) as depicted in Figure 3.3(a). These layers are the skin, subskin and subsurface.



(a)



(b)

Figure 3.3(a) A typical open water temperature profile with the layers divided according to the dominant process of heat flux occurring. T_s indicates surface temperature, while T_o indicates subsurface temperature, which implies a depth fairly close to the surface ($<10\text{cm}$). Adapted from Gladyshev (2002). (b) The fraction of heat transfer in the top mm on the ocean. Source; McAlister & McLeish (1969).

As depicted in Figure 3.3(a) the *skin* is the most superficial layer with a thickness δ 0.1–1.0 mm for large lakes and oceans and larger for small contained areas. It contains a latent heat sink at the surface, along with a sensible heat flux component. Atmospheric IR radiation absorption and surface radiation affects the top 25 μm ((Saylor 2002)) with the effective optical depth of 10- 20 μm at an IR wavelength of 10 μm using Figure 4.26. This is the depth averaged by IR thermometers which usually operate in the 8-12 μm range. Therefore IR thermometers are the most convenient way of determining the skin temperature.

The skin layer has a higher viscosity due to its proximity to the surface in which molecular forces dominate, making molecular conduction the dominant mechanism of heat transfer (Gentemann & Minnett 2008; Volino & Smith 1999)

A comparison of the fraction of heat transport at various depths is shown in Figure 3.3(b). The skin layer depth is depicted in this figure by the radiation and conduction area, down to a depth where determined by the prevailing wind conditions.

The dominance of conduction in this layer was demonstrated by Andreev, Gurov, & Khundzhua (1976), who made direct measurements of skin layer temperatures using microthermocouples. They found the temperature gradient within the layer was linear, and the coefficient of conductivity across this layer was calculated to be $0.58 \pm 0.06 \text{ W m}^{-1}\text{C}^{-1}$. This is identical to the tabulated value at 20°C of $0.581 \text{ W m}^{-1}\text{C}^{-1}$ (Kaye & Laby 1973) for the molecular conductivity of water, indicating

there is only conductive transport of heat across the skin. Since conduction is less efficient in transferring heat than convection, this “insulating boundary layer” (Hasse 1971; Saunders 1967) impedes the upward heat flux, making the skin a layer of increased heat flux resistance. When this resistance characteristic is combined with a liberation of heat by latent, sensible and radiative heat processes at the surface (Handler, Smith, & Leighton 2000), this layer usually contains the steepest temperature gradient of any depth within the storage (Barnes & Feher 1980).

The next layer under the skin is the *subskin layer*, where density induced convective heat transfer processes begin to dominate. It usually has a thickness of around 1 cm, and convection thermals begin in the upper part of this layer. The temperature accordingly varies on a scale of minutes due to thermals, and the temperature profile is exponential (Gladyshev 2002).

The *subsurface layer* is considered to be that where the temperature characteristics reflect the ‘true bulk temperature’ of the water body. In practice the depth of the upper reaches of this layer is chosen to be deep enough to avoid the exponential subskin profile and surface roughness effects, and shallow enough for the large scale temperature gradient which extends to the bottom to begin to be observed. For open water bodies, with no surface waves this is typically a few cm beneath the surface. However it should be noted that during the day, the top few metres of open water is warmed by solar radiation forming a “diurnal warm layer” which is a layer of warm water heated by solar radiation convecting towards the skin layer. This diurnal warm layer needs to be allowed for estimating bulk temperature based on radiometric and ΔT_S temperatures (Gentemann & Minnett 2008). Measurements performed during the day on the skin zone during the day could overestimate the bulk temperature. At subsurface depths this diurnal heating cycle may produce a variation by as much as 3°C (Yokoyama 1991).

Allowing for the effect of the diurnal heating, the subsurface layer temperature is ascribed ‘bulk’ or ‘volume’ temperature of a water body. The temperature however, is always a function of depth, and the function is very difficult to predict as it depends on many heat fluxes, and hydrodynamic properties of the water body. Generally authors state the “bulk temperature” at a certain depth, to allow changes with depth. Often ocean temperatures are measured at a depth of 10 m because this is around the depth of water inlets on large ships, which are continually monitored for engineering purposes in any case (Donlon *et al.* 2002). This layer is represented in Figure 3.3(b) under the ambient wind condition line.

3.2 Characteristics of the skin

As mentioned previously, owing to the dominance of molecular conduction, the skin is a fairly stable layer which “rides over deeper turbulent convection currents” (Gentemann & Minnett 2008). The layer is generally detected by measuring the temperature gradient just under the surface (Grassl 1976). If it is disturbed by breaking waves, wind speeds exceeding 10 m s⁻¹ or rain (Grassl 1976), mixing the skin layer with lower layers, it will reform in around 10–12 seconds (Clauss 1970; Ewing & McAlister 1960). The reformation time has been investigated more thoroughly by Mobasher (2006), who found that the reformation time is highly variable, depending on both water temperature and wind speed. He found that; at a low temperature of 10 °C and low wind speed < 5.5 m s⁻¹ the reformation time is around 50 seconds, whereas at a higher temperature of 30 °C and high wind speed 10 m s⁻¹ the reformation time reduces to 1 second.

Using simultaneous IR photography and underlying velocity measurements Volino & Smith (1999) found that a cycle of varying thickness occurs in the skin layer. As cooling occurs at the surface, the skin thickness increases until it becomes unstable with respect to the warmer subskin water. A cold thermal is initiated in the subskin zone (Katsaros 1980) in which a plunging sheet forms which drains the cool water downwards, instantly reducing the skin thickness. Once this is complete the cooling at the surface again starts the cycle of increasing the skin layer thickness again.

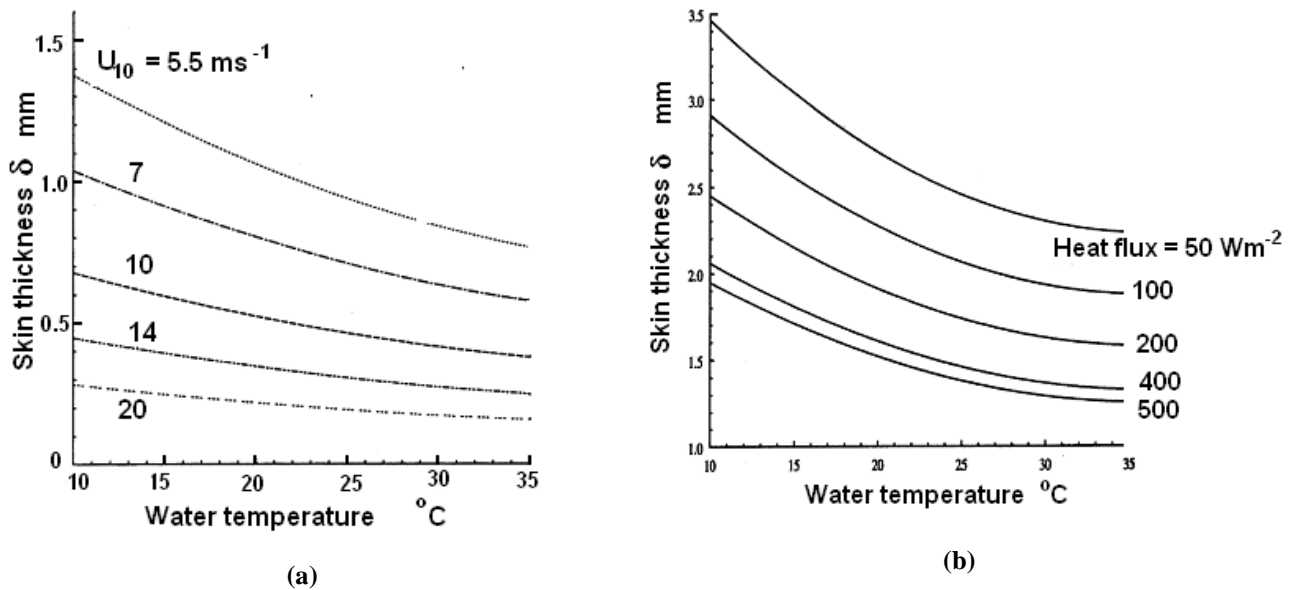


Figure 3.4(a) Theoretical variation of skin thickness with water temperature and wind speed. (b) Theoretical variation of skin thickness with total heat loss. Adapted from Mobasheri (2006).

3.2.1 Skin thickness δ

The main factors affecting the thickness of the skin layer are wind speed, bulk water temperature and heat flux. Figure 3.4 was produced from theoretical considerations by Mobasheri (2006) and depicts the effects of these three factors on skin thickness. The effect of wind is depicted in Figure 3.4(a) showing the effect of generated turbulence mixing the surface and decreasing the skin thickness. A similar decrease in skin thickness has been determined in data gathered by Gladyshev (2002:15). The effect of increasing temperature decreases the viscosity of water, increasing the subsurface convection currents and decreasing the skin thickness. This is shown on the x axis of both graphs. The effects of increasing the heat flux on skin thickness as shown in Figure 3.4(b), also decreases the skin thickness by increasing the activity of the convection currents.

Warm skin conditions change the skin thickness dramatically as the cold thermals cease. The warmer temperature lower density water at the top increases the skin thickness as it is now stable and has little temperature fluctuation. The thickness of the skin in this situation increases to around 10 mm, with the sub skin increasing to around 50-70 mm (Gladyshev 2002:19). Thus the heat flux through a warm skin is believed to be lower because of the thicker conduction zone.

The thickness is determined by the viscous shear stress transmitted by the wind to the water, and also by the viscosity (Mobasher 2006), and therefore would be expected to increase with addition of surface active layers due to an increase in viscosity and decrease in surface stress and turbulence (see Chapter 5). It might also be expected that sampling water in tubes, as will be carried out in this work, would increase the skin thickness due to decreased turbulence caused by close proximity to the walls and lower horizontal wind speed.

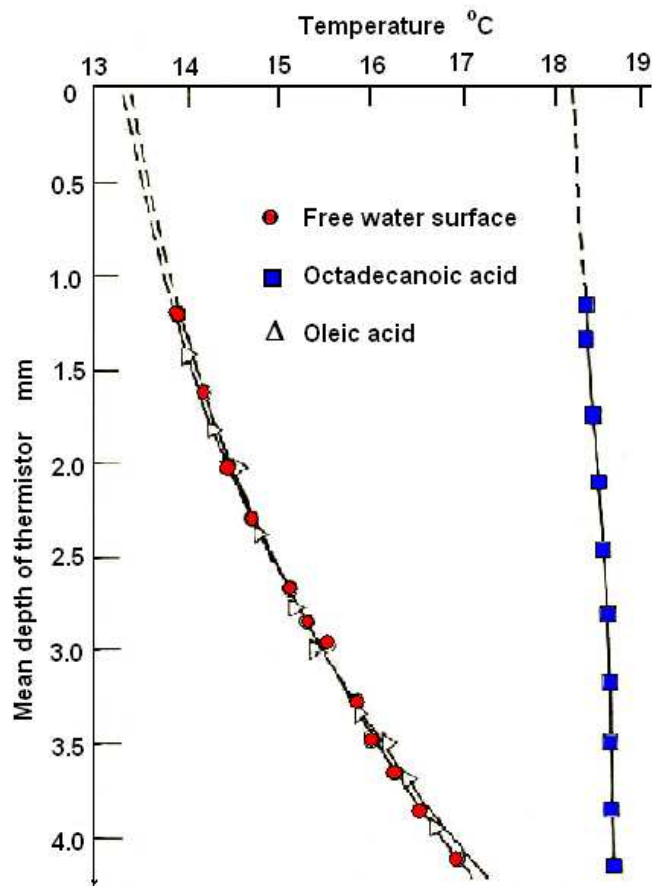


Figure 3.5 Temperature profiles of free water; ●, oleic acid; ▽, and; octadecanoic acid; ■. Adapted from Jarvis, Timmons, & Zisman (1962).

3.2.2 Skin temperature

Thermistors and thermocouples are problematic at the surface, however they can measure the temperature profile at depth, and this can be extrapolated back to the surface to obtain surface temperature. This was carried out by Jarvis, Timmons, & Zisman (1962). In an enclosed chamber, with a slight wind of dry nitrogen gas, they extrapolated the temperature from a thermistor array to obtain surface temperature and change in surface temperature resulting from the addition of monolayers. The surface temperature was found to increase by up to 7 °C with the addition of octadecanoic acid compared to a clear water surface, as shown in Figure 3.5.

The octadecanoic temperature profile, shows little reduction in temperature approaching the surface due to its evaporation reducing effects. Also shown is the temperature profile of oleic acid monolayer, which has little effect on evaporation, and therefore shows is a very similar profile to clear water.

An array of thermocouples was also used by Navon and Fenn (1971) in a temperature-controlled chamber, who similarly measured the change in temperature profile that occurs with the addition of a monolayers with an array of thermocouples. They found a surface temperature ~ 1.5 °C warmer with the addition of hexadecanol.

Differences in surface temperature as measured with thermistors have been found by Gladyshev (2002:49) to be influenced by sensible heat transfer due to the difference between air temperature and water temperature (T_{AW}), and also the humidity in the air.

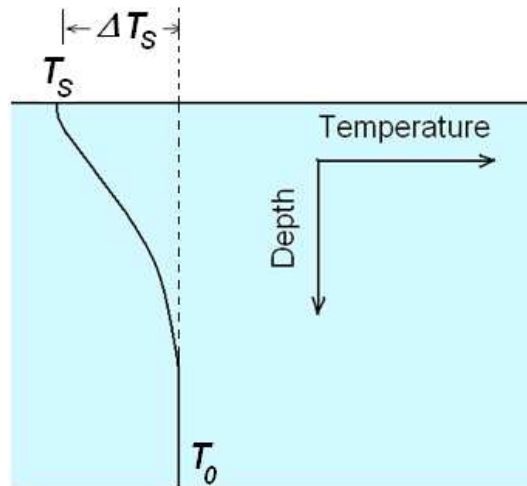


Figure 3.6 Surface deviation temperature.

A useful definition used by Hasse (1971) to determine whether the skin layer is cool or warm is called the *surface deviation temperature* ΔT_s . It measures the temperature of the surface skin relative to the subsurface as follows:

$$\Delta T_s = T_s - T_0 \quad (3.2)$$

where T_s is the temperature of the surface, T_0 is the temperature below the surface gradient, in the subsurface layer. The difference is depicted in Figure 3.6. So a negative ΔT_s indicates a cool skin and a positive value indicates a warm skin.

3.2.3 Predicting Surface Deviation temperature ΔT_s

The ΔT_s can be determined by measuring the heat fluxes near the surface or by using physical temperature sensors. A heat flux method described by Gladyshev (2002) involves accounting for all the heat fluxes passing through a particular depth h . ΔT_s is usually negative for a cool skin, however it can also be positive; indicating a warm skin. The temperature depression can be related to heat fluxes as follows:

$$\Delta T_s = -\frac{h}{H_h}(R + P + LE) \quad (3.3)$$

where h is the depth at which T_0 is measured, H_h is the average heat transfer in the layer at depth h , R is the radiative heat flux from water surface, P is the sensible heat flux processes into the air, L is the latent heat of evaporation, E is the rate of evaporation, with all these fluxes being measured in Wm^{-2} .

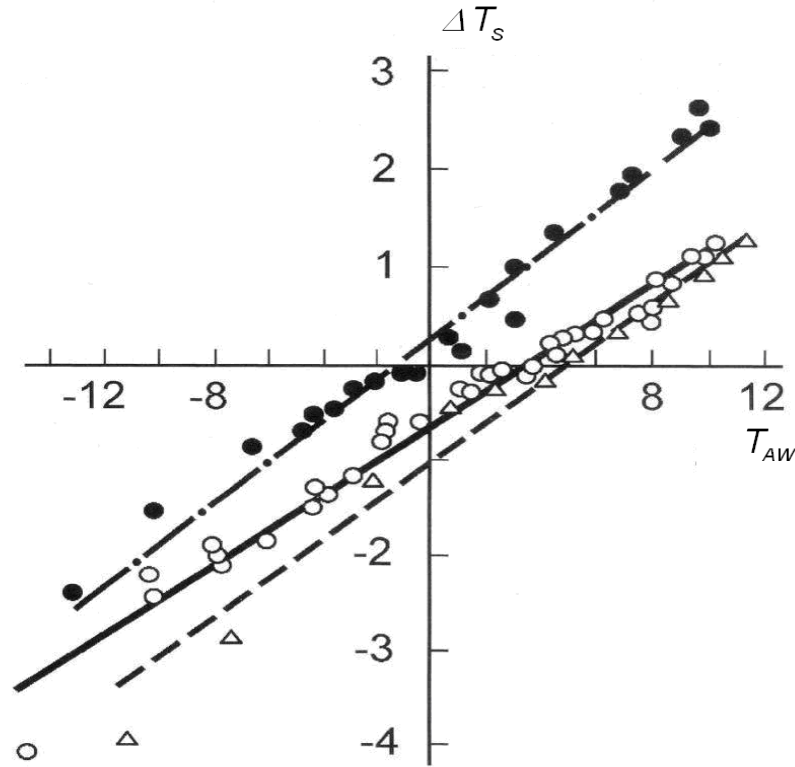


Figure 3.7 Surface temperature deviation ΔT_s at various air water temperature differences. Adapted from Gladyshev (1988). The plots show different relative humidity conditions. Data series 88%; ●, 21%; ○, and 15%; Δ .

The linearity of ΔT_s with respect to T_{AW} is confirmed by results in Figure 3.7 measured by Gladyshev (1988) in a small trough under controlled conditions for three different humidity conditions. The gradients were measured for each humidity; 15% had 0.204 ± 0.007 , 21%; 0.194 ± 0.009 and 88%; 0.220 ± 0.011 . It can be seen that humidity has little effect on the gradients of the data, with Gladyshev finding no statistically significant differences. They differ only by vertical position. Gladyshev constructed an empirical relationship based on these results:

$$\Delta T_s = 0.2T_{AW} - 54.8 \frac{\Delta e}{p} + 0.424 \quad (3.4)$$

where $\frac{\Delta e}{p}$ is a dimensionless quantity, p is the atmospheric pressure, T_{AW} is the difference between the temperature of the air and subsurface temperature of the water, and Δe is a quantity called the humidity deficit, discussed in Chapter 1, which can be calculated by:

$$\Delta e = e_{swT} - e \quad (3.5)$$

where e_{swT} is the saturation pressure of the water vapour at the given air temperature and e is the actual pressure of the water vapour.

As the 15% and 21% humidity plots are vertically lower than the origin, the results show cold skins are much more likely than warm.. For a humidity of 21%, T_{AW} needs to be around 4°C before ΔT_S becomes positive. At around 70% humidity these two processes become equivalent and the skin deviation follows the air temperature. Under these humidity conditions, if the T_{AW} is positive the skin is warm. If T_{AW} is negative the skin is cool.

An interesting event happens on the y axis where T_{AW} is zero. There is no sensible heat conduction and the surface temperature deviation can be related to the evaporation rate accurately. This has possible uses in measuring the evaporation rate under controlled conditions.

3.3 Other temperature-altering events

Aerial IR measurements of large storages show little temperature increase with coverage. This would tend to indicate there are processes acting to cool the monolayer surface. Sections 3.3.1-3.3.4 present cooling effects, using the idea that cold thermals are impeded by the increased viscosity.

3.3.1 Cold Thermals

As evaporation occurs, the skin layer cycles in thickness as cold thermals are released into the bulk. Cold thermals are defined here as packets of cold fluid which are released from the skin layer and sink into the fluid below, warm water then rises from below by advection (Volino & Smith 1999). The cold thermals act to drain and reduce the thickness of the conduction layer thereby allowing greater heat flux through the surface.

The source region of cold thermals is in the upper part of the subskin layer, (Katsaros *et al.* 1977) and they act as drains for the cool water in the skin layer. In spite of thermals affecting the effective thickness of the skin, they do not destroy the skin layer, or the temperature gradient which act across it (Gladyshev 2002:17). Takashi & Kunio Aseada (1989) assert that under average water storage conditions 96% of the heat conduction is transferred by thermals. The thermal may take the form of a sheet, vortex or plume. A sheet is a line of falling fluid that draws cool fluid horizontally from the skin layer to then plunge into the bulk fluid. A vortex spins the surrounding cool fluid downwards- like a funnel. A plume is a thermal which remains attached to the skin.

Despite IR images only gathering radiation from a surface layer 25 μm thick (Section 4.5.1) variations at the surface reflect thermal activity in the subskin zone which conduct through the skin layer. Since the subsurface and the air temperature are both, approximately, spatially uniform, the temperature measured can be related to the thickness of the skin (Saylor, Smith, & Flack 2000). When there is a thermal acting below the skin, as in darker areas (Figure 3.8), the temperature is lower because the skin becomes thicker. Conversely, in light areas where the skin is being drained a warm area shows as the skin is thinner and conducts more heat to the surface. Therefore on an IR image, the dark areas correspond to thick layers or thermal drains and the light areas correspond to warmer thinner skin.

Addition of a monolayer of hexadecanol to the surface increases the effective surface viscosity; increasing the thickness of the skin layer and reducing the magnitude of the subskin convective heat

flux. The dilational elasticity of the monolayer retards the horizontal speed of the fluxes just under the skin making them slower and larger (see Figure 4.10).

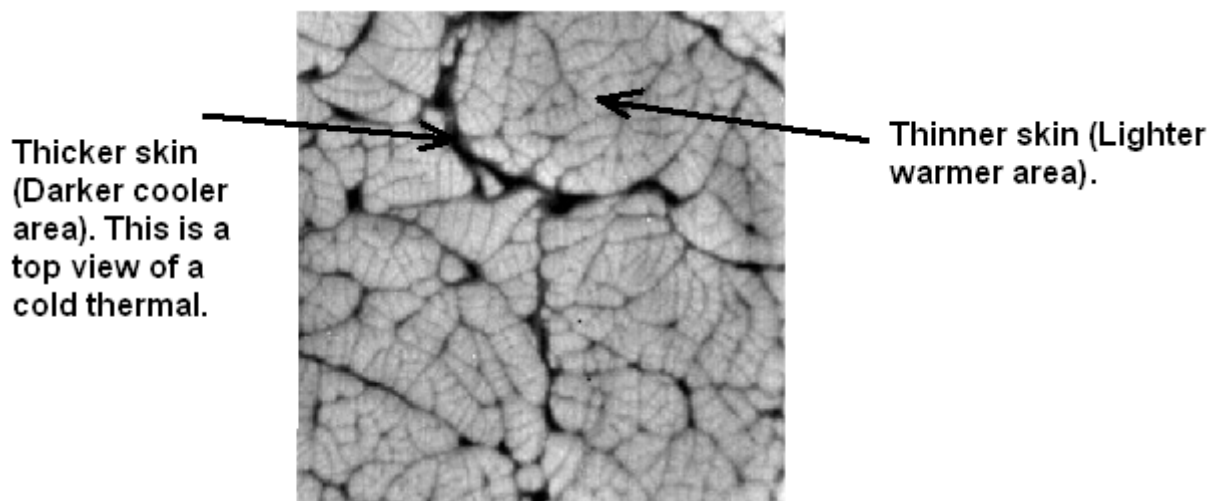


Figure 3.8 IR image of edge length; 17.1 cm, of a clear water surface with a heat flux of 407 Wm^{-2} . Source; Conover & Saylor (2006).

3.3.2 Effect of monolayers on the supply of heat to the surface

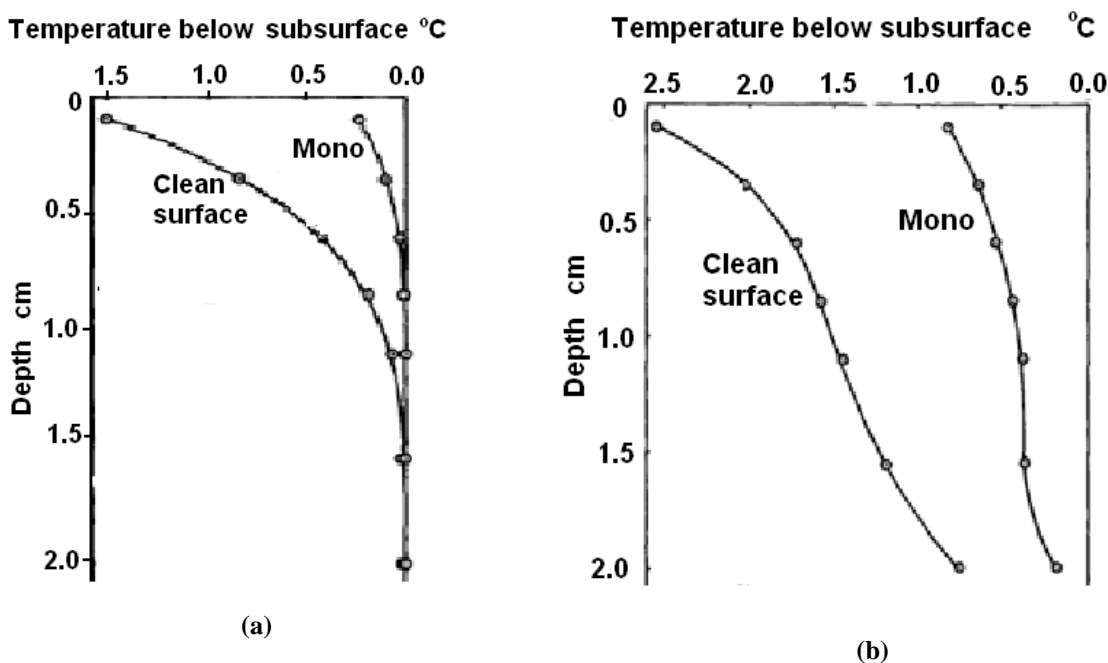


Figure 3.9 (a) Surface temperature profile for a bulk temperature of $2 \text{ }^\circ\text{C}$. (b) Surface depression temperature for clear water surface and hexadecanol monolayer at a surface pressure of 38.2 mN m^{-1} bulk water at $17 \text{ }^\circ\text{C}$. Adapted from Navon & Fenn (1971).

Finding whether there is an impairment to heat supply to the surface from the bulk caused by monolayers is important, as it would contribute towards reducing the size of the surface temperature increases caused by the evaporation reduction. This would make remote detection methods using

surface temperature much more difficult. Navon and Fenn (1971) have shown that impairment of convection in the convection heat flux under laboratory conditions by using an array of thermocouples in the top 2 mm of a trough. They compared clear water surface with hexadecanol monolayer surfaces. The temperature profile for the top 2 mm is shown for covered and clear water surface at 2 °C in Figure 3.9(a), and at 17 °C in Figure 3.9(b). At 2 °C there is no density induced convection caused by a cool skin. At 17 °C the shape of both covered and clear water measurements have changed due to the influence of convection below the skin. The heat flux can be gauged by the gradient of the temperature profile in the skin region as this is purely conductive heat transfer. From this, it can be seen that the heat flux is smaller in the case of the monolayer covering. The difference is presumably due to the reduction in evaporation afforded by monolayer.

Some of the lowered heat flux is caused by impairment of subskin convection caused by the increased viscosity of the surface, according to Navon & Fenn. There has been discussion over whether impairment of heat flux does actually affect the evaporation rate by “starving” the surface slightly of heat and cooling the surface.

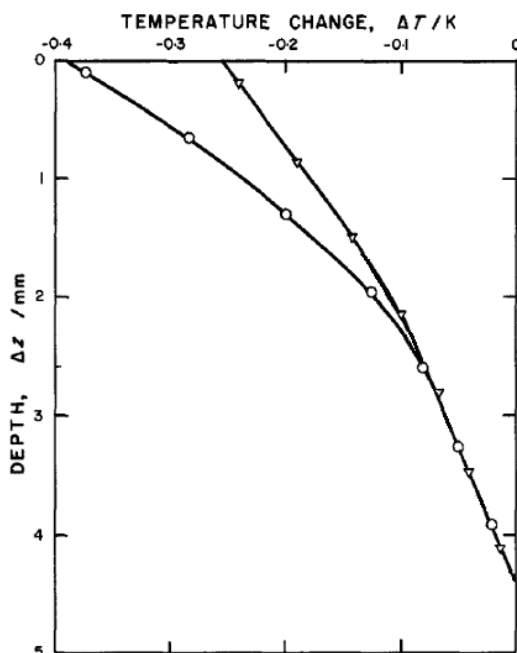


Figure 3.10 Temperature profile, found by using changes in interferometer fringes in a 5 mm deep trough. O; Clean surface with specific evaporation $m_e=0.53 \text{ g m}^{-2} \text{ s}^{-1}$. Triangle; Octadecanol at 20 mN m^{-1} with $m_e = 0.32 \text{ g m}^{-2} \text{ s}^{-1}$. Water temperature 25°C. Adapted from Barnes & Feher (1980)).

Barnes and Feher (1980) (Figure 3.10) used an interferometer to display the temperature gradient in terms of fringe shifts, with the aim of determining whether monolayers reduce the convection activity contributing to the evaporation resistance. They found no affect of heat flux impairment, with the temperature profile determined only by the change in evaporation resistance. However these measurements were performed in a 5 mm deep trough with no wind, and therefore a low heat flux. The absence of any differences due to convection in this data may reflect an absence of cold thermals in the very shallow trough.

There is evidence that under higher wind speed the viscosity of monolayer does affect the surface temperature.

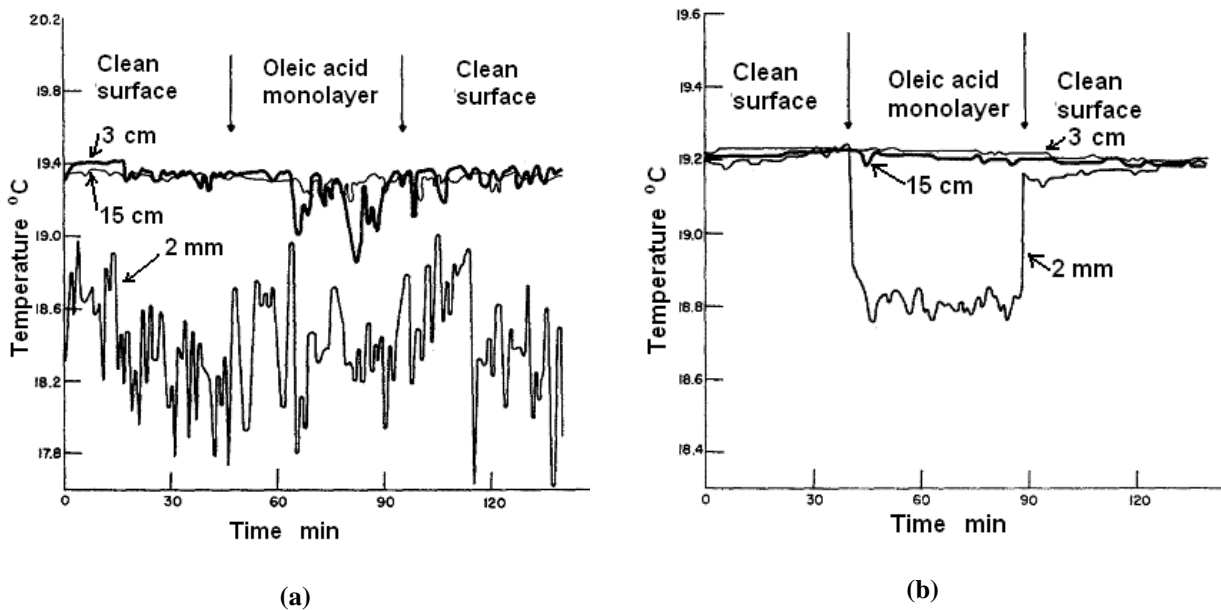


Figure 3.11 (a) Temperature profile of oleic acid at three depths 2 mm, 3 cm (dark line) and 15 cm. Gas N_2 at 0% R.H. and flow rate of 1.5 litres min^{-1} using full film pressure of 30 $mN m^{-1}$. (b) 55% R.H. and flow rate of 6 litres min^{-1} . Adapted from Jarvis (1962).

Jarvis (1962) has convincingly demonstrated a skin cooling effect of monolayers presumably produced by impairment of the subskin convection heat fluxes. He placed thermistors at the three depths of 2 mm, 3cm and 15 cm in oleic acid. Initially he noticed the larger temperature fluctuation under a water surface, indicating more active convective heat flux for all measurements. Under conditions of low humidity of 0% and low wind 1.5 litres min^{-1} (Figure 3.11(a)) there is no change in surface temperature, due to the low evaporation resistance of oleic acid (see Table 1.2). Conversely, under conditions of higher wind speed of 6 litres min^{-1} and higher relative humidity of 55%, there is evidence of surface cooling when the monolayer is added (Figure 3.11(b)). This appears to be due to impairment of the water heat fluxes to the surface, due to the surface viscosity of the monolayer effectively insulating the skin region from lower region to some extent as horizontal movement near the skin zone is impeded (Jarvis 1962; Marlatt & Grossman 1968).

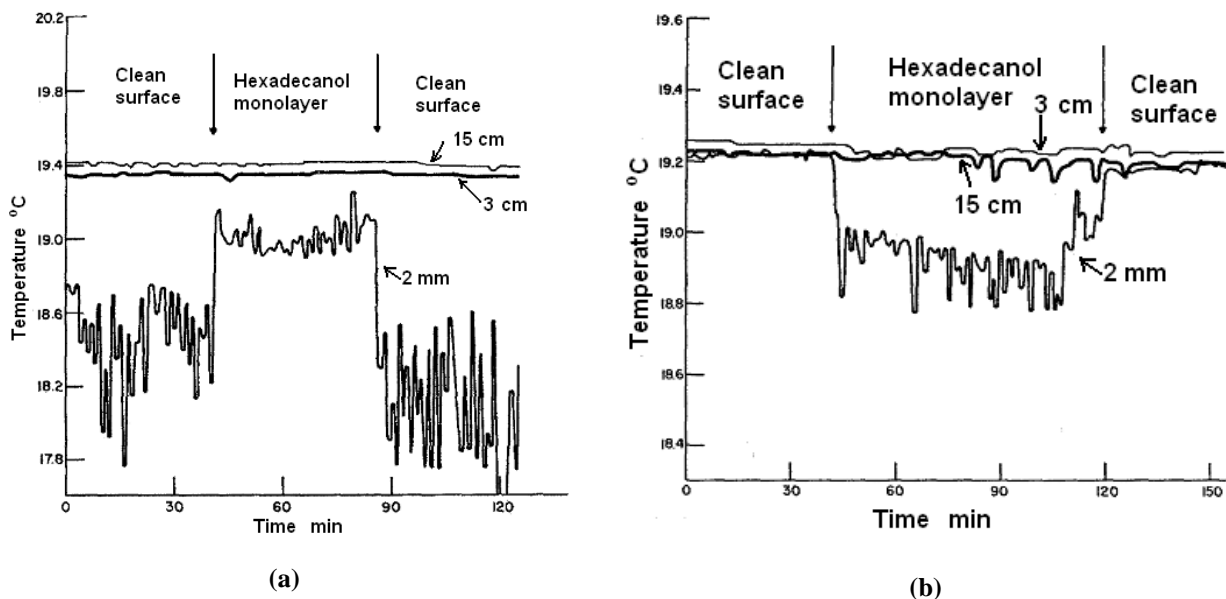


Figure 3.12 (a) Temperature profile of hexadecanol at three depths 2 mm, 3 cm (dark line) and 15 cm. Gas N_2 at 0% R.H. and flow rate of $1.5 \text{ litres min}^{-1}$ and full film pressure of 36 mN m^{-1} . (b) 55% R.H. and flow rate of $6 \text{ litres min}^{-1}$. Adapted from Jarvis (1962).

The procedure was repeated for hexadecanol. The low humidity (0%) and low wind speed ($1.5 \text{ litres min}^{-1}$), (Figure 3.12(a)) shows an expected relative warm surface due to lowering of evaporation rate. Conversely at high humidity (55%) and higher wind speed ($6 \text{ litres min}^{-1}$) (Figure 3.12(b)) the evaporation is reduced for the water surface. The monolayer surface is cooler, due to impairment of the heat flux. The cooling of the hexadecanol is perhaps slightly less than the oleic acid monolayer due to the evaporation resistance it possesses.

Jarvis notes that in high heat flux conditions any monolayer with sufficiently high viscosity is capable of impairing the convection currents and allowing a thin layer of insulated surface water to cool by evaporation by around 0.4°C (Jarvis 1962). Jarvis called this effect “Phlegmatizing” the surface as lateral movement is restricted and the natural convection motion underneath is impaired.

The apparent impairment of heat fluxes appears to be caused by an increase in effective skin thickness (Gladyshev 2002). This effect is important to note as it tends to reduce the magnitude of the surface warming that would be expected with application of evaporation reducing monolayers (Saylor, Smith, & Flack 2000). This insulation of the surface due to convection impairment would be the reason why IR radiometric detection aerial methods show only minor temperature differences with addition of monolayer (see Chapter 4).

3.3.3 Effect on spreading heat

The retardation of heat flux in the downward direction by monolayers (hexadecanol and others) was shown by Gugliotti *et al* (2004) with attenuation of convection currents given as an explanation, backed with imaging evidence. The apparatus consisted of a 50 mW , 532 nm Nd:YAG laser directed vertically downwards into a highly absorbent solution of concentrated crystal violet. The

air temperature immediately around the entry point was monitored. At the end of 5 seconds, a 15 fold increase in air temperature difference was measured when the surface was covered with hexadecanol, as the higher surface viscosity impeded the heat dispersing mechanisms which operate for a clean water surface.

This detection method would require accurate positioning of laser and temperature sensors at the surface. The main drawback to the use of this method is the impurities needed in the water to absorb the radiation near the surface. This perhaps could be overcome by using an IR laser, which would deposit radiation at the surface. This is still testing for surface viscosity which may indicate coverage for monolayer such as oleic acid, which do not reduce evaporation.

3.3.4 Nusselt Number

As explained in Section 3.1.3 the skin, subskin and subsurface layers are defined by the dominant heat transfer mechanism, with conduction occurring in the skin, and an increasing convective heat flux occurring as depth increases.

Convection currents are a more efficient mechanism for transferring heat than conduction in fluids, as whole chunks of the fluid alter depth due to differences in density (Barnes & Hunter 1982). By comparison, conduction is relatively inefficient, and thus exhibits a higher heat flux resistance.

The heat flux per unit area, Q_{cond} ($\text{W m}^{-2} \text{ } ^\circ\text{C}^{-1}$) transmitted by conduction in the vertical direction can be calculated using the heat transfer equation

$$Q_{cond} = \frac{k\Delta T}{L} \quad (3.6)$$

where k is the heat transfer coefficient, which for water at $20 \text{ } ^\circ\text{C}$ is 0.58 W m^{-2} (Kaye & Laby 1973), L is the depth, ΔT is the temperature difference between the bottom of a shallow trough and the depth being studied.

Suppose the layer is moving, so that convection occurs. The convective heat flux Q_{conv} would then be

$$Q_{conv} = h\Delta T \quad (3.7)$$

where h is the convective heat transfer coefficient. In the subsurface region, the heat transfer coefficient for small troughs is around $230 \text{ W m}^{-2} \text{ } ^\circ\text{C}^{-1}$ (Barnes & Hunter 1982) however this value increases with large storages.

In practise, heat is transferred within a water body to the surface by a combination of conduction and density-driven convection processes. The Nusselt ratio, Nu , is a measure of the relative contributions of the two mechanisms, and is given by combining Equations 3.6 and 3.7. to give (Navon & Fenn 1971):

$$Nu = \frac{Q_{cond} + Q_{conv}}{Q_{cond}} = \frac{\text{Total heat transfer}}{\text{Conductive heat transfer}} = \frac{Q}{Q_{cond}} \quad (3.8)$$

where Q is the total heat flux up to the depth being measured and Q_{cond} is the calculated heat conduction from the bottom of the tough to the depth being studied.

The Nusselt number is a dimensionless ratio that compares heat flux in a motionless fluid with one with only conduction currents. A value of unity would indicate very ‘sluggish’ movement of water, with only conduction occurring, whereas in turbulent flow, there is continuous motion of the fluid and the Nusselt number is of the order of 100-1000. Nusselt numbers are just above unity in the surface skin of a water body, and increase with depth as convection currents come to dominate the heat transfer processes (Barnes & Hunter 1982).

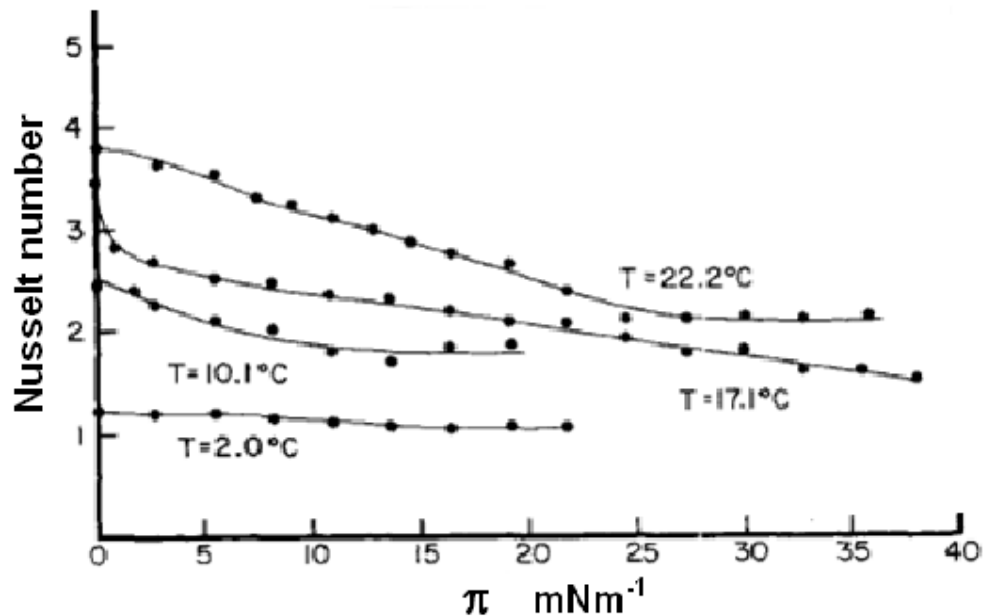


Figure 3.13 Reduction in convection with increasing hexadecanol monolayer pressure shown by a decrease in Nusselt number. Adapted from Navon & Fenn (1971).

Navon and Fenn (1971) obtained Nusselt’s numbers for clear water and hexadecanol covered surfaces at different surface pressures, taken from experimentally obtained figures for the evaporation resistance. Each data series in Figure 3.13 shows a different temperature, and it can be seen that increasing the temperature also increases the Nusselt number due to the decrease in viscosity and an increase in heat flux. At 2 °C the Nusselt’s number is about 1 since cooling causes expansion rather than contraction, leading to the loss of buoyancy driven convection. At higher temperatures monolayers are more effective in reducing the convective fraction of upward heat flux.

Gladyshev (2002:48) proposed that the decrease in convective heat flux is due to an increase in effective thickness of the skin, with the result that application of monolayer makes cool skins cooler and warm skins warmer.

3.3.5 Surface temperature deviation ΔT_S as a potential detection method

The reduction in evaporation associated with a monolayer should increase ΔT_S , however there is also the impairment of convective heat flux acting to lower the ΔT_S as shown in Section 3.3.2. There exists some possibility of a detection system for monolayers based on a change in ΔT_S that occurs with monolayer coverage. For the detection to be successful, the vertical heat flux would need to be

monitored, to account for the changes occurring to ΔT_S as a result of heat flux conditions. The value of T_{AW} affects ΔT_S as shown by experimental data in Figure 3.7 and Equation 3.4.

The ΔT_S was measured for a range of T_{AW} in a small laboratory vessel by Gladyshev and Sushchik (1994), for both clear and octadecanoic acid covered surfaces. The difference in ΔT_S between a clear water surface and monolayer of stearic acid plotted against T_{AW} is shown in Figure 3.14. This figure supports Gladyshev's argument (Gladyshev 2002:48) that monolayers make warm skins warmer and cool skins cooler, calling it a "dual effect". So for positive T_{AW} the ΔT_S becomes larger, while for negative T_{AW} it becomes negative. This is caused by suppression of the convective heat exchange between the skin and subskin layers (Gladyshev & Sushchik 1994) effectively insulating the surface, making it more susceptible to the influence of T_{AW} .

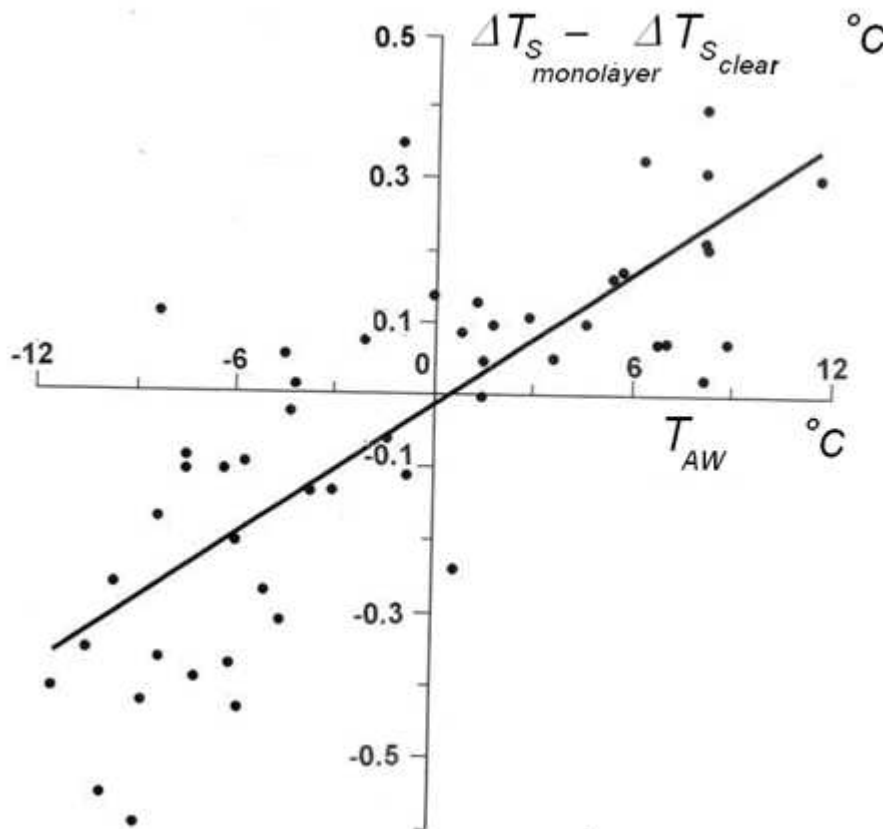


Figure 3.14 Difference between the surface deviation temperature with a monolayer ($\Delta T_{S\ monolayer}$) and that of clear water ($\Delta T_{S\ clear}$) as a function of the temperature difference between air and subsurface T_{AW} . Monolayer is octadecanoic acid. Adapted from (Gladyshev & Sushchik 1994).

The proportionality between the change in ΔT_S created by the monolayer ($\Delta T_{S\ monolayer} - \Delta T_{S\ clear}$) and T_{AW} are shown from measurements on a small laboratory trough by Gladyshev & Sushchik (1994) (Figure 3.14) with an air temperature of around 24 °C. For positive T_{AW} the surface is warmed by the presence of the monolayer, however for negative T_{AW} the surface is cooled. This figure would also indicate that temperature differences created by the monolayer are more evident with large magnitude values of T_{AW} , either positive or negative. In these results they found that it was not possible to avoid significant differences in air humidity, which affects the magnitude of ΔT_S and contributed to the scatter of points.

It is instructive to examine the values of ΔT_S for both a monolayer covered surface and for clean water for a range of humidities. Combining Gladyshev's (1988) earlier surface temperature deviation measurements for clean water at various values air-water temperature differences and relative humidities (Figure 3.7), with data in Figure 3.14, and assuming a proportionality between ΔT_S and relative humidity for a given T_{AW} (Section 4.5.4) yields the graph of Figure 3.15.

The solid red line indicates ΔT_S for water as a function of T_{AW} based on fitting the data extracted from Figure 3.7 and Figure 3.14. The dashed red lines are the 0% (Lower) and 100% (upper) relative humidities. The solid blue line represents ΔT_S for monolayer as a function of T_{AW} for 50% relative humidity, again based on fitting data extracted from Figure 3.14. So the difference between the two solid lines indicates the temperature difference between clear water surface and monolayer surface which increases in magnitude with the magnitude of T_{AW} .

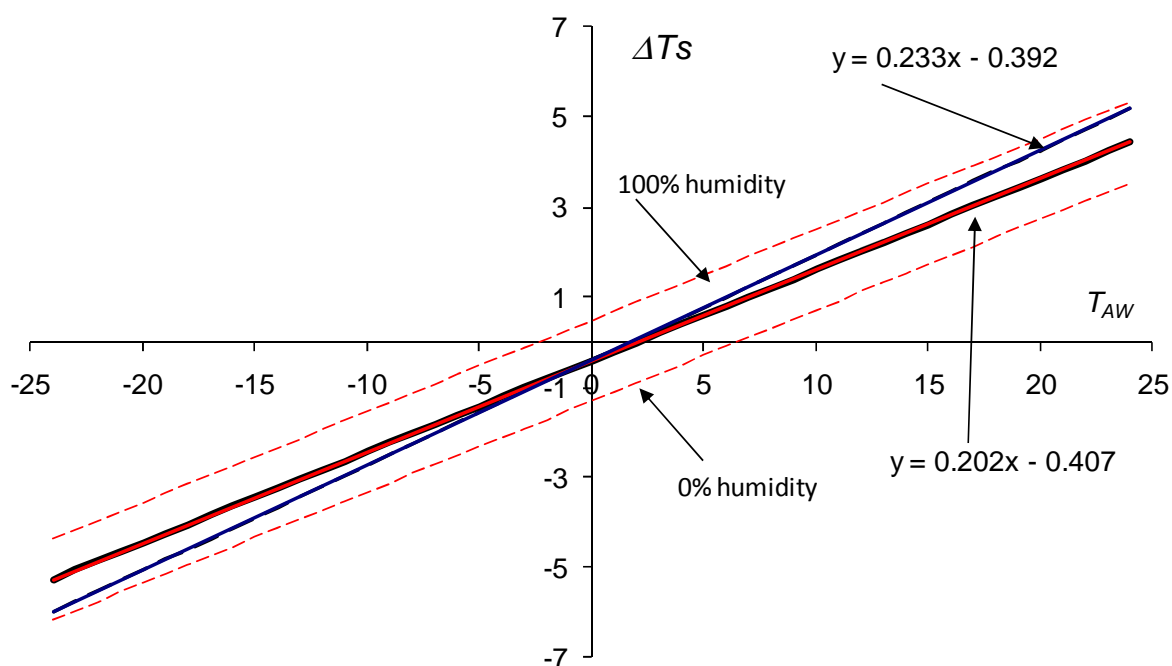


Figure 3.15 ΔT_S for a clean, and octadecanoic acid covered surface. ΔT_S for clear water surface at 50% humidity; Red solid line. The red dashed lines are an extrapolated range of humidity from 0-100%. Octadecanoic acid monolayer at 50% humidity; Blue line.

Whilst the data presented in Figure 3.14 suggests the potential of using T_{AW} to detect monolayers, it must be remembered that this figure was synthesised using data for octadecanoic acid at sea with only several humidity values. It is therefore necessary to produce a complete calibration dataset in order to check for the veracity of this approach, and importantly understand the potential conditions under which the approach is not likely to offer a clear delineation of surface conditions (that is monolayer or clean water). To this end, the following section describes a set of experiments aimed at verifying the potential suitability of ΔT_S as the basis for detecting monolayers. Other possibilities for detection involve measuring an increases in the skin thickness, due to higher surface viscosity as discussed in Section 3.2.1. Also a change in the bulk temperature of troughs due to changes in evaporation rate may show distinct differences. These will be experimentally tested.

3.4 Experimental contact temperature measurements

A PVC trough of water at thermal equilibrium provides an interesting model to examine processes that occur around the surface of water. The temperature of the surface is the result of a balance of the latent heat flux cooling as it drains the heat from the surface, while there is a reactive heat fluxes through the walls and upwards in the trough water. It would be expected that the surface would assume temperature with respect to the water in the trough rather than the surrounding air since the coefficient of thermal conductivity of air ($0.024 \text{ W m}^{-1} \text{ K}^{-1}$) is much lower than that of water ($0.58 \text{ W m}^{-1} \text{ K}^{-1}$) (Kaye & Laby 1973). From this base bulk water temperature, ΔT_S may be positive or negative as shown in Figure 3.7 due to air humidity and T_{AW} values.

3.4.1 Temperature profile in troughs using thermistors

A twin thermistor array was constructed and placed in identical tubes to compare the temperature profiles of a clear water tube to a hexadecanol covered tube to ascertain differences created by the addition of hexadecanol.

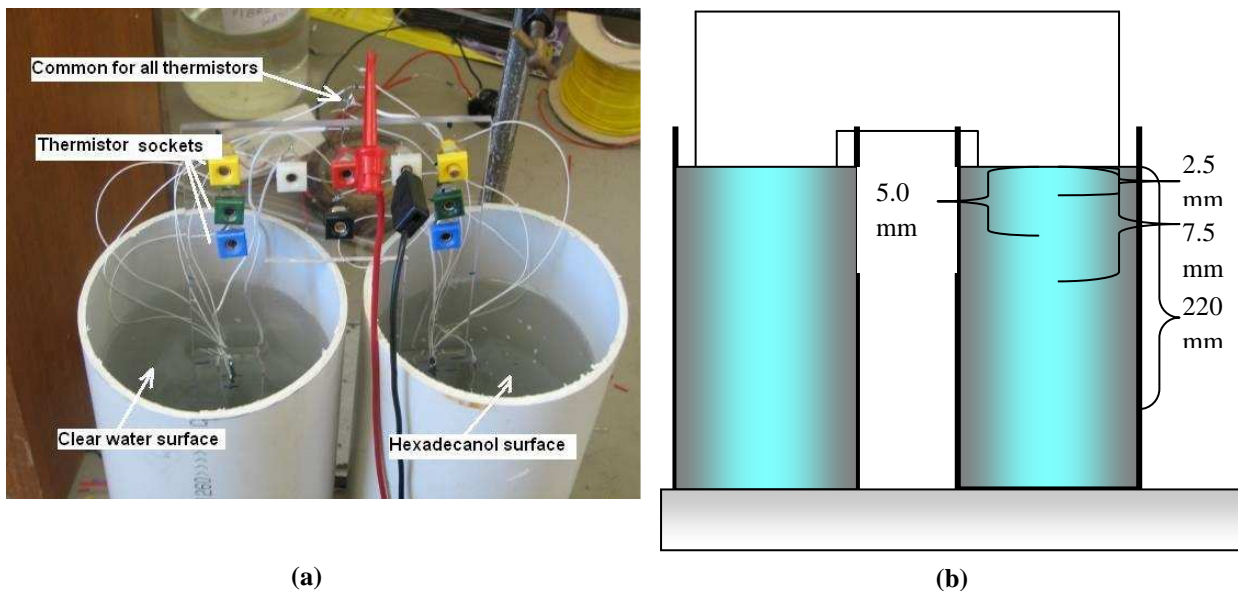


Figure 3.16 (a) Polycarbonate twin arm thermistor array positioned on the twin tubes. The excess crystals of hexadecanol can be seen floating on the surface of the right trough. (b) Depth of thermistors.

Materials and Methods

Two 100 mm diameter PVC tubes 30 cm long were capped and used as troughs to measure temperature differences. An inverted U shaped twin thermistor array was constructed from clear polycarbonate (Figure 3.16(a) and (b)) and four $10 \text{ k}\Omega$ 10K3A5421 thermistors (Betatherm, Ireland) were fastened through each arm of a twin armed thermistor array at a depth. The U shape was designed so that it could be rest on the rim two 30 cm high troughs. The size of the thermistors is shown in Figure 3.17.

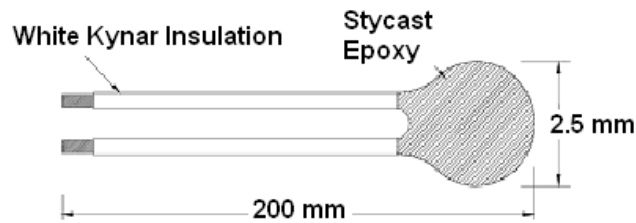


Figure 3.17 Size of the thermistors used.

The thermistors specifications state that they designed to have a resistance of 10 k Ω at 25 $^{\circ}$ with a tolerance of $\pm 0.1^{\circ}$ C for the range used. The NTC- negative temperature coefficient indicates that as the temperature increases, the resistance decreases. The temperature can be calculated from the measured resistance according to the Steinhart-Hart equation. This is a polynomial curve fitting relationship given as (Steinhart 1968):

$$T = \left(a + b(\ln R) + c(\ln R)^3 \right)^{-1} - 298.15 \quad (3.9)$$

where a , b and c are constants. For the thermistors used these are given as: $a = 1.129241 \times 10^{-3}$, $b = 2.341077 \times 10^{-4}$, $c = 8.775468 \times 10^{-8}$.

The water level was adjusted in each tube so that the top thermistor was 2.5 mm deep. The temperature profile of both tubes could then be measured concurrently so that comparisons could be made under identical conditions once thermal equilibrium was established (the apparatus was left overnight to reach thermal equilibrium). A Fluke 8840A (USA) multimeter was used to measure resistance of each so that the temperature could be calculated. The thermistors were purchased, covered with an epoxy resin, as shown in Figure 3.17, however were not water proof, so before use they were covered with a few coats of polyester resin.

The leads of the thermistors were soldered to 6 mm banana sockets so that the leads of the multimeter could be plugged into each socket with one end of each being joined to a common socket to allow the resistance of each could be measured by moving one plug as shown in Figure 3.16(a). Measurements of temperature were made under still conditions and under wind by using a 50 W desk fan (Brinsmead Delux, Model TO 300, Email Ltd, Australia).

Results and Discussion

Results (shown in Figure 3.18(a) and (b)) are the averages from several readings and show an increase in temperature near the bottom of the trough. This temperature gradient is along the length of the tube, and is due to the heat conducted through the sides and floor of the trough into the water, while latent heat processes are draining heat at the surface. However it is not being convected to the top as would be expected for large water storages (Strub & Powell 1987), probably due to impairment of convection currents by the walls and small size of the trough.

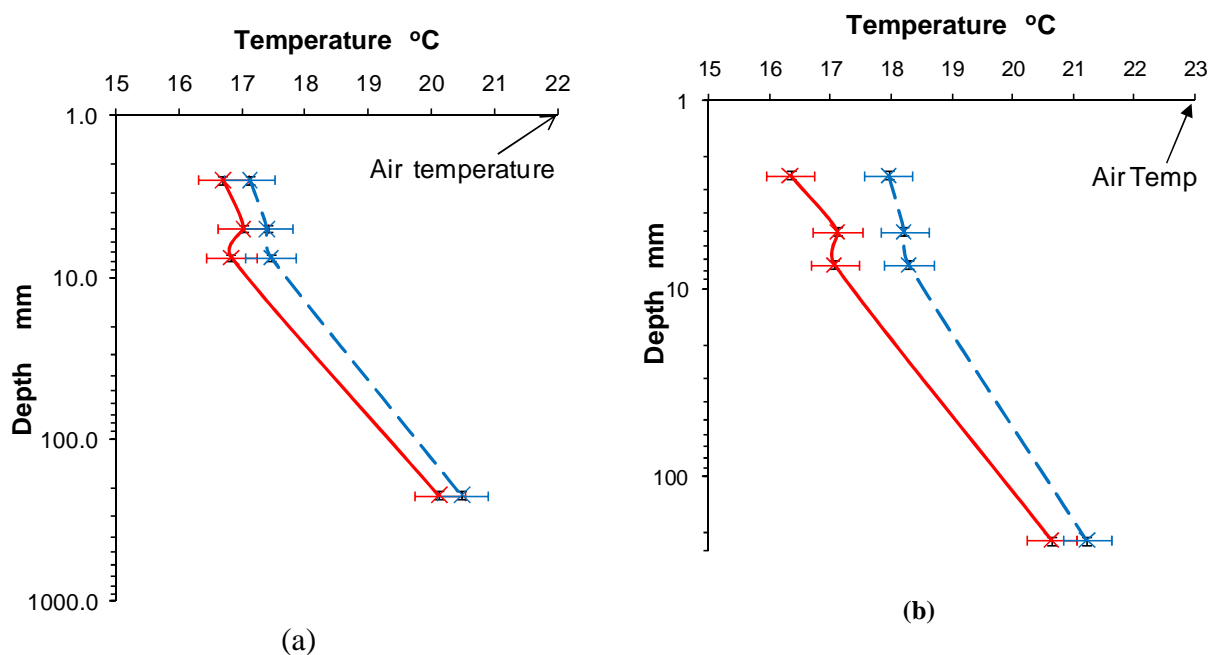


Figure 3.18(a) Temperature profile in 30 cm deep trough for no wind conditions for clear water (×) and hexadecanol (*). **(b)** Addition of wind at a speed of 2.2 m s⁻¹. Error bars were estimated to be 0.4 °C, gained from the variations in measured temperature using thermistors in this setup.

Differences in temperature profile between the clear water and hexadecanol covered surfaces were distinguishable for all measurements due to the lower evaporation rate of monolayer surface. Under conditions of no wind (Figure 3.18(a)) the difference was ~ 0.5 °C. Windy conditions (2.2 m s⁻¹ measured just above the trough), showed an enlarged difference between the two profiles, (Figure 3.18(b)) particularly near the surface, increasing to ~2 °C. Care was taken under windy conditions to leave several hours for thermal equilibrium to be established. So the hexadecanol surface shows an increased effectiveness at reducing evaporation under wind conditions, as evidenced by the larger temperature difference.

This confirms that the effect of wind increases the evaporation reduction effect of hexadecanol, as determined by MacRitchie (1969). The effect of artificial wind creates a larger temperature differences between clear water and monolayer, which may be useful in developing methods of monolayer sensing.

If a linear line of best fit is drawn through the data the temperature gradient decreases by 19% for water altering from 15.3 to 18.3 °C m⁻¹ with the addition of wind. If the same is carried out for hexadecanol the gradient alters from 14.8 to 14.4 °C m⁻¹, a fairly similar value with a difference of 3%. This shows the differences in evaporation reduction created by wind is mainly due to the increased evaporation of water, rather than to any substantial change of effectiveness of the monolayer.

Conclusion

The addition of wind increases the evaporation reduction of hexadecanol, mainly by increasing the evaporation of a clear water surface, with which it is compared. According to these results monolayer detection methods relying on temperature would show greater contrast with the addition

of an artificial wind over the surface. This comparison of temperature profiles would be difficult to obtain in the field as clear water reference surface easily becomes contaminated (Chapter 2).

3.4.2 Estimation of ΔT_S measured with a logged three thermistor array

To avoid the use of a reference water surface as used in the previous experiment a search was begun for temperature characteristics that occur distinctively with the presence of monolayer. Measurement of ΔT_S was carried out using a three thermistor array, which was attached to a micrometer screw gauge so that it can be positioned very accurately. Positioning is particularly important for the middle (surface) thermistor, due to proximity to the surface and the large skin temperature gradient.

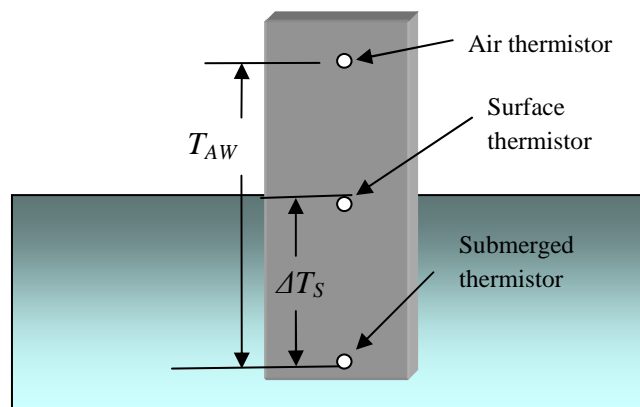


Figure 3.19 Arrangement for measurement of T_{AW} and ΔT_S .

Materials and methods

Three small holes were drilled in a Perspex sheet 12 cm apart. The leads of the previously used thermistors were fed through each hole, so that the sensor protruded a few mm through the hole. Silicone sealer was applied to the lead side of the polycarbonate sheet to hold the thermistors in place. The whole array was then attached to a micrometer screw gauge stand using a boss head clamp, so that the position of the middle thermistor could be accurately adjusted relative to the surface of the water. The top and bottom thermistors would also move but it can be assumed that the difference in temperatures produced for small height adjustments for the thermistors would be minimal. The array was positioned on a plastic trough, 30 cm in diameter, which had a water depth of 35 cm, so that the surface thermistor was positioned just under the water. This was carried out by lowering the array so that the surface thermistor was completely submerged, then raising it until the first sign of surface disturbance/meniscus was evident. This often took several attempts since as soon as a normal meniscus appeared around the thermistor the top appeared not to be covered with water. Considering the original diameter of the thermistors were 2.5 mm (Figure 3.17) and some additional thickness created by the polyester resin the effective depth for this thermistor would be close to 1.0 ± 0.2 mm.

Wind conditions were created with the 50 W Brinsmead desk fan directed horizontally across the surface. The high positive T_{AW} values were obtained by adding ice to the trough.

In the absence of measurable absolute differences that monolayer produce to the water storage, it was considered that differences may be amplified if a parameter which affects evaporation is

artificially altered on a contained sample of surface. Wind is the obvious choice, since it is proportional to the evaporation rate (Equation 1.1) and because it is easy to alter.

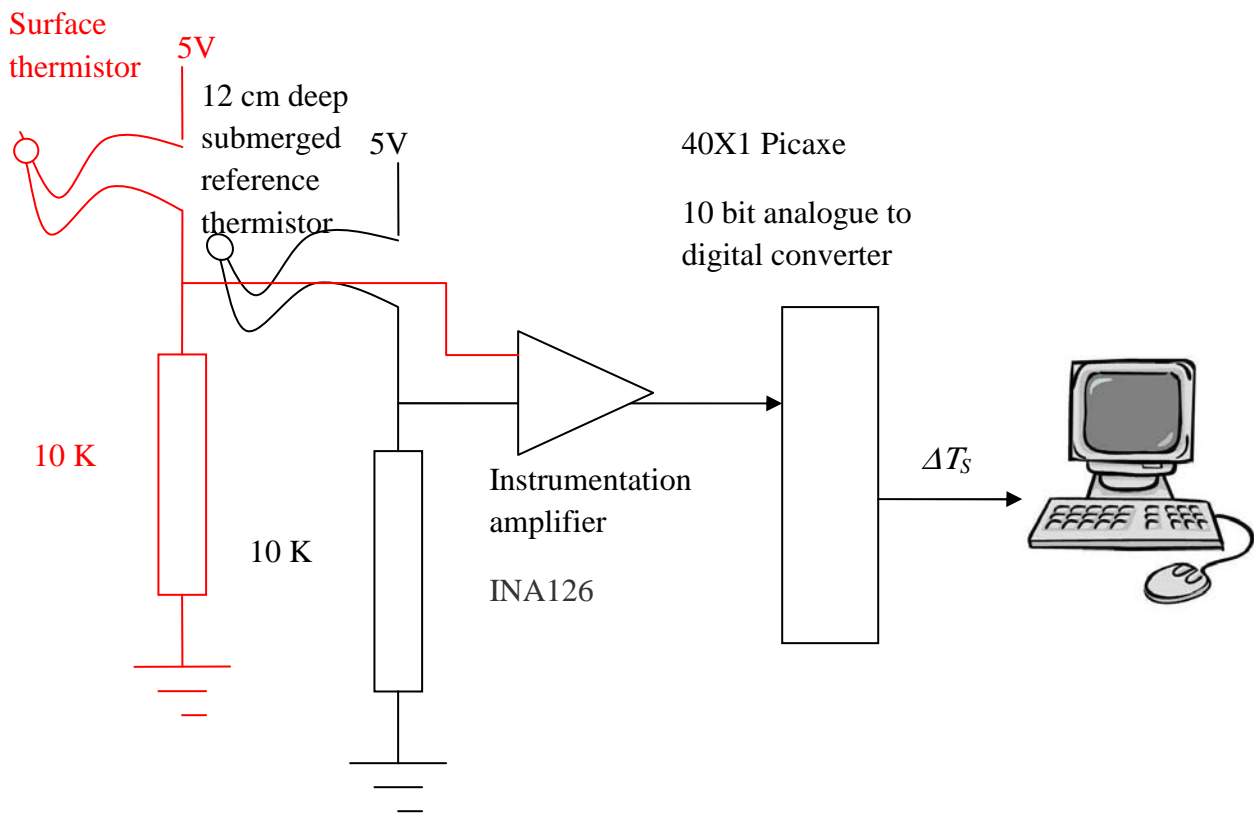


Figure 3.20 Wiring diagram used to measure ΔT_s using thermistors. The T_{AW} used an identical setup, both referenced to the same 12 cm deep thermistor.

Both the air thermistor T_{AW} and surface thermistor ΔT_s were referenced to the submerged thermistor. This was done by connecting each of the thermistors to a 5V voltage divider, which were made up of a 10 k Ω 1% tolerance resistor in series with the thermistor as shown in Figure 3.20. This converts the resistance of the thermistor to voltage. The small voltage differences between each of the surface and air thermistors and the submerged thermistor was then amplified, using an INA 128 Instrumentation amplifier (Texas Instruments, USA). These comprise a dual amplifier that minimizes the input current, so that the voltage measurement from the voltage divider is not affected. The circuit diagram of the amplifier is shown in Figure 3.21.

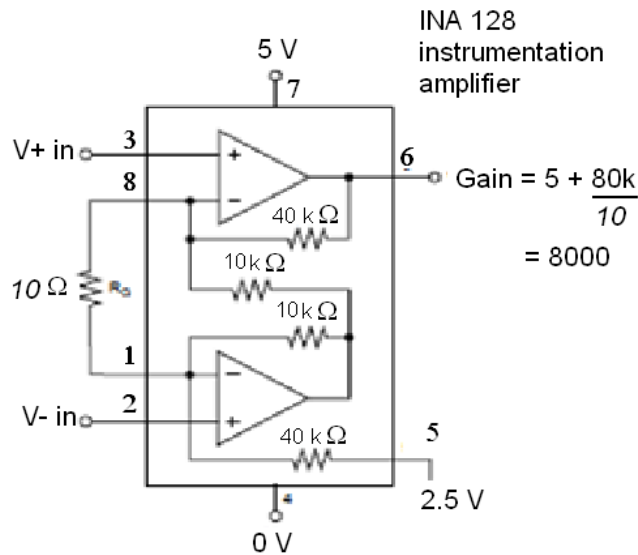


Figure 3.21 INA 128 Instrumentation amplifier with a zero reading at a reference voltage of 2.5 V.

An artificial balance point of the amplifier, at 2.5 V was created by attaching 2.5 V to the reference voltage (pin5), to allow for higher or lower temperatures than the reference submerged thermistor, so that not only higher temperatures at 2.5-5 Volts can be measured, but also negative temperatures corresponding to the region 0–2.5 V.

The 0-5 V amplified output is then connected to a 40X1 Picaxe microprocessor (UK) containing using 2 of the 4 digital to analogue A/D converters available, one for each of T_{AW} and ΔT_S . Using a 10 bit conversion (1024 levels), the 2.5 (temperature = 0) value would then correspond to a recorded level of 512. Positive temperature differences would be larger than 512 and negative temperature differences would be smaller.

The 2.5 V reference voltage was obtained roughly by simply using two 1kΩ resistors in series as a type of voltage divider. The program for the microprocessor was written to keep checking the true value of this voltage (with another A/D converter), and include this value as the amplifier's zero in calculations. The microprocessor was programmed to measure the values temperature every 5 seconds. This data was logged by a desktop computer using serial communication.

The result of this connection was an adjustable sensitive automatic system which can record small differences in temperature for the surface and air referenced to the 12 cm deep submerged thermistor. The amplifier could be easily adjusted to use as much of the 5 V output range as possible by varying the value of feedback resistors.

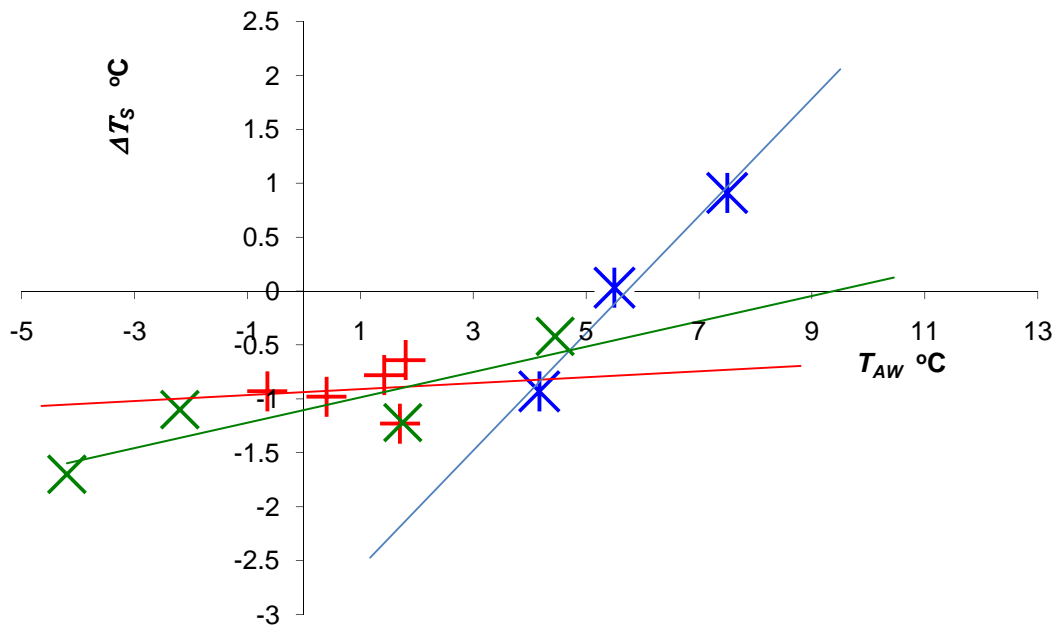


Figure 3.22(a) ΔT_s for water (+), hexadecanol (*) and conditions of a wind speed of 2.2 m s^{-1} over water (x) for several T_{AW} values with linear line of best fit fitted to each.

Results, discussion and conclusion

Averaged results for T_{AW} and ΔT_s , taken every 5 seconds over 5 minutes, are plotted in

Figure 3.22. They are fairly similar to the reported values of Gladyshev (Figure 3.7), showing that T_{AW} does affect ΔT_s , and that for a value of T_{AW} of zero, ΔT_s is a fraction of a degree below zero. However the large scatter in these results makes reliance on T_{AW} uncertain as an indicator of coverage. Gladyshev's results were for large surfaces, whereas these results have been produced using a small indoor container.

The proximity of the thermistors to the polycarbonate sheet probably introduced some degree of edge effects. Critically, slight variations in positioning the surface thermistor at $1.0 \pm 0.2 \text{ mm}$ would also affect results, since this is the area of largest temperature gradient. The lack of clear differences between clear surface, hexadecanol and the influence of wind for small temperature differences, combined with the effect of T_{AW} made it clear that measurements of this type needed to be in a controlled environment and in a standard enclosed sampling chamber.

3.4.3 Climate Chamber

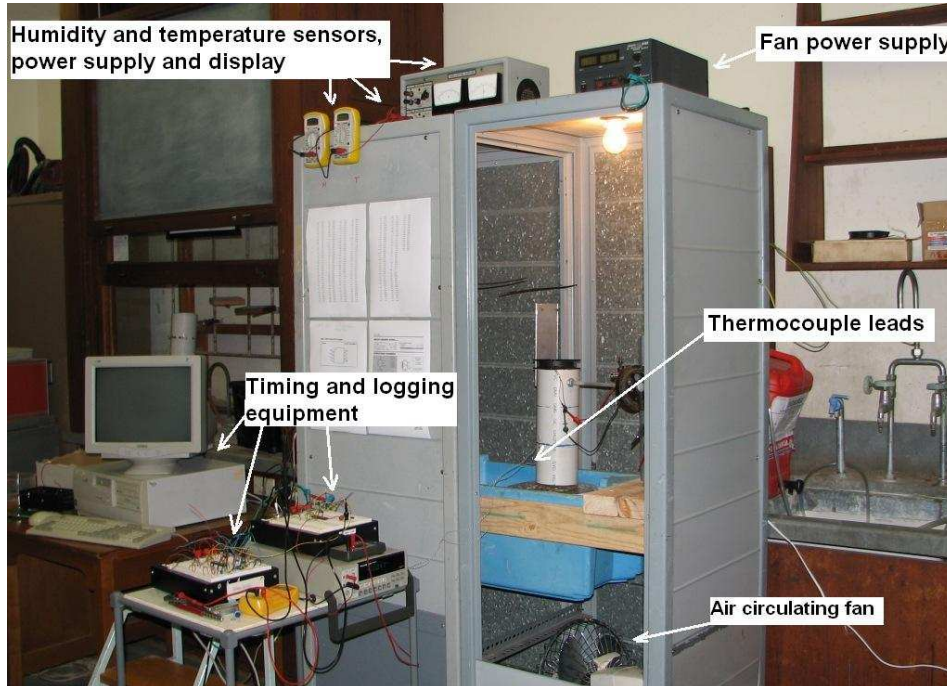


Figure 3.23 Climate chamber testing single tube.

In order to control humidity and temperature, a climate chamber was constructed by attaching two equipment shelves together and hinging a clear Perspex door on the front. A shelf was added at a height of around 1 m as shown in Figure 3.23. It was positioned next to a sink, so that water could be added to the sampling trough, overflowed into a larger container and siphoned back to the sink, to clean the surface of the trough.

The conditions were measured and controlled in the chamber with the following equipment:



Figure 3.24 (a) Photograph and (b) dimensions of the humidity/temperature sensor.

Humidity and air temperature sensing

A Novus RHT-DM sensor/transmitter (Novus Automation, UK) was fastened through the top of the chamber and connected to a 15V supply. The sensors are located on the end of a 200 mm probe constructed with a stainless steel sheath (Figure 3.24 (a) and (b)). It has 4-20 mA separate outputs for temperature and humidity, which can be measured with multimeters (screwed to the top left of

the climate chamber). Specification sheets show 3% accuracy in measuring humidity, and 1% accuracy in measuring temperature in the range used (Novus Automation Inc 2008).



Figure 3.25 (a) Ionmax humidifier. (b) Suki dehumidifier.

Humidity control

A separate humidifier and dehumidifier were used to control humidity, both placed in the bottom of the chamber. The humidifier (Ionmax Ion 60, Andatech Corporation Pty. Ltd., Australia). possessed a controlling humidistat could be set at 5% intervals between 30%-70%, with a continuous operation option. No specification regarding its accuracy for the humidistat was given, however the Novus humidity sensor showed an agreement to within 5%. When there was a difference between the two sensors an average was taken, as there may have been a difference due to location of each. The dehumidifier (Suki, WDH-101P B-type, Applied Climate control Australia) increased air temperature slightly when left running, about half of this temperature increase was overcome by attaching a bar fridge with the door removed, to the outside of the chamber so that the steel of the chamber was cooled to the temperature of the fridge.

It was found that the humidity could be reliably varied from 30% to 90% using these units.

Temperature control

A 2000 W air forced heater (Onix FH-03-08, China) with thermostat control was also placed in the climate chamber to increase temperature in some experiments. For some experiments it was controlled using the microprocessor to switch a a 240V solid state FET relay (fully described in Section 4.5.5.).

Circulation of air

A 12 volt 240 mA computer exhaust fan (Sunon MD1208PTS1, Taiwan) was attached to the ceiling of the chamber to circulate air to prevent stratification of the air from producing a large temperature gradient. This was found to be insufficient to eliminate stratification, and temperatures were measured at the level of the experiment. Therefore another 50 W desk fan (Brinsmead Delux, Model TO 300, Email Ltd, Australia) was placed on the floor of the chamber (Figure 3.23). This

produced an air flow which did not affect the experiment unduly but was strong enough to eliminate vertical temperature gradients.

Cleaning surface

To obtain water with a surface tension close to the tabulated value, it was found best to flood an inner container to overflow as described in Section 2.6.1, so that any impurities lowering the surface tension would flow out of the container. This also helped remove any traces of monolayers from previous tests. The chamber was placed closed to a sink so that this could be carried out, using clear polyvinyl tubing to carry the water to and from the chamber. Tap water was added to a containing vessel so that it would overflow into the large blue trough, where it was siphoned back into the sink. This method worked very effectively at purifying the surface, as verified by the initial rapid spreading of hexadecanol crystals and oil indicators.

3.4.4 Preliminary measurements using 100 mm PVC pipes

Surface measurements are more accurate if carried out in a standard enclosure, where waves, sunlight, underwater turbulence and wind cannot affect results unduly. A few containers were trialled, made of copper and polystyrene, however a 30 cm long, 100 mm diameter PVC tube proved to be the best standard containment model, since they are very inexpensive, water resistant, easy to glue, and have good thermal insulating properties. They are also large enough to contain a surface which allows a reasonable degree of convection within the water. Initial measurements were made of temperature profiles within these tubes, as it was considered important to contrast water temperature profile characteristics, for monolayer and clean water situations to determine any reliable differences. Wind flowing over the surface showed larger temperature differences between clear water and monolayer as results show in Section 3.4.1, so artificial wind was also used.

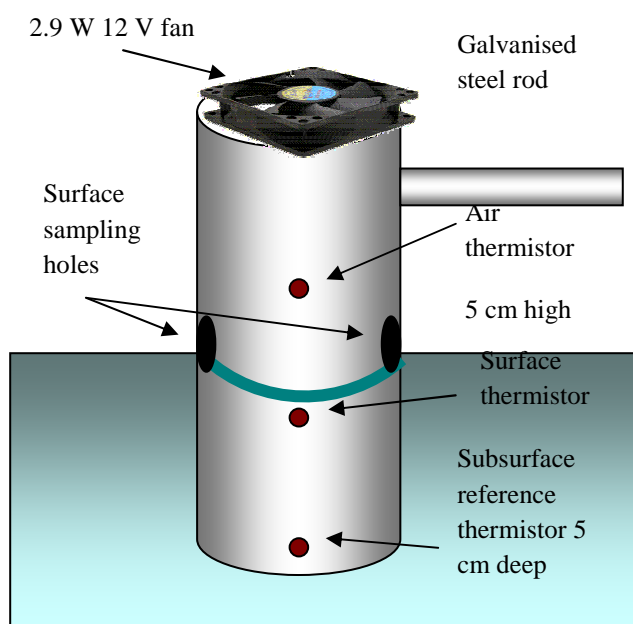


Figure 3.26 Thermistor tube setup to measure ΔT_S and T_{AW} with the reference ~ 5 cm deep.

Material and methods

Thermistors were pushed through a small hole into the tube from the outside, one just submerged, an air thermistor at 5 cm high and a reference one at a depth of 5 cm. The wires on the outside of the tube were glued so as to position the sensor on the inside fairly close to 5 mm from the wall. A galvanised iron arm was bolted to the tube so that the other end of the arm could be connected to the micrometer screw gauge stand. The whole assembly was then adjusted to position the surface thermistor just below the surface. A 12 V 2.9 W (Sunon MD1208PTS1, Taiwan) computer exhaust fan was positioned on top of the tube so that turbulent wind was created, which would not horizontally stress the surface and perhaps reduce the monolayer coverage. Slits which measured 6 mm wide by 25 mm high were drilled into the side of the tube at water level so that the air and monolayers can move into the interior of the tube. The wind speeds were measured just above the fan thus were not the air speeds near the surface of the water, though they should be proportional to it.

Results

The relative temperatures ΔT are shown in Figure 3.30 below for thermistors placed at various depths for clean water and water with a hexadecanol monolayer. The graphs show the greater cooling of the surface layers in the absence the monolayer, shown by the generally lower surface temperature values. The water plot also shows that a large temperature gradient in the skin/subskin layers is only obtained for a medium wind condition. For low winds the evaporation is too low to lower the skin temperature, for high winds, there is too much surface turbulence for the skin layer to establish a skin layer temperature variance.

The skin/subskin layer is only apparent in the top 1.5 mm for water. The hexadecanol plot shows much thicker skin/subskin layers extending to a depth of around 8 mm particularly with the higher heat flux (larger T_{AW}) runs. This is consistent with the reported impairment of the sub skin convection layers caused by monolayers (Saylor, Smith, & Flack 2000).

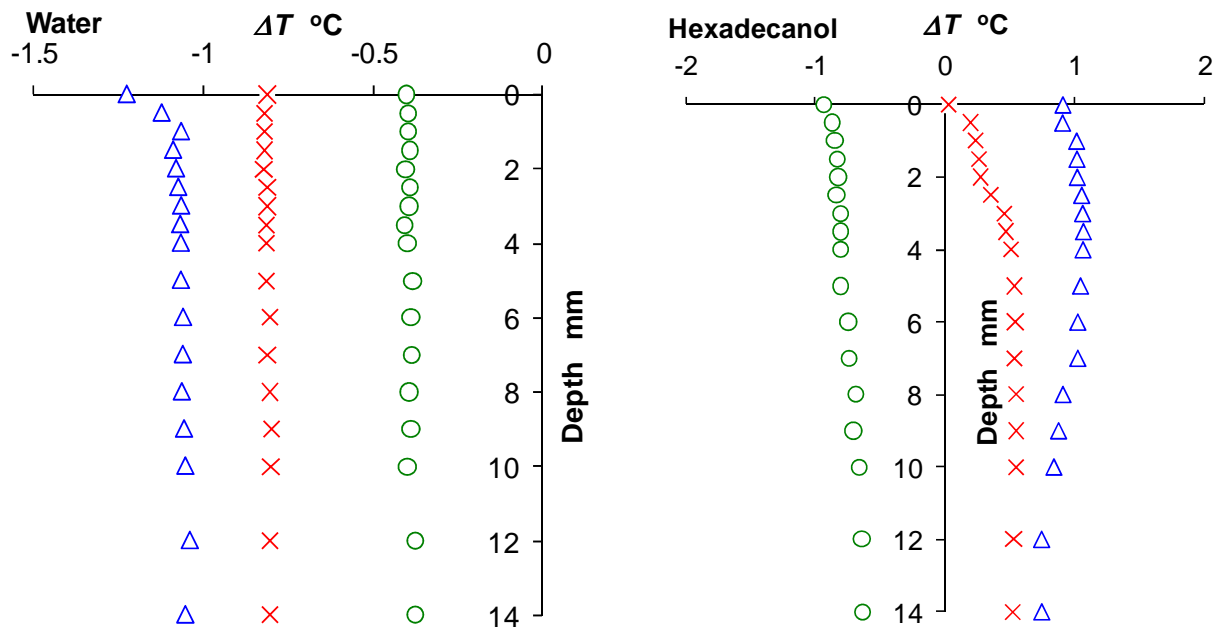


Figure 3.27 Temperature profile for water in the PVC tube for various T_{AW} and wind conditions for water (a) Water with no wind and $T_{AW}=1.7\text{ m s}^{-1}$; \times , wind speed 2.5 m s^{-1} ; Δ , $T_{AW}=2.2\text{ }^{\circ}\text{C}$ wind speed 6.3 m s^{-1} , $T_{AW}=2.5\text{ }^{\circ}\text{C}$; \circ . (b) hexadecanol with no wind and $T_{AW}\text{ }^{\circ}\text{C}=5.0$; \times , no wind, $T_{AW}=5.5\text{ }^{\circ}\text{C}$; Δ , 2.2 m s^{-1} , $T_{AW}=5.5\text{ }^{\circ}\text{C}$; \circ .

3.4.5 Surface temperature variation with wind speed in tube

The apparatus described in Section 3.4.4 was again used, only varying the fan speed, and measuring the resulting changes to ΔT_S . The fan could be inverted so that both air speed upwards and downwards could be analysed. A photograph of the turbulent effect of high fan speed on the surrounding water, with the tube out of the water, is shown in Figure 3.29.

Materials and Methods:

Figure 3.28 was obtained by varying the voltage of the fan was varied from -6 m s^{-1} pushing air downwards to $+6\text{ m s}^{-1}$ - pushing air upwards. The fan was left on for 1 minute at a time, and the surface temperature was taken towards the end of the minute. The fan was then left off for 15 minutes before continuing with another measurement. This technique was used to correct earlier methods, where the fan was left on, and the surface temperature was reduced significantly, altering the measured T_{AW} .

It was hoped that the ΔT_S as measured with the surface thermistors would show a different resulting magnitude when the monolayer was added. This would also depend on T_{AW} , which was measured with the air thermistor and was kept as constant as possible during these runs. .

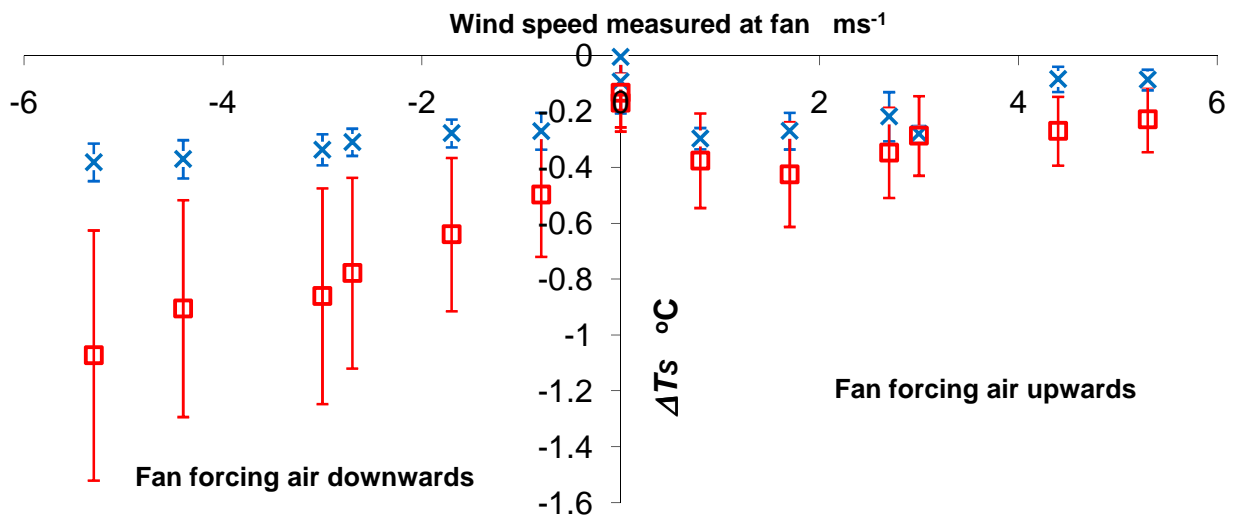


Figure 3.28 ΔT_s variation with fan speed in single tube. Water; \square . Hexadecanol; \times . Error bars are ± 1 standard deviation.

Results:

Figure 3.28 shows the difference in ΔT_s averaged over 14 runs. During these measurements the air temperature was 16-22 °C and ambient humidity between 30-40%. Each run was started at the left or right of the graph and continued through the origin. Measurements were read when the system appeared to stabilize.

When the fan was forcing air upwards from the water surface the water level was observed to rise within the tube by 1-2 mm for only the highest air flow speeds. This increases the actual depth of the subsurface/sub skin thermistor by the same amount which reduces the magnitude of ΔT_s . This can be seen on the right hand side of Figure 3.28.

Conversely when the fan was forcing air downwards onto the water surface the water level was observed to depress the water level by a similar amount, again only for the highest air flow speeds. The large fan speed also increased the turbulence and it was noticed that the waves splashed onto the thermistor keeping it always moist, even if out of the water. This would have the effect of cooling the surface thermistor. The surface of the monolayer is cooler than the water surface when both are compared to the temperature 5 cm down.

Conclusion

The use of thermistors in comparing surface temperature with a reference 5 cm deep value to determine ΔT_s showed that the presence of monolayer reduced ΔT_s at all wind speeds. However the design of air flow in this single tube model is probably affecting results, particularly at high wind speeds by altering the water level. It was also becoming apparent that accurate differences in temperature were needed, and for these small temperature differences, thermocouples are more accurate, and therefore used in the following experiments.

3.4.6 Time dependence of ΔT_S in tube using thermocouples

The ΔT_S was measured referenced to a depth of 5 cm over 10 minutes for a range of fan speeds with a clear and hexadecanol covered surface. This time was used as a maximum time as the outside trough containing the experiment began to cool with the increased evaporation, which increased the T_{AW} value.

Materials and Methods

The thermistors were replaced with Type T copper-constantan thermocouples (Lab Facility, UK), which were smaller, have no self heating issues and do not require a voltage divider to measure and log data automatically. The thermistors were originally used only to provide absolute temperature values. However, with the importance of T_{AW} and ΔT_S since becoming apparent, the thermocouples seem more appropriate. It was found that after about a month of use, the thermocouple junction oxidized to the extent that the junction broke. The cause was traced back to the amplifier, which was zeroed at +2.5 volts. (It was needed to be at this value to allow the Picaxe to measure positive and negative temperature differences from the reference junction. The corrosion was overcome by dipping the junctions in polyester resin and drying several times before use.

ΔT_S was measured by positioning one junction of the each thermocouple 5 mm through the the wall of the tube into the inside just below water level, while the other reference junction was pushed through at a depth of 5 cm. T_{AW} similarly was measured by positioning one junction 5 mm away from the wall on the inside of the tube at a height of 5 cm with another reference junction near the first reference thermocouple.

The Texas instruments INA126 instrumentation amplifier used for the thermistors was found to drift badly when amplifying by a much larger value. To overcome this, a “Zero-Drift”, low input offset amplifier Linear Technology LTC1050, which has a specified maximum input offset voltage of 5 μV and very low drift with temperature of 0.05 $\mu\text{V } ^\circ\text{C}^{-1}$ was used. This ensured that zero output of the amplifier value would always correspond to zero input.

The amplification was easy to adjust feedback resistor used was 220 k Ω for the ΔT_S value and a less sensitive 470 k Ω for the T_{AW} , with the resistor to ground 270 Ω . For the ΔT_S , the gain could be calculated from:

$$\frac{R_f}{R_g} + 1 = \frac{220000}{270} = 815.8 \quad (3.10)$$

So in used with a T type thermocouple with a voltage output of 0.041 mV $^\circ\text{C}^{-1}$. The voltage measured in mV needs to be divided by:

$815.8 \times 0.041 = 33.4$ to gain the temperature difference in $^\circ\text{C}$. Similarly the less sensitive T_{AW} amplifier gives a dividing value of 7.1.

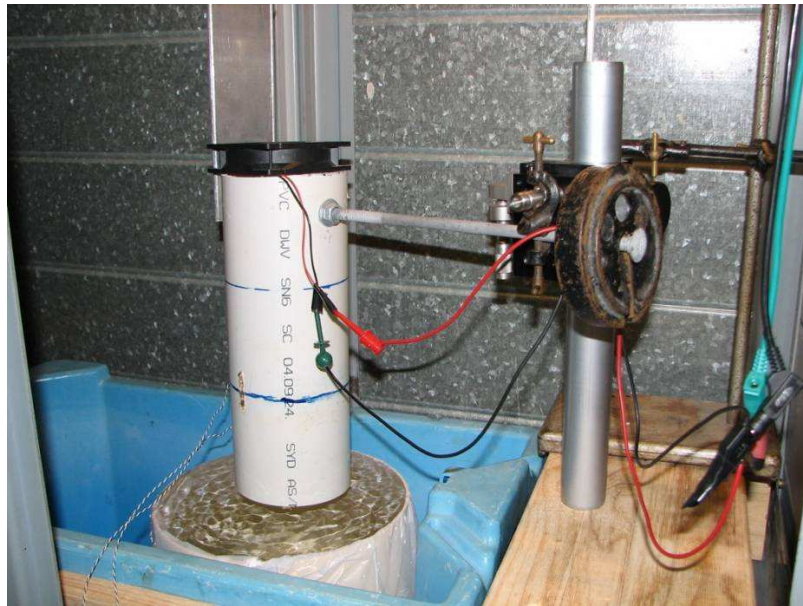


Figure 3.29 Single tube with micrometer height adjustment and fan positioned on top. Measurements were made with thermocouples.

Data was gathered using this setup by varying the voltage of the fan producing different wind speeds, both up and down for clear and monolayer surfaces, an attempt to find a dependable difference that can be found easily with the addition of monolayer. When the fan was on a high setting, the water surface was quite turbulent as shown in Figure 3.29.

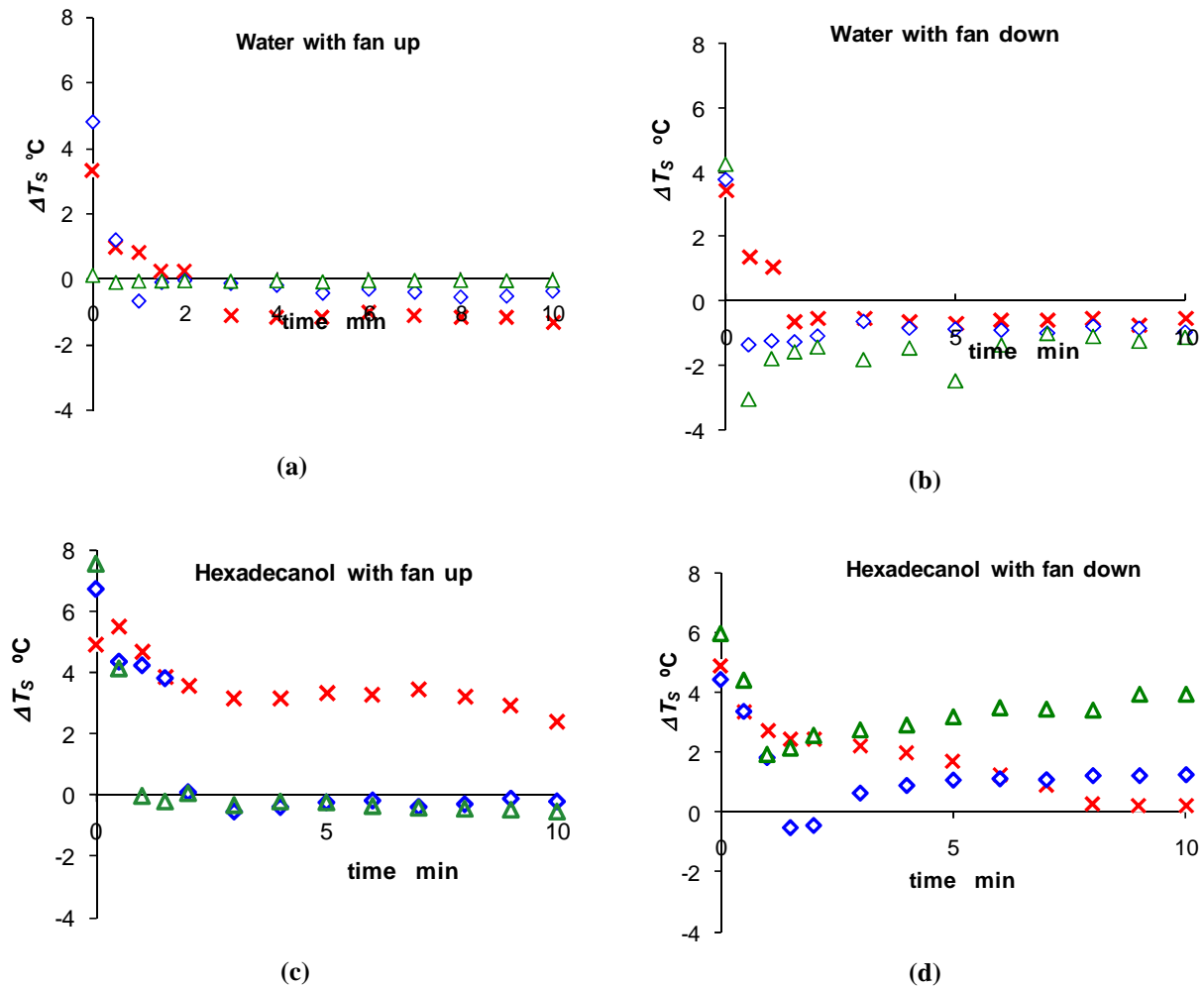


Figure 3.30 Effect of switching fan on at $t = 0$ for; (a) Water surface with fan pushing air upwards. (b) Fan pushing downwards. Also a hexadecanol monolayer with (c) fan pushing air upwards (d) Fan pushing downwards. Wind speeds measured with hand held anemometer directly above fan are; 1.7 m s^{-1} ; \times , 3.0 m s^{-1} ; \diamond , 5.3 m s^{-1} ; \triangle .

Results

The results (Figure 3.30) show a definite warming with the addition of hexadecanol, particularly for low wind speeds. However it is possible that at high wind speeds, the water level in the tube moved, changing the position of the surface thermocouple junction. This is the probable explanation for the large positive ΔT_s seen in the hexadecanol graph with fan down. The 5.3 m s^{-1} fan speed is oddly a higher temperature than the lower fan speeds. The water level would probably have been lowered by the air pressure of the fan leaving the thermocouple junction slightly out of the water. Visually it was hard to tell as there was wave turbulence, and the water level was hard to ascertain. The same high fan speed for water may have had enough wave action to lower the temperature of the junction to water temperature. On close inspection, it also appears that the plots for monolayer do not change temperature as quickly as water.

Again there was concern that the water level altered for large wind speeds using the single tube with fan placed on top. When this was combined with the potentially uneven air flow that would occur across the surface, it was considered useful to alter the tube shape to a Y shape to allow better air flow.

3.4.7 Wind induced temperature changes

In order to compare separate experimental results a standard suitable apparatus was developed as described below. A series of experiments was then undertaken to measure the changes in temperature profile that occur with the addition of monolayer.

Materials and Methods

A 45°100 mm PVC Y tube was used as the sampling chamber, as shown in Figure 3.31. This setup has an arm for fan placement to draw air through, from a large entrance on the other arm. A 12 V 2.9 W computer exhaust fan, 80 mm in diameter was used to provide wind speeds. Measurement of wind speed was made in the centre of the vertical inlet arm in the Y tube, using the Lutron LM8000 anemometer. The speed was adjusted by adjusting the DC supply voltage with the results: 5V produced 0.7 m s^{-1} , 10 V produced 3.0 m s^{-1} and 15 V produced 5.3 m s^{-1} as measured above the inlet. The drawing action of the fan produced no detectable water level changes for fan speeds of up to 6 m s^{-1} .

The shape of the tube is important, as too much horizontal stress produced by the wind could move the monolayer to one side. The air flowing through the Y tube produces turbulent eddies which are capable of removing water vapour from the surface, through not presenting a net drag to the surface which would be capable of removing monolayer coverage. No net movement of the crystals was noticed at any wind speed, indicating coverage of monolayer.

The tube was held in position over the surface using a fastened galvanised metal rod attached to a vertically adjustable micrometer screw gauge. The thermocouple junctions were attached by drilling small holes in the Y tube 5 cm apart and inserting the junctions through into the chamber around 5 mm from the wall. The wire leads were then held in place with silicon sealer glue on the exterior.

An overflow system was used to keep the surface clean for clear water tests and to prepare for monolayer runs. To maintain a clean surface for tests where no monolayer is present an overflow system was used, where a container was placed in a larger container. Tap water was added to the inside container using a clear plastic tube from a tap and allowed to overflow to an outside larger container, to clean the surface. Oil indicator tests showed that this method was more effective than any static method of ensuring cleanliness that was attempted. During clean surface measurements, the tap was left dripping into the overflow container, however, it was turned off for monolayer measurements so monolayer would not be lost.

The monolayer could flow into the tube by two 8 mm wide slits drilled into the side of the tube.

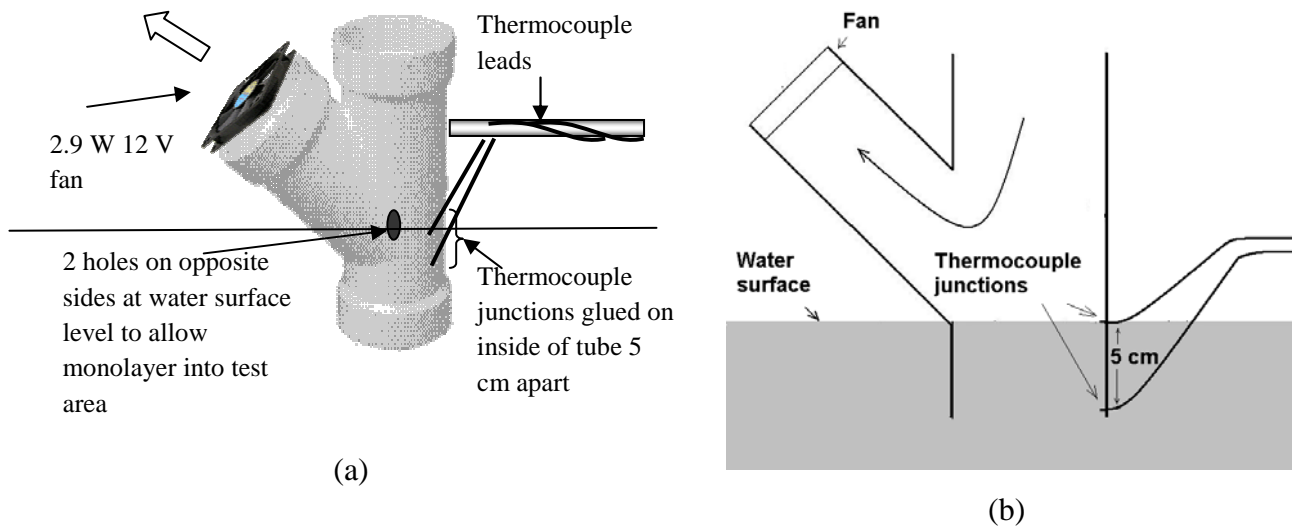


Figure 3.31 PVC Y shaped tube setup. (a) Exterior view showing fan, supporting rod and surface entrance hole, (b) Cross section showing position of thermocouple junctions.

3.4.8 Thermocouple profile measurements referenced to 5 cm depth.

Surface temperature differences resulting from changes in wind speed were measured in the modified sampling chamber by switching the fan on and off and using various wind speeds. Both the magnitude of ΔT_5 and time to reach this value were examined to determine differences.

Materials and methods

The thermocouple junctions were inserted into the side of the tube 5 cm apart. The top junction could be accurately set by moving the assembly using the micrometer scale and following the procedure for positioning just below the surface, then using the micrometer scale to lower it to a certain depth. The fan speeds used were 0.7, 3.0 and 5.3 m s⁻¹ for each of three depths Figure 3.32 Figure 3.33.

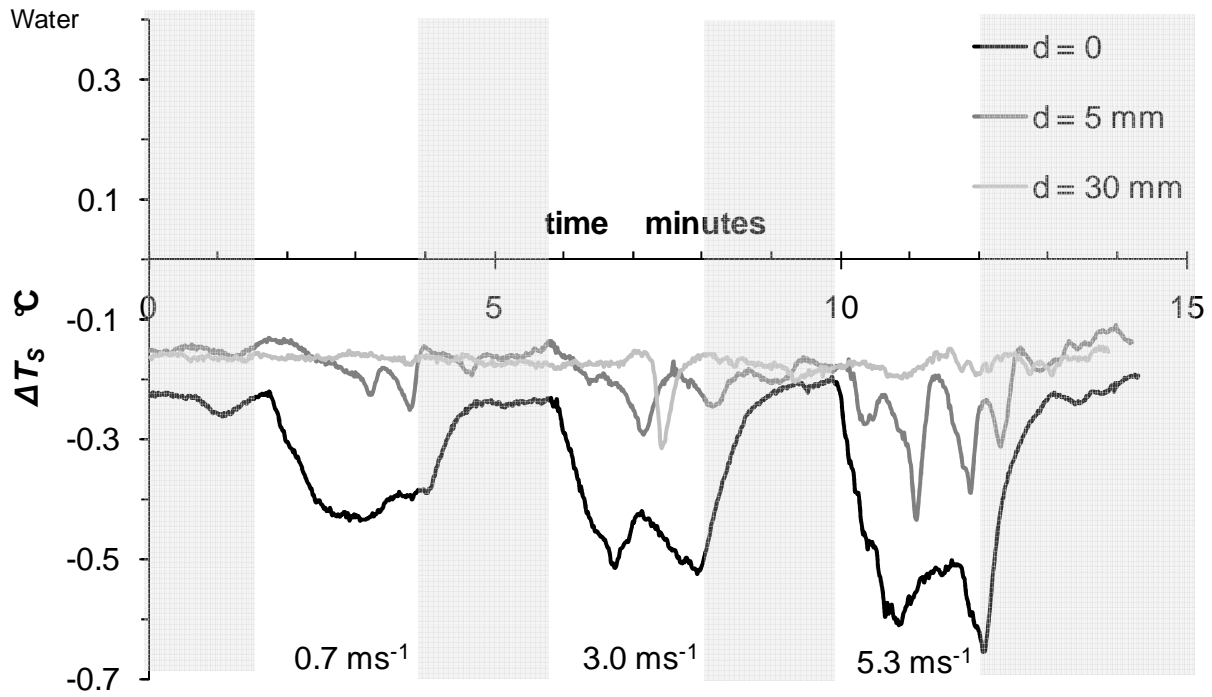


Figure 3.32 Temperature profile for water for three wind speeds. Temperature is referenced to 5 cm depth. Shaded areas correspond to fan switched off.

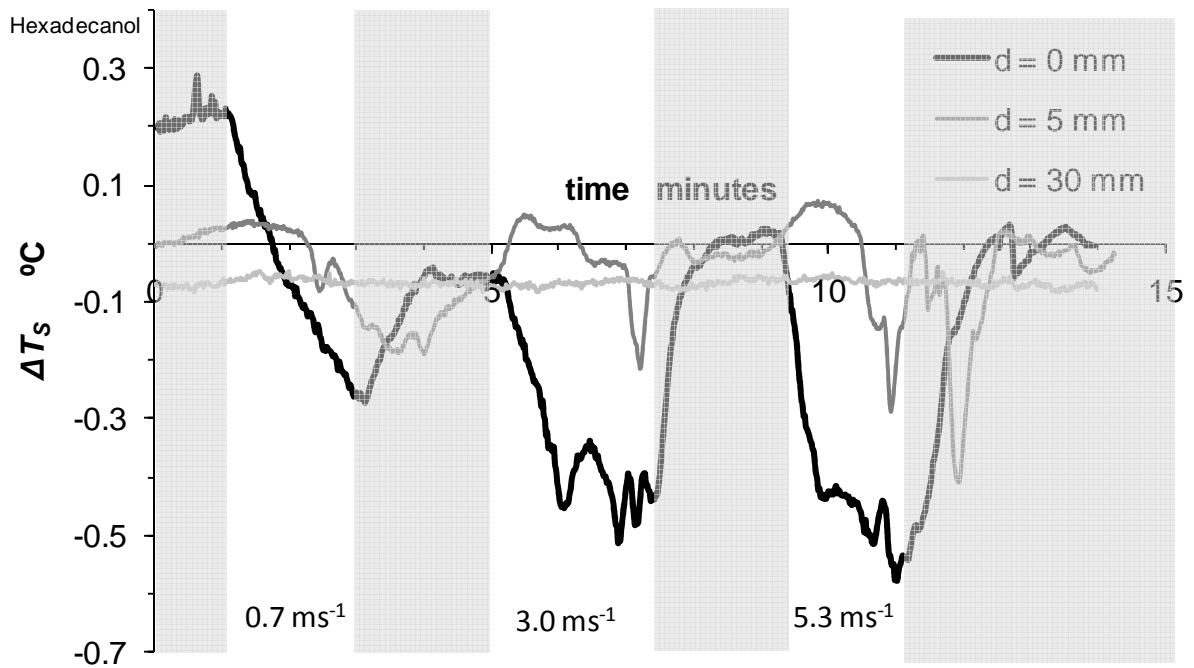


Figure 3.33 Temperature profile for hexadecanol for three wind speeds. Temperature is referenced to 5 cm depth. Shaded areas correspond to fan switched off.

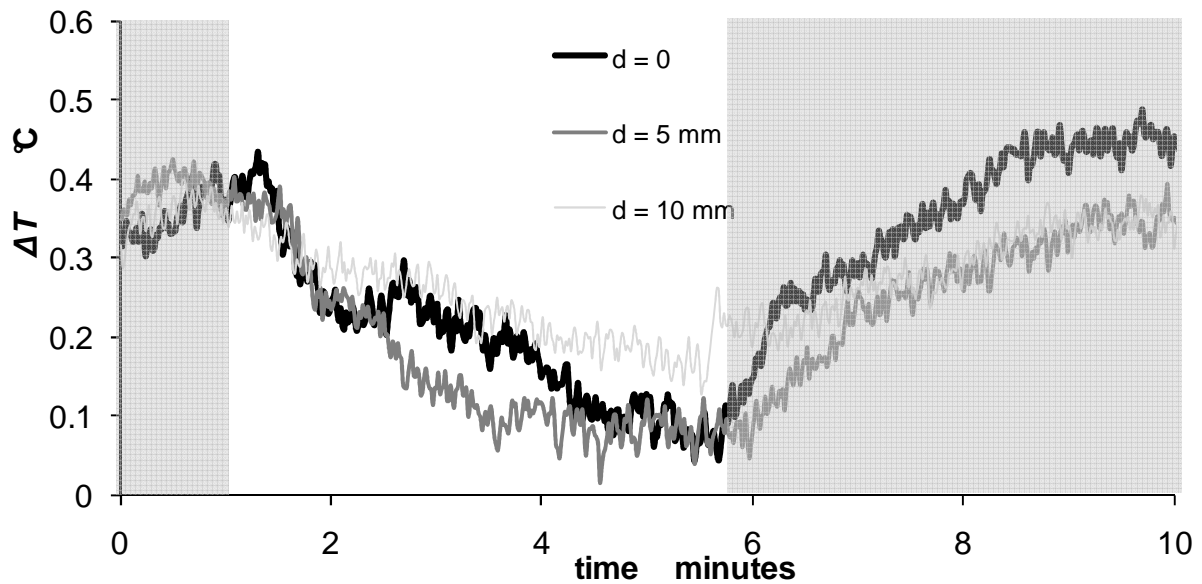


Figure 3.34 High wind speeds of 5.7 m s^{-1} for a water surface, showing evidence of surface mixing. Shaded areas correspond to fan switched off.

Results and Discussion

Figure 3.32 and Figure 3.33 show the temperature at a depth of 0 mm (as close to surface as possible), 5 mm and 30 mm for both a water surface and hexadecanol surface. As expected, the temperature near the surface fluctuates in response to wind to a greater degree than deeper levels. In the presence of monolayer the temperature measurements are generally warmer. The evaporative cooling that occurred in Section 3.4.7 occurred generally by the general temperatures, though no distinct surface features showed as a result of wind speed changing.

The jaggedness of the 0 mm and especially of the 5 mm results are probably due to cold thermals, and not produced by the thermocouples or amplifier.

It was hoped that either the cooling rate or the maximum cooling of the surface would show a significant difference when the fan was turned on, however the behaviour in both plots appeared quite similar.

Figure 3.34 shows the mixing effect for higher wind speeds of 5.7 m s^{-1} . At this speed there is mixing of layers due to turbulence with the cool skin of water disappearing completely.

These plots indicate that at low wind speeds, the monolayer surface does not cool to the same extent as a water surface. It is possible that this difference in temperature created by the difference in latent heat flux may be exaggerated by heating the air.

3.4.9 Accumulation of warm water at the surface referenced to 15 cm depth.

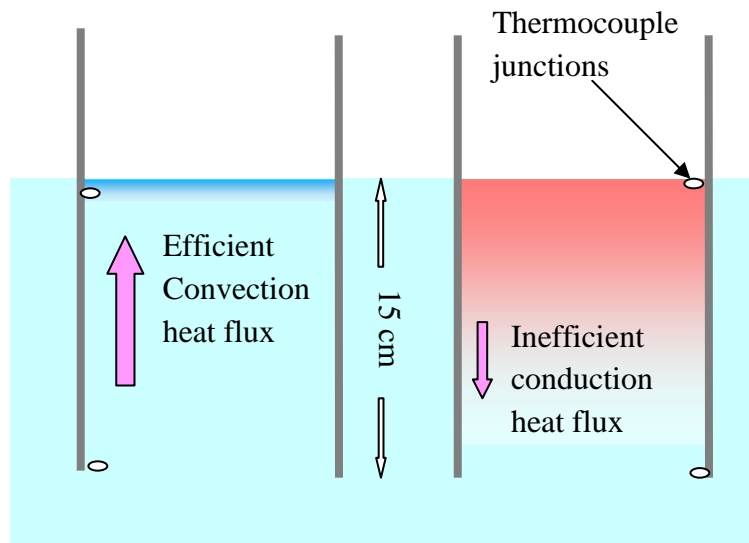


Figure 3.35 Differences between cold skin layer and trapped warm water.

The cool skin of water is not trapped at the surface, but sinks in thermals. Therefore the evidence of a difference in latent heat flux is sinking away from the surface. However if the air is warmed, there is more chance of creating a warm skin, in which thermals do not operate, thereby trapping and accumulating the difference in latent heat between water and monolayer at the surface. In this situation a difference in temperature near the surface may be evident.



Figure 3.36 4 W Heater secured to metal grill fitted inside inlet.

Materials and methods

A 4 W positive temperature coefficient resistor heater (DBK, Germany) was bolted onto a metal grill positioned on the vertical inlet of the Y tube (Figure 3.36).

The thermocouple was attached to an analogue to digital converter on a Picaxe 40 X1, similar to the experiments described in Section 3.4.8. However, the reference thermocouple was lowered to the

bottom of the open tube, 15 cm depth, rather than a depth of 5 cm, as there may be a deeper temperature gradient extending down the full length of the tube.

The fan was switched on for 4 minutes to provide more time for temperature stabilisation. The wind speed was 1.7 m s^{-1} , which is a relatively low speed to maintain the warm surface and prevent excessive turbulent mixing. The T_{AW} value for these experiments was fairly close to 3°C .

Results and Discussion

The plots shown in Figure 3.37 (a) and (b) are representative of many runs measured and show the temperature for water and monolayer with a fan turned on and off. The monolayer surface is again generally warmer than the water surface, however this is only slight, and general temperature differences such as this are of little help in detecting monolayers. It is interesting and consistent with expectations that the cooling gradient of the monolayer was not as rapid when the fan is switched on.

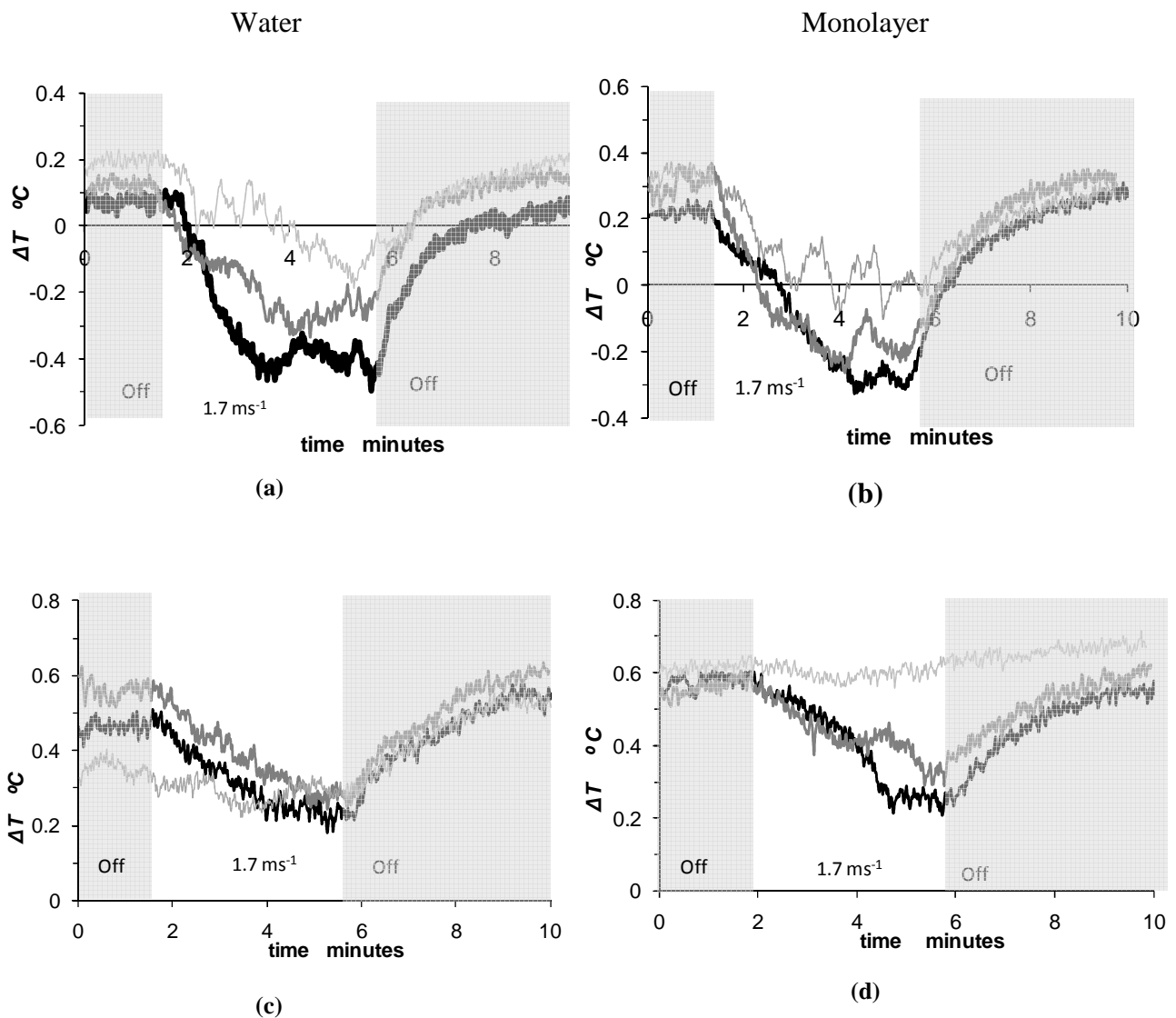


Figure 3.37 Cooling of surface (black heavy line), 1mm depth (grey line) and 4 mm depth (thin light grey line) with no heating for water (a) and hexadecanol (b). Heating of 4 W is shown for water (c) and hexadecanol (d).

When the heater is used (Figure 3.37(b) and (c)), the series both increase in temperature, showing the heater was affecting the temperature near the surface, the cooling of the surface was again delayed for the monolayer. These are chosen samples and averaging to achieve statistically relevant characteristics was found to be unsuccessful due to the highly variable nature of measuring tenths of a degree referenced to 15 cm deep. The use of the 4 W heater was also unable to produce the desired warm skin, despite the deliberate slow wind speed.

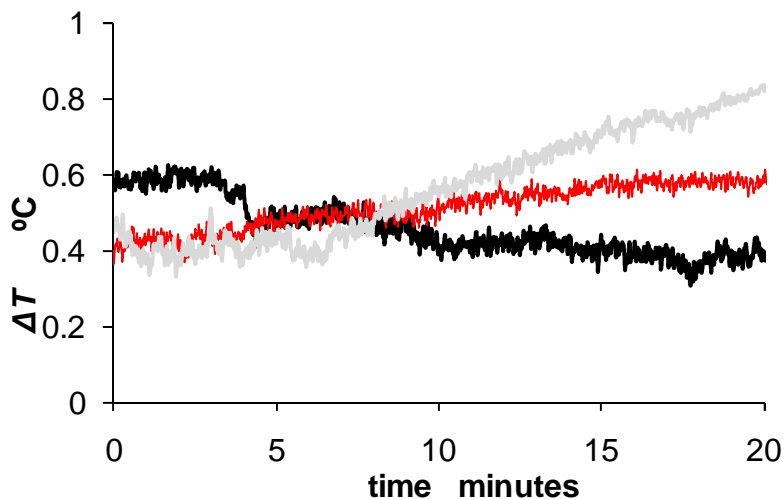


Figure 3.38 Effects of 10W heater and low air flow (1.7 m s^{-1}). Temperature measured at a depth of 1 cm comparing a water surface (black) with no heater, water using heater (thin red) and hexadecanol using heater(grey).

Increasing the power of the resistor to 10 W, while using the same low wind speed (1.7 m s^{-1}) and measuring temperature at a depth of 1 cm (for greater temperature stability) showed some difference between monolayer and water surfaces (Figure 3.38). As expected the water decreased slightly in temperature with no heater. When the heater was used the water rose in temperature slightly, and the monolayer rose around twice the temperature. The temperature differences between monolayer and water surface are, however quite small, being a few tenths of a $^{\circ}\text{C}$. These measurements were still quite unstable considering the reference was 15 cm deep and thermal currents sometimes seem to influence the results.

Further attempts were made to increase the separation in temperature by increasing the power of the resistor to 25W. The effect of this seemed to be that the temperature near the surface of the water increasingly responded to the sensible heat flux rather than the desired evaporative cooling, and no increase in temperature differences between clear surface and hexadecanol were observed.

3.5 Conclusion

Measurement of ΔT_S in various ways using contact methods showed some promise in use as a detection method. The main impediment to its use under field conditions appears to be exact

positioning needed for the surface thermocouple junction in the high temperature gradient skin area, and finding a relatively stable area in the subsurface region to position the reference junction.

The difference in ΔT_s between clear water and monolayer appeared to be larger with the addition of wind; showing a difference of temperature near the surface after a short period of time. Heating of the surface, however produced minimal improvement. The use of an enclosed sampling area (PVC tube) improved the stability of measurements significantly.

The temperature differences being measured between clear water surface and monolayer in this chapter are relatively small since the cool water; being used as the main thermal evidence of evaporation; is being allowed to escape to the depths of the trough and not being measured in the balance of heat fluxes occurring at the surface. This could be corrected by capping the bottom of the sampling tube to capture and include the evaporatively cooled water. The use of troughs will be examined further in subsequent chapters.